Design and Implementation of Calculated Readout by Spectral Parallelism (CRISP) in Magnetic Resonance Imaging (MRI)

by

Simon So

A thesis
presented to the University of Waterloo
in fulfillment of the
thesis requirement for the degree of
Master of Applied Science
in
Systems Design Engineering

Waterloo, Ontario, Canada, 2010

I hereby declare that I am the sole author of this thesis. This is a true copy of the thesis, including any required final revisions, as accepted by my examiners.

I understand that my thesis may be made electronically available to the public.

Abstract

CRISP is a data acquisition and image reconstruction technique that offers theoretical increases in signal-to-noise ratio (SNR) and dynamic range over traditional methods in magnetic resonance imaging (MRI). The incoming broadband MRI signal is de-multiplexed into multiple narrow frequency bands using analog filters. Signal from each narrowband channel is then individually captured and digitized. The original signal is recovered by recombining all the channels via weighted addition, where the weights correspond to the frequency responses of each narrowband filter. With ideal bandpasses and bandwidth dependent noise after filtering, SNR increase is proportional to $\sqrt{N}$, where N is the number of bandpasses. In addition to SNR improvement, free induction decay (FID) echoes in CRISP experience a slower decay rate. In situations where resolution is limited by digitization noise, CRISP is able to capture data further out into the higher frequency regions of k-space, which leads to a relative increase in resolution. The conversion from one broadband MR signal into multiple narrowband channels is realized using a comb or bank of active analog bandpass filters. A custom CRISP RF receiver chain is implemented to downconvert and demodulate the raw MR signal prior to narrowband filtering, and to digitize the signals from each filter channel simultaneously. Results are presented demonstrating that the CRISP receiver chain can acquire 2D MR images (without narrowband filters) with SNR similar to SNR of images obtained with a clinical system. Acquiring 2D CRISP images (with narrowband filters) was not possible due to the lack of phase lock between rows in k-space. RMS noise of narrowband, broadband and unfiltered 1D echoes are compared.

Acknowledgements

I would like to thank all the members of the ALISS group, especially Linda Vu, Jeff Meade, and Andrew Cenko, for their invaluable support and contributions to the CRISP project. All three have put in a lot of work in the beginning to get CRISP up and running. An extra special thank you to Linda for: moving equipment, staying up for long scan sessions, reconstructing images, keeping the project objective in focus, pointing out silly mistakes, and all the little things in between.

I am grateful for Mike Noseworthy and Sergei Obruchkov from Imaging Research Center at St. Joseph's Hospital in Hamilton, Ontario for lending us time on their 3 T system. It was a great pleasure to work with Sergei and I appreciate all the work he has done put in for this project.

I would like to acknowledge Ken Bradshaw and Logi Vidarsson of Sentinelle Medical, and Bill O'Reilly of Tornado Medical Systems, for their advice and assistance, and for spending their time and effort troubleshooting in hardware and software issues with us. Their help was critical in interfacing CRISP with a clinical system. A special thanks to Sentinelle Medical for providing us access to the Sunnybrook IRCCI 1.5 T system.

Implementing a custom RF receiver chain would have been much more difficult without the help of Professor Peemoeller and Claude Lemaire from Physics and Astronomy at University of Waterloo. They allowed us to borrow key pieces of RF equipment, gave us time on the Bruker 11.7 T NMR system, and shared their considerable experience and expertise.

I would like to thank Adrian Spanu, an Undergraduate Research Assistant from Systems Design Engineering, who helped to design the PCB layout for the CRISP narrowband filters.

Last but not least, I offer my sincere gratitude to my supervisor Professor Arsen Hajian for supporting me for the past two years. Thank you for all the academic, professional, and personal advice and for being a great supervisor overall.

To Mom and Dad.

Contents

List of Tables viii

List of Figures xi

Nomenclature xii

1 Introduction 1
- 1.1 Dispersed Fourier Transform Spectrograph . . . 1
- 1.2 Application in MRI . . . 3
- 1.3 Thesis Contribution and Organization . . . 3

2 Basics of MRI 5
- 2.1 Spin . . . 5
- 2.2 Precession . . . 7
- 2.3 Bulk Magnetization . . . 8
- 2.4 Bloch Equations . . . 12
- 2.5 Frequency and Phase Encoding . . . 14
- 2.6 K-space and Image Reconstruction . . . 17

3 CRISP 19
- 3.1 Calculated Readout by Spectral Parallelism . . . 19
- 3.2 State of the Art . . . 20
- 3.3 Comparison to CRISP . . . 21
- 3.4 CRISP Reconstruction . . . 21
- 3.5 Signal-to-Noise Improvement . . . 26
- 3.6 Sensitivity Improvement . . . 28
- 3.7 Conclusion . . . 29

4 RF Receiver Chain 33

4.1 Input Signal . . . 33
4.2 RF Receiver . . . 35
4.3 Quadrature Detection . . . 35
4.4 Local Oscillator . . . 43
4.5 Phase Drift . . . 43
4.6 Experimental Results . . . 47
4.7 Conclusion . . . 47

5 Filter Hardware and Data Acquisition 49
5.1 Filter Requirements . . . 49
5.2 RF Filters . . . 51
5.3 Passive and Active Filters . . . 53
5.4 Filter Response Types . . . 54
5.5 MAX274 . . . 56
5.6 Simulations . . . 57
5.7 Breadboard . . . 59
5.8 Printed Circuit Board . . . 60
5.9 Testing . . . 63
5.10 Analog-to-Digital Conversion . . . 70
5.11 Conclusion . . . 70

6 Results and Discussion 71
6.1 Summary of Results . . . 71
6.2 Limitations . . . 74

7 Conclusion 75
7.1 Future Work . . . 76

APPENDICES 77

A Designing Elliptic Filters 78

B Derivation of MAX274 second-order section transfer function 84

C Initial and Final Resistor Values for CRISP Filters 87

Bibliography 92

List of Tables

4.1 Digital quadrature reference signal values from $n = 0$ to 7. 42
4.2 SNR of images acquired with clinical system and custom CRISP system . . 47

5.1 Designed f_0 and Q values for CRISP bandpass filters. 57
5.2 Error between actual and designed center frequencies for CRISP narrowband bandpass filters. 63

6.1 RMS noise of echoes from bone sample. 72
6.2 Average RMS noise over all trials in $MnCl_2$ experiment. 72

C.1 CRISP bandpass filter resistor values before and after fine adjustments, for filters 1-4 88
C.2 CRISP bandpass filter resistor values before and after fine adjustments, for filters 5-8 89

List of Figures

1.1 A simple conventional Fourier transform spectrograph. 1
1.2 A sample interferogram. Light intensity is captured with a bolometer AC-coupled to the signal. 2
1.3 Organizational diagram for the main chapters of the thesis 4

2.1 Precession of nuclear magnetic moment vector ($\vec{\mu}$) about external $\vec{B}_0$ field. 7
2.2 Zeeman splitting: observable energy difference between spin states caused by the presence of a magnetic field. 9
2.3 Bulk magnetization, $\vec{\mathbf{M}}$, is the sum of all nuclear magnetic moments in a sample. 10
2.4 Net magnetization after application of 90°-pulse. 11
2.5 Recovery of longitudinal magnetization. 15
2.6 Decay of transverse magnetization. 15
2.7 Examples of MR echoes. 16

3.1 Simplified signal flow for (a) SENSE and PILS reconstruction and (b) CRISP reconstruction. 22
3.2 CRISP intermediate images from four bandpass filtered signals. The image region used to estimate bandpass filter response is highlighted. 23
3.3 Image of the calibration water phantom acquired without CRISP bandpass filters 24
3.4 CRISP bandpass filter response profiles. 24
3.5 CRISP reconstruction. In (c), noise outside of the FOV is amplified due to the weighted-add reconstruction. 27
3.6 Low-bit level digitization simulation FIDs from an onion sample. Sampling rate was 500 kHz, therefore, each tick on the x-axis represent 2 μs. 30
3.7 Low-bit level digitization simulation images from an onion sample. 31

4.1 Complex MR signal. 34

4.2 The signal received by an RF coil. 34
4.3 Simple heterodyne receiver chain. 35
4.4 Simple homodyne receiver chain. 36
4.5 Simple receiver chain with CRISP filterbank. 36
4.6 Demodulation with real signal $cos(\omega_0 t)$ 37
4.7 Demodulation with complex signal $e^{-j\omega_0 t}$ 38
4.8 Correcting for quadrature mismatch 39
4.9 Reconstructed images with mismatched quadrature reference pair. 41
4.10 Digital quadrature detection example signal spectrum. 42
4.11 Output spectrum of PTS 500 frequency synthesizer. 44
4.12 K-space data from clinical and CRISP systems. Produced by S. Obruchkov. 45
4.13 Effects of improper phase lock between local oscillator and signal resonant frequency. 46
4.14 Phased-locked loop for demodulation. 46
4.15 Comparison of images acquired with clinical system and custom CRISP receiver chain unfiltered (without narrowband filters) 48

5.1 Bandpass filter response parameters. 50
5.2 Bandpass filter responses for ideal four-channel CRISP system. 51
5.3 A simple SAW filter. 52
5.4 IDL simulation of CRISP bandpass filter magnitude frequency responses. . 58
5.5 SPICE circuit simulation of 12 kHz CRISP bandpass filter. 59
5.6 SPICE simulated frequency response for the CRISP bandpass filters after resistor tuning. 60
5.7 CRISP bandpass filters MAX274 breadboard layout schematic. 61
5.8 CRISP bandpass filters breadboard prototype. 62
5.9 CRISP filters PCB top layer 64
5.10 CRISP filters PCB bottom layer 65
5.11 Narrowband bandpass filters (bottom) and broadband filter (top) partially populated 66
5.12 Frequency sweep of CRISP PCB narrowband filters 1-4 with spectrum analyzer. 67
5.13 Frequency sweep of CRISP PCB narrowband filters 5-8 with spectrum analyzer. 68
5.14 Frequency sweep of CRISP PCB broadband filter with spectrum analyzer. 69

6.1 Acquired echoes from beef bone with CRISP receiver chain. 73

A.1 Visualization of transformation of elliptic lowpass poles and zeroes to bandpass poles and zeroes 79
A.2 Poles and zeroes of normalized 5th-order elliptic lowpass 81
A.3 State-variable biquad topology with additional zero. 82

B.1 Circuit diagram of one second order section in MAX274 84

Nomenclature

Δk_x	K-space sampling interval in x-direction
Δk_y	K-space sampling interval in y-direction
ϵ	Ripple factor, determined by R_p
γ	Gyromagnetic ratio, 2.675×10^8 rad/s/T
$\hbar$	Reduced Planck constant, 1.054572×10^{-34} Js
λ	Wavelength of input light source
ω_0	Larmor frequency
ω_c	Carrier frequency of MR signal
ω_{rf}	Frequency of radio frequency pulse
τ	Time duration of oscillating $\vec{B_1}$ magnetic field/radio frequency pulse
$\vec{\mu}$	Nuclear magnetic moment vector of an isolated spin
$\vec{B_0}$	Main external magnetic field
$\vec{B_1}$	Secondary oscillating magnetic field, orthogonal to main magnetic field $\vec{B_0}$
$\vec{M}$	Net or bulk magnetic moment vector of a packet of spins
$\vec{S}$	Spin angular momentum of an isolated spin
A_{min}	Minimum stopband attenuation for bandpass filter
BW	Filter or signal bandwidth
f_0	Bandpass center frequency
f_c	Center frequency
f_h	Upper 3 dB point for bandpass filter
f_l	Lower 3 dB point for bandpass filter
f_{cutoff}	-3 dB or half-power point or cutoff frequency for low pass filter

$H(s)$	Filter transfer function
I	Spin of atomic nucleus
$I(x, y)$	Continuous 2D image function
$I[u, v]$	Discrete 2D image function
I_{FTS}	Light intensity captured by Fourier transform spectrograph
K	Complete elliptic integral of the first kind
M_z^0	Magnitude of longitudinal magnetization at equilibrium
m_I	Azimuthal quantum number
M_z	Laboratory frame longitudinal magnetization vector
$M_{x'y'}$	Rotating frame transverse magnetization vector
$M_{x'}$	Rotating frame longitudinal magnetization vector
M_{xy}	Laboratory frame transverse magnetization vector
P_1	Path length of the delay arm in a Fourier transform spectrograph
Q	Quality factor of resonant circuits
R_n	n-th order Chebyshev rational function
R_p	Magnitude of passband ripple of bandpass filter
R_p	Magnitude of stopband ripple of bandpass filter
s	Spin quantum number
$S(k_x, k_y)$	Continuous 2D k-space
$S(t)$	Signal induced in RF receiver coil, i.e. free induction decay (FID)
$S[m, n]$	Digitized or sampled 2D k-space
T_1	Time constant for spin-lattice or longitudinal relaxation
T_2	Time constant for spin-spin or transverse relaxation
T_n	n-th degree Chebyshev polynomial
W_x	Field-of-view in x-direction
W_y	Field-of-view in y-direction
x	Delay position of the retroreflector in a Fourier transform spectrograph

Chapter 1

Introduction

Calculated Readout by Spectral Parallelism (CRISP) is a method of noise reduction that can be applied to magnetic resonance imaging (MRI) [1]. The motivation and basic principles behind CRISP stem from the dispersed Fourier transform spectrograph (dFTS) developed by Professor Hajian et al. [2]. Other than sharing similar underlying basic principles, CRISP is a distinct technology from dFTS.

1.1 Dispersed Fourier Transform Spectrograph

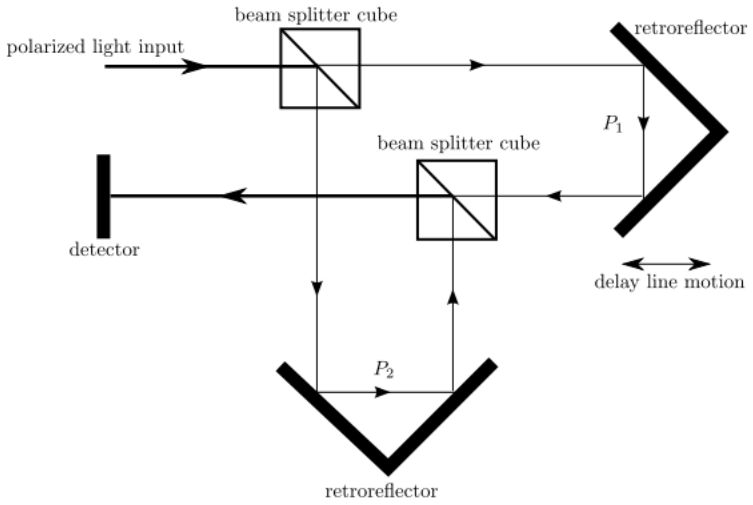

Figure 1.1: A simple conventional Fourier transform spectrograph.

Fig. 1.1 illustrates a simple version of a conventional Fourier transform spectrograph

(FTS). Incoming polarized light is split into two beams by the first beam splitter cube. One beam travels to the retroreflector to the right and then bounces back. The other travels down to the second retroreflector and then bounces back. The two reflected beams are recombined at the second beam splitter cube and the resulting beam hits the detector. The retroreflector on the right is allowed to move along one axis, and a change in the delay position of the reflector, denoted as x, corresponds to a change in the path length P_1. If light with wavelength λ is the input, then light from the two different paths constructively interfere completely when x/λ is an integer and destructively interfere completely when x/λ is an integer plus 1/2. The captured light intensity, I_{FTS} , is at a maximum when $x = 0$, and at a minimum when $x = \lambda/2$. As a function of delay x, I_{FTS} oscillates sinusoidally above and below the mean signal level. The magnitude of oscillation decreases as x increases and the frequency of oscillation corresponds to the center wavelength of the bandwidth of the light source. The resulting plot of I_{FTS} versus x is called an interferogram. The region of x where large deviations from the mean signal level is found is called the fringe packet. At large x, the oscillations diminish to the mean signal level. Fig. 1.2 shows a sample interferogram, where the light is captured with a bolometer AC-coupled to the signal, hence the nearly zero mean signal level [3].

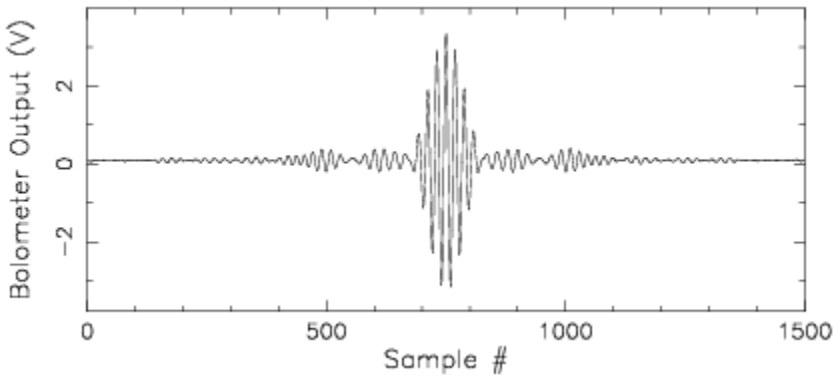

Figure 1.2: A sample interferogram. Light intensity is captured with a bolometer AC-coupled to the signal [3].

An important point to note is the Fourier relationship between the bandwidth of the input source, and the width of the envelope of the fringe packet. A wideband light source has a narrow envelope and fringes disappear quickly as x increases, while a narrowband light source has a wider envelope with fringes disappearing more slowly as x increases.

The dispersed FTS uses a diffraction grating to separate a broadband signal into multiple narrowband channels. This has the effect of converting a single broadband FTS into many narrowband FTSes. The advantage of doing such is twofold. First, due to the smaller bandwidth of each narrowband channel, sampling requirement for each is reduced.

The Nyquist theorem is satisfied when the sampling frequency is greater than twice the bandwidth of the band-limited signal. In order words, the sampling period must be less than the reciprocal of twice the bandwidth. Therefore, a larger sampling period is possible with the dFTS without aliasing. Second, narrowband signals correspond to wider fringe packets, meaning more signal for a larger range of delays. Assuming Poisson distributed noise, this results in a signal-to-noise improvement in the reconstructed spectrum.

1.2 Application in MRI

In MRI, the signal being measured is in the radio frequency range, 64 MHz for 1.5 T systems, instead of several THz for optical systems, but the basic principle behind dFTS can still be applied. Treating the MR signal as a broadband signal, it can be converted into multiple narrowband channels using analog bandpass filters instead of a diffraction grating. The narrowband signals are then recombined and the MR image is reconstructed from the narrowband fragments. This method of processing MR signals is known as CRISP.

1.3 Thesis Contribution and Organization

This thesis investigates CRISP as a method of acquiring and reconstructing MR data. Chapter 2 offers a review of MRI basics. The expected benefits with CRISP will be discussed and compared to recent developments in MR data acquisition and image reconstruction algorithms in chapter 3. Initial experimental and simulation results using an NMR system are presented.

The construction of a CRISP prototype system is divided into two major sections: 1) implementation of a custom RF receiver chain, and 2) designing and building analog bandpass filters. Chapter 4 deals with the implementation of a custom RF receiver chain, demonstrates experimental results acquired with the system, and compares them with images obtained with a clinical MRI system. Chapter 5 describes the process of design, implementation, and testing of the analog bandpass filters. Results obtained with filters and custom receiver chain are shown. Chapter 6 summarizes the results acquired with the CRISP system and finally, chapter 7 presents some possible future directions for this work.

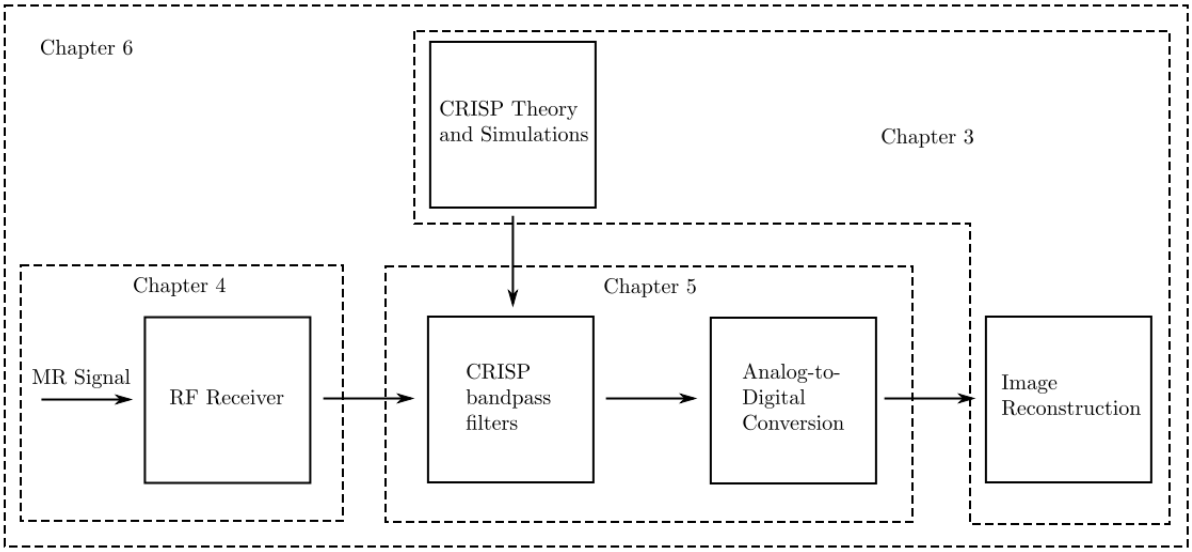

Figure 1.3: Organizational diagram for the main chapters of the thesis

Chapter 2

Basics of MRI

The field of nuclear magnetic resonance (NMR) was founded on the experiments performed independently by Felix Bloch and Edward Purcell [4, 5]; they were awarded a joint Nobel Prize in Physics for their discovery in 1952. In an external magnetic field, NMR-active nuclei precess about the direction of the field. When energy is applied to the system in the form of a radio frequency (RF) pulse at the frequency of precession, a rotating magnetic field is generated. This rotating field excite the nuclei such that a magnetization, precessing about the external field, is established. As a consequence, a current is induced in an RF receive coil. This resulting signal is the MR signal. Spectroscopy on different types of solids and liquids can be performed by exploiting this effect. Furthermore, with careful manipulation of magnetic field gradients and RF pulses, the familiar 2-D and 3-D images in magnetic resonance imaging (MRI) can be obtained. An explanation of how the NMR signal is generated and how it is used to produce an image begins with the quantum mechanical property known as spin.

2.1 Spin

Spin is a form of angular momentum, but unlike classical angular momentum, it is not a result of physical motion of a particle. Spin is an intrinsic quantity akin to mass or charge. All elementary particles have an associated spin quantum number, s. The magnitude of total angular momentum of a particle with spin s is $\sqrt{s(s+1)}\hbar$ [6] where s can take on positive integer or half-integer values, i.e. $s = 0, 1/2, 1, 3/2, \ldots$, and so on. For example, $s = 1/2$ for both neutrons and protons.

The angular momentum of a system with multiple parts is a quantized vector sum of their individual angular momenta. The magnitude of the total angular momentum of a

two-part system is given by $\sqrt{l_3(l_3+1)}\hbar$ [6], where l_3 is constrained by

$$|l_1 - l_2| \leq l_3 \leq l_1 + l_2, \tag{2.1}$$

and l_1 and l_2 are the quantum numbers of the individual parts.

An atomic nucleus has nuclear spin angular momentum equal to the combination of the spin angular momentum of their individual constituents, i.e. protons and neutrons, as well as the orbital angular momentum of the nucleons. The spin quantum number I for the intrinsic nuclear spin angular momentum follows the following general rules. Nuclei with an even number of protons and and even mass number have zero spin. Those with odd number of protons and even mass number have integer spin. Nucleus with an odd mass number have half-integer spin. The most abundant hydrogen isotope, ^1H, has one proton in its nucleus and therefore has spin 1/2. The nucleus of deuterium, ^2H, a relatively rare hydrogen isotope, has one proton and one neutron and spin 1.

Spin angular momentum and nuclear magnetic moment are proportional to each other via the relationship [7, 8]:

$$\vec{\mu} = \gamma \vec{S}, \tag{2.2}$$

where γ is a proportionality constant describing the ratio between the magnetic moment and the angular momentum of a nuclear spin. This constant is known as the gyromagnetic ratio. For protons, ^1H, the gyromagnetic ratio is $\gamma = 2.675 \times 10^8\ rad/s/T$. The magnitude of the magnetic moment can be determined from [7]:

$$\mu = \gamma\hbar\sqrt{I(I+1)}.$$

However, in general, the direction of the spin angular momentum vector, which is defined as the spin polarization axis, is random in the absence of an external magnetic field. Depending on the sign of the gyromagnetic ratio, the magnetic moment vector is pointing either in the same or opposite direction of the spin polarization axis. In the case of ^1H, which has a positive gyromagnetic ratio, the spin polarization axis and the magnetic moment vector point in the same direction.

In the presence of an external magnetic field, $\vec{B_0}$, the magnitude of z-component of the magnetic moment vector is given by

$$\mu_z = \gamma m_I \hbar,$$

By convention, the z-axis is chosen to be aligned with the direction of the external magnetic field, i.e. $\vec{B_0} = B_0\vec{k}$ [7]. The magnetic quantum number, m_I, takes on $(2I+1)$ possible values from $-I$ to $+I$ in integer steps. For ^1H, since $I = 1/2$, m_I is -1/2 or +1/2, often referred to as spin 'down' and spin 'up' states respectively. This corresponds to the two

possible orientations of the spin polarization axis of the ^1H nucleus in relation to the $\vec{B_0}$ magnetic field. There is an energy difference between these two spin states, which is important for the generation of an observable signal. Instead of perfectly aligning itself along the $\vec{B_0}$ field as one could imagine a macroscopic bar magnet would do, $\vec{\mu}$ rotates around the magnetic field in a cone, keeping a constant angle with respect to the field. This motion is called precession.

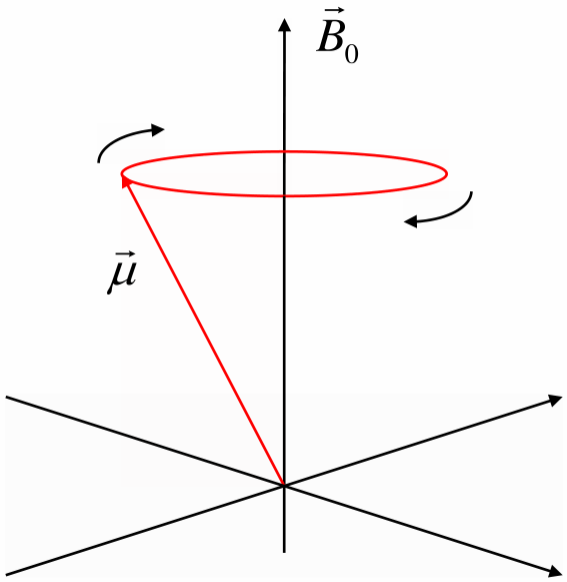

Figure 2.1: Precession of nuclear magnetic moment vector ($\vec{\mu}$) about external $\vec{B_0}$ field.

2.2 Precession

The precession of the nuclear magnetic moment vector is often compared to the motion of a child's spinning top whose axis is tilted away from vertical. In classical physics, analysis of the motion of a spinning top is complicated by factors such as friction, internal degrees of freedom, and additional sources of angular momentum [6]. However, the precession of $\vec{\mu}$ in a magnetic field is free of such complications. The angular frequency of precession can be derived by considering the torque on the magnetic moment [7], $\vec{\mu}$, and recalling from classical physics that torque is the rate of change of angular momentum, $\vec{S}$ [8]:

$$\frac{d\vec{S}}{dt} = \vec{\mu} \times B_0\vec{k}.$$

From Eq. 2.2, $\vec{\mu} = \gamma\vec{S}$, and so:

$$\frac{d\vec{\mu}}{dt} = \gamma\vec{\mu} \times B_0\vec{k}. \tag{2.3}$$

Solving Eq. 2.3 results in:

$$\begin{aligned} \mu_{xy}(t) &= \mu_{xy}(0)e^{-j\gamma B_0 t} \\ \mu_z(t) &= \mu_z(0), \end{aligned} \tag{2.4}$$

where $\mu_{xy} = \mu_x + j\mu_y$. Eq. 2.4 indicates that $\vec{\mu}$ precesses about the external magnetic field, $B_0\vec{k}$, and the frequency of precession is given by:

$$\omega_0 = -\gamma B_0, \tag{2.5}$$

where ω_0 is the Larmor frequency [6, 7, 9] in radians ($\omega = 2\pi f$). Since γ is positive for ^1H, ω_0 is negative. Assuming the magnetic field $\vec{B_0}$ points 'up', the negative frequency indicates that the direction of precession is clockwise when looking 'down' from the 'top'. One can also use the left-hand rule: fingers curl in the direction of precession and the left thumb points in the direction of the magnetic field.

Now consider an ensemble of spins, such as all the ^1H nuclei in a water sample. Without an external magnetic field, spin polarization is isotropic, i.e. spin polarizations are random and have an equal probability of pointing in any direction in space. With the B_0 magnetic field turned on, all ^1H nuclei begin to precess around the field at the same Larmor frequency. Due to tiny fluctuations in magnetic field strength and direction that each proton is experiencing, the 'cones of precession', that is, the angle between $\vec{B_0}$ and each microscopic $\vec{\mu}$, may be different for each individual $\vec{\mu}$ [6]. However, macroscopically, considering the ensemble of spins in the water sample, the net distribution of spin polarizations is slightly in favour of the spin states where the magnetic moment vector is aligned with the magnetic field, as opposed to the orientations where the magnetic moment is pointing in the opposite direction from the magnetic field. The splitting of energy states is termed the Zeeman splitting effect (see Fig. 2.2) and the population difference between the energy states is predicted by the Boltzmann distribution [7]. This population difference leads to a small net or bulk magnetic moment, $\vec{M}$, to appear in the water sample along the longitudinal direction (z-axis).

2.3 Bulk Magnetization

Bulk or net magnetization is defined as the sum of all nuclear magnetic moments in a sample [7]:

$$\vec{\mathbf{M}} = \sum_{i=0}^{N} \vec{\mu_i},$$

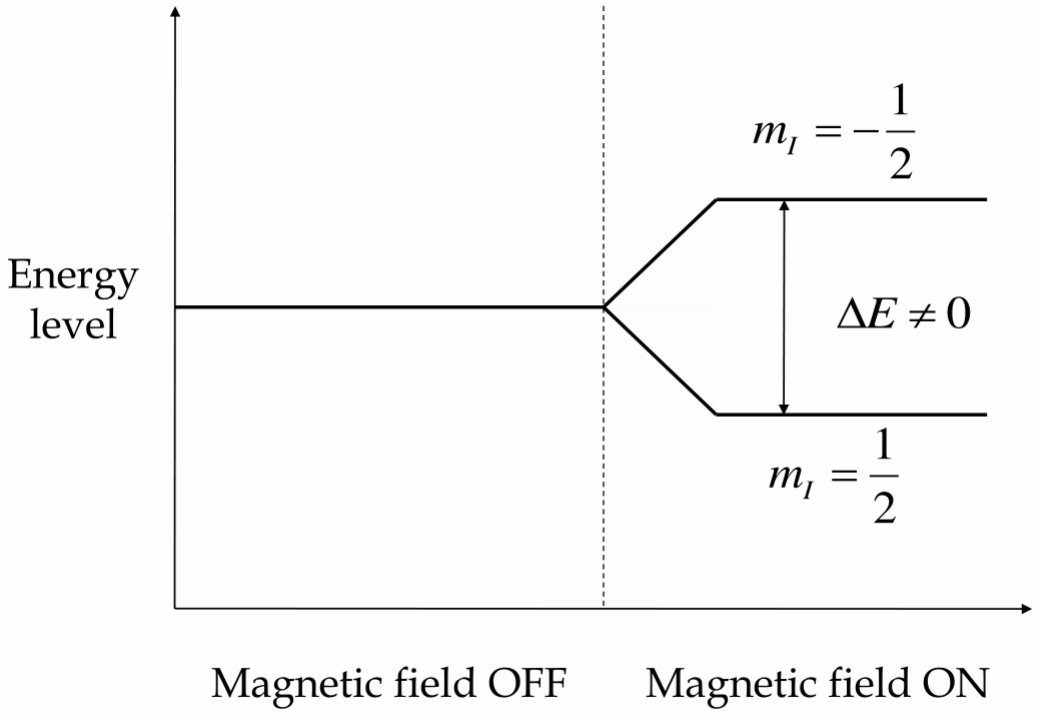

Figure 2.2: Zeeman splitting: observable energy difference between spin states caused by the presence of a magnetic field.

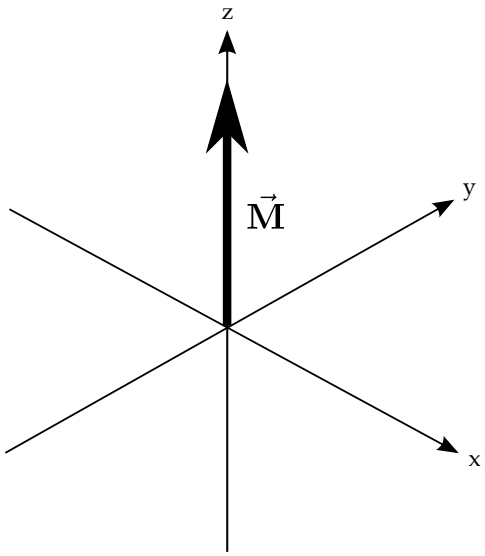

Figure 2.3: Bulk magnetization, $\vec{\mathbf{M}}$, is the sum of all nuclear magnetic moments in a sample.

The magnetization vector points in the same direction as the $\vec{B_0}$ field (positive z-axis) because phase coherence between individual magnetic moments does not exist yet. In other words, although all the protons are precessing about $\vec{B_0}$ at the Larmor frequency, they are all out of phase with each other. As a result, the transverse components of all the magnetic moments cancel each other, and only the longitudinal components constructively sum together to give a net magnetization vector.

It is convenient here to introduce a rotating frame of reference, as opposed to the original laboratory frame of reference, which rotates about the z-axis at the Larmor frequency. The transverse axes in the rotating frame are denoted as the x' and y' axes. In this new coordinate system, a vector in the transverse plane rotating about the z-axis at the Larmor frequency would appear to be stationary. Vectors going slower than the Larmor frequency appear to be rotating anti-clockwise and vectors going faster appear to be rotating clockwise.

The bulk magnetization vector can be tipped from the z-axis down to the transverse plane using a short duration, oscillating magnetic field, known as $\vec{B_1}$, orthogonal to the main magnetic field $\vec{B_0}$, illustrated in Fig. 2.4. In order to have any effect on net magnetization, the frequency of oscillation must satisfy what is known as the resonance condition [7]:

$$\omega_{rf} = \gamma B_0. \tag{2.6}$$

Therefore, recalling Eq. 2.5, ω_{rf} must equal the Larmor frequency.

The $\vec{B_1}$ field is generated using RF pulses through transmitter coils. For example, a $\vec{B_1}$

field oscillating at the Larmor frequency between positive and negative x-axis is created using a coil placed around the x-axis and applying an alternating current at the Larmor frequency. In the rotating frame of reference, the $\vec{B_1}$ field appears stationary, pointing along the x'-axis. The net magnetization vector rotates about the $\vec{B_1}$ field. The angle of rotation is dependent upon the strength and duration of $\vec{B_1}$ [9]:

$$\theta = 2\pi\gamma\tau B_1, \tag{2.7}$$

where τ is the time duration of the $\vec{B_1}$ pulse.

A 90°-pulse tips the net magnetization vector 90° toward the y'-axis, as shown in Fig. 2.4. In the laboratory frame, the net magnetization vector follows a spiral path down to the transverse plane, making the motion much more difficult to describe, hence the introduction of the rotating frame of reference. Similarly, a 180°-pulse rotates the magnetization vector 180° about the x'-axis and results in the vector pointing in the negative z direction [7].

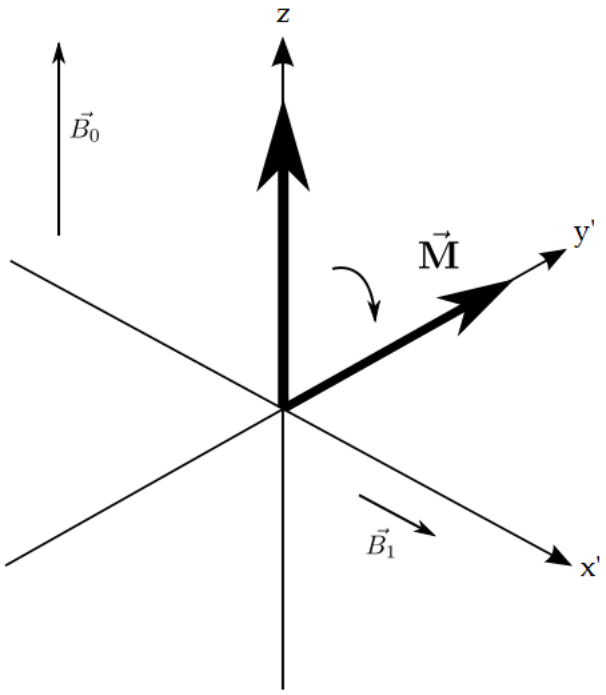

Figure 2.4: Net magnetization after application of 90°-pulse.

2.4 Bloch Equations

The $\vec{B_1}$ field is turned on for a short period of time and then turned off. The process through which the spin system returns to its equilibrium state after the $\vec{B_1}$ field is switched off is called relaxation [9]. The net magnetization vector is split into its longitudinal and transverse components, M_z and M_{xy} respectively. The recovery of M_z is termed spin-lattice or longitudinal relaxation, and the decay of M_{xy} is called spin-spin or transverse relaxation [7].

Bloch equations, introduced by Felix Bloch, describe the time-dependent behaviour of the bulk magnetization vector in a magnetic field. Note that these are only phenomenological equations and the mechanics of the relaxation process is too detailed to be covered in this document. In vector form [7], where $\vec{\mathbf{M}} = (M_x, M_y, M_z)$,

$$\frac{d\vec{\mathbf{M}}}{dt} = \gamma\vec{\mathbf{M}} \times \vec{\mathbf{B}} - \frac{M_x\vec{i} + M_y\vec{j}}{T_2} - \frac{(M_z - M_z^0)\vec{k}}{T_1}.$$

The terms involving T_1 and T_2 describe the relaxation process. T_1 is the time constant for longitudinal relaxation and T_2 is the time constant for transverse relaxation. Note the similarity with the classical equation of the motion of a gyroscope, i.e.

$$\frac{d\vec{\mathbf{L}}}{dt} = \vec{\mathbf{r}} \times m\vec{\mathbf{g}}.$$

In component form [4],

$$\begin{aligned}
\frac{dM_x(t)}{dt} &= \gamma[M_y(t)B_z(t) - M_z(t)B_y(t)] - \frac{M_x(t)}{T_2} \\
\frac{dM_y(t)}{dt} &= \gamma[M_z(t)B_x(t) - M_x(t)B_z(t)] - \frac{M_y(t)}{T_2} \\
\frac{dM_z(t)}{dt} &= \gamma[M_x(t)B_y(t) - M_y(t)B_x(t)] - \frac{M_z(t) - M_z^0}{T_1},
\end{aligned} \tag{2.8}$$

where M_z^0 is the longitudinal magnetization at equilibrium. B_x, B_y and B_z are the x, y, and z-components of the $\vec{B_1}$ field, where $B_x = B_1 cos(\omega_{rf}t)$, $B_y = B_1 sin(\omega_{rf}t)$ and $B_z = 0$. For simplicity, off-resonance effects are not taken into account, that is, assume $\omega_0 - \omega_{rf} = 0$. Eq. 2.8 can then be expressed in the rotating frame of reference as follows [10]:

$$\begin{aligned}
\frac{dM_{x'}(t)}{dt} &= -\frac{M_{x'}(t)}{T_2} \\
\frac{dM_{y'}(t)}{dt} &= \gamma M_z(t)B_1 - \frac{M_{y'}(t)}{T_2} \\
\frac{dM_z(t)}{dt} &= \gamma M_{y'}(t)B_1 - \frac{M_z(t) - M_z^0}{T_1}.
\end{aligned} \tag{2.9}$$

Note that $M_{z'}$ and M_z are equal since they are co-linear.

Consider the free precession scenario, where no RF pulses or $\vec{B_1}$ fields are being applied, magnetization is allowed to freely recover to equilibrium. In this case, $B_{x'}$ and $B_{y'}$ are both zero, and Eq. 2.9 reduces to [4]:

$$\begin{aligned}
\frac{dM_{x'}(t)}{dt} &= -\frac{M_{x'}(t)}{T_2} \\
\frac{dM_{y'}(t)}{dt} &= -\frac{M_{y'}(t)}{T_2} \\
\frac{dM_{z'}(t)}{dt} &= -\frac{M_{z'}(t) - M_z^0}{T_1}.
\end{aligned}$$

Solving the above system of first-order differential equations yields the following:

$$\begin{aligned}
M_{x'}(t) &= M_{x'}(0)e^{-t/T_2} \\
M_{y'}(t) &= M_{y'}(0)e^{-t/T_2} \\
M_{z'}(t) &= M_{z'}(0)(1 - e^{-t/T_1}).
\end{aligned} \tag{2.10}$$

M_z is known as the longitudinal nuclear magnetization and M_x and M_y can be combined to form the transverse nuclear magnetization, M_{xy}. Eq. 2.10 can be written as:

$$\begin{aligned}
M_{x'y'}(t) &= M_{x'y'}(0)e^{-t/T_2} \\
M_{z'}(t) &= M_z^0(1 - e^{-t/T_1}).
\end{aligned} \tag{2.11}$$

Transformation from the rotating frame to the laboratory frame, the frame in which signals are measured, can be done with the following relationship [7]:

$$M_{xy}(t) = M_{x'y'}(t)e^{-j\omega_0 t}.$$

Therefore,

$$\begin{aligned}
M_{xy}(t) &= M_{xy}(0)e^{-t/T_2}e^{-j\omega_0 t} \\
M_z(t) &= M_z^0(1 - e^{-t/T_1}).
\end{aligned} \tag{2.12}$$

As seen in Fig. 2.5 and 2.6, the recovery of the longitudinal magnetization is characterized by time constant T_1 and similarly the decay of transverse magnetization by T_2. If a coil were placed around the x-axis, a signal would be induced by the precession of the transverse magnetization vector M_{xy}. Note that M_{xy} is a circularly polarized magnetic field and that using one coil around the x-axis will pick up only one of quadrature components. Two orthogonal coils in quadrature are required to receive both components. Quadrature

detection methods will be discussed in chapter 4. This signal induced in the receiver coils, $S(t)$, is called the free induction decay (FID):

$$S(t) = M_z^0 e^{j\omega_0 t} e^{-t/T_2}.$$

T_1 is the time constant describing the rate at which spins realign with the external magnetic field and is affected by the spins' ability to exchange energy with their surroundings. T_1 is shorter for fat, and longer for water. T_2 decay is due to distributions of the local magnetic fields, which causes phase decoherence (dephasing) of the spins and thus a loss of net signal. Fat has short T_2 times and water has long T_2 times.

There is a period of 'receiver dead time' following an RF pulse where the receiver electronics are saturated and unable to capture signal [11]. For this reason, the first part of an FID, which occurs at the time of the RF pulse, is often unobservable. Instead, another signal known as an 'echo' is generated after the FID fades away. The FID decays due to dephasing of spins; some spins precess faster than others, and some slower than others, eventually all the spins are at different phases and cancel each other out. A 180°-pulse is applied after the FID fades away, which flips all the spins 180° such that the faster spins are now lagging behind the slower spins. After some time, the spins will rephase and begin to dephase once again. The result is a symmetrical signal, where the rate of rephasing and dephasing is governed by T_2. Fig. 2.7 shows a few examples of echoes.

These echoes are similar to the interferograms produced by FTS instrumentation, shown previously in Fig. 1.2. MRI echoes, instead of interfering light, are produced by the summation of RF signals, and the relationship between the bandwidth of light and width of the resultant fringe envelope is analogous to the relationship between the bandwidth of the RF signal and the envelope of the resultant echo. This is examined in more detail in chapter 3.

2.5 Frequency and Phase Encoding

The FID is the combination of signals from all spins in the sample. In order to perform imaging, there must be a way to differentiate between signals from different physical locations. If all the spins are precessing at the same frequency and phase, it becomes a difficult, if not impossible, task to identify the origin of the signal. Phase and frequency encoding is a technique to localize each voxel (3-D pixel) with a unique frequency and phase pair such that signal from each voxel could be recovered [9]. If a linear magnetic gradient were applied across one dimension of the image, say the vertical direction, spins in the rows experiencing a lower magnetic field would precess more slowly (according to the Larmor equation) and spins in rows experiencing a larger magnetic field would precess more quickly. When the gradient is turned off, all the spins precess at the same Larmor

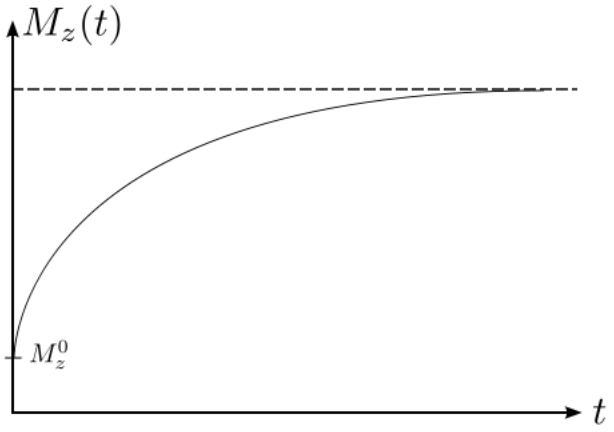

Figure 2.5: Recovery of longitudinal magnetization.

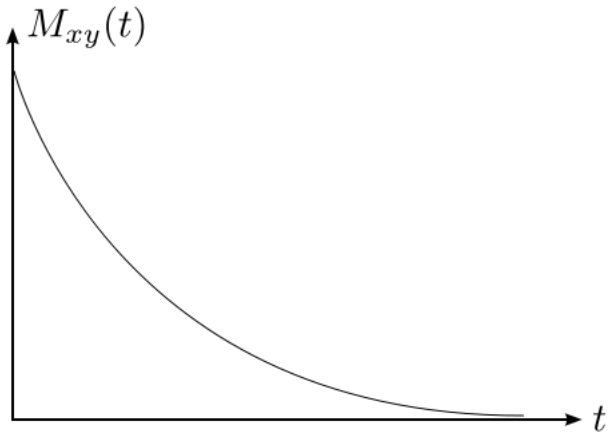

Figure 2.6: Decay of transverse magnetization.

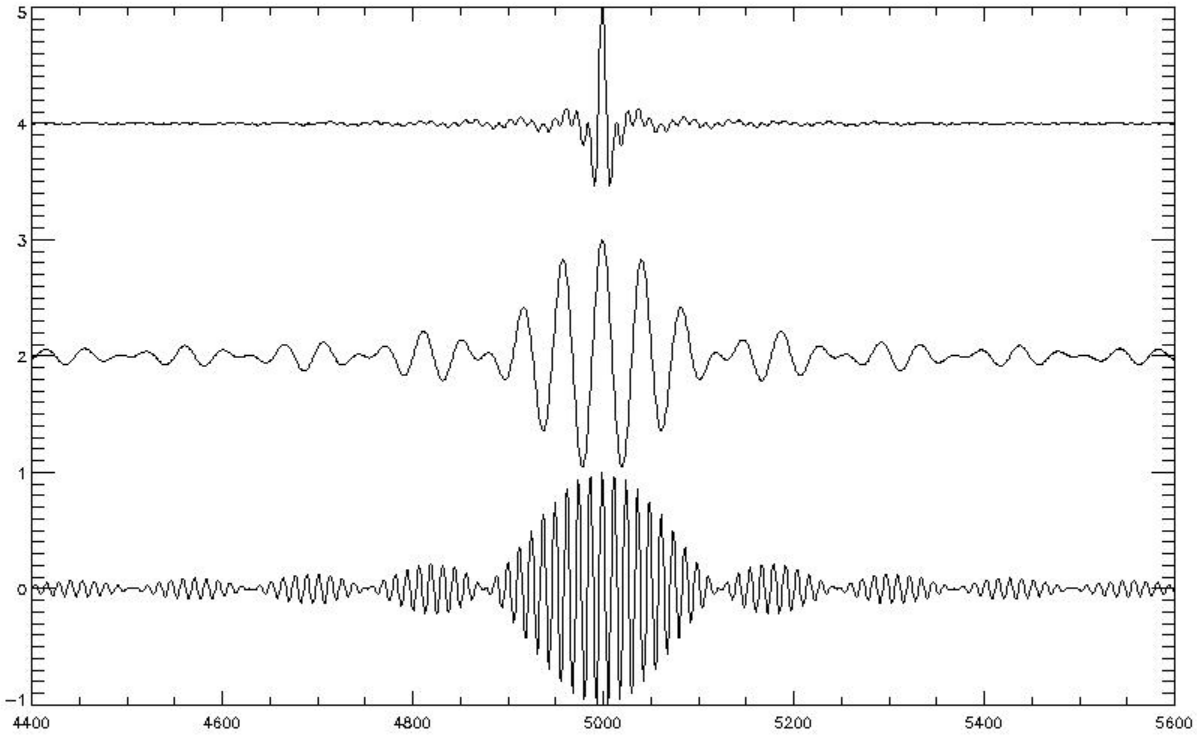

Figure 2.7: Examples of MR echoes. From top to bottom: broadband unfiltered, narrowband filtered low frequency (channel 1/8), narrowband filtered high frequency (channel 8/8).

frequency again, but each row now has a different phase from the next. Then if a linear gradient were to be applied across the horizontal direction, spins in each column would precess at a different frequency. Now, we have encoded each voxel with a frequency and phase, varying by frequency horizontally and phase vertically. By applying the gradients in different directions (x, y, z), sagittal, coronal, and axial images can be obtained.

2.6 K-space and Image Reconstruction

In a simple rectilinear acquisition scheme, such as the classic spin echo pulse sequence, the phase encoding gradient is varied X times where X is the number columns of the resultant image. A 256x256 image would require 256 different phase encoding steps, and therefore 256 echoes would be acquired. The echoes are arranged in a 2D matrix known as k-space. The imaging equation can be formulated as:

$$S(k_x, k_y) = \int_{-\infty}^{\infty}\int_{-\infty}^{\infty} I(x,y)e^{-j2\pi(k_x x + k_y y)}dxdy, \tag{2.13}$$

where k_x and k_y belong to the set of points in k-space, and $I(x, y)$ is the desired image. Actual acquired data points in k-space are discrete. Assuming k-space sampling is uniform, Eq. 2.13 can be written as:

$$S[m,n] = S(m\Delta k_x, n\Delta k_y) = \int_{-\infty}^{\infty}\int_{-\infty}^{\infty} I(x,y)e^{-j2\pi(m\Delta k_x x + n\Delta k_y y)}dxdy,$$

where Δk_x and Δk_y are the k-space sampling intervals in the frequency encoding and phase encoding directions respectively, $m = \{-\infty, \ldots, -1, 0, 1, \ldots, \infty\}$ and $n = \{-\infty, \ldots, -1, 0, 1, \ldots, \infty\}$. Recall the Poisson formula which relates the coefficients of the Fourier series representation of a function with the periodic extension of its continuous Fourier transform:

$$\sum_{m=-\infty}^{\infty}\sum_{n=-\infty}^{\infty} S[m,n]e^{j2\pi(m\Delta k_x x + n\Delta k_y y)} = \frac{1}{\Delta k_x \Delta k_y}\sum_{m=-\infty}^{\infty}\sum_{n=-\infty}^{\infty} I(x - \frac{m}{\Delta k_x}, y - \frac{n}{\Delta k_y}).$$

In practice, $I(x, y)$ is limited by the field-of-view, that is, $I(x, y) = 0$ for $|x| > W_x/2$ and $|y| > W_y/2$. The number of data points acquired for the signal $S[m, n]$ is also finite, that is, $m = \{-M/2, \ldots, M/2\}$ and $n = \{-N/2, \ldots, N/2\}$. Since only a finite number of samples are available, the reconstructed image using the truncated signal is an approximation of the true image. $I(x, y)$ can be approximately recovered using:

$$I(x,y) = \Delta k_x \Delta k_y \sum_{m=-M/2}^{M/2-1}\sum_{n=-N/2}^{N/2-1} S[m,n]e^{j2\pi(m\Delta k_x x + n\Delta k_y y)},$$

where $|x| < 1/\Delta k_x$ and $|y| < 1/\Delta k_y$.

To ensure no aliasing will occur, the k-space sampling interval must be small enough to satisfy the Nyquist criterion. Consider $I(x, y)$ as a bandlimited signal with maximum frequencies given by $(M/2)\Delta k_x$ and $(N/2)\Delta k_y$. Then, to avoid aliasing, the pixel sizes in $I(x, y)$, Δx and Δy, must satisfy:

$$\Delta x \leqslant \frac{1}{M\Delta k_x},$$

and

$$\Delta y \leqslant \frac{1}{N\Delta k_y}.$$

At the maximum pixel size, a $M \times N$ image is obtained. That is, $I[p, q] = I(p\Delta x, q\Delta y)$ where $p = \{-M/2, \ldots, M/2\}$ and $q = \{-N/2, \ldots, N/2\}$. $I[p, q]$ can be obtained by evaluating the Discrete Fourier Transform (DFT) of $S[m, n]$:

$$I[p, q] = \Delta k_x \Delta k_y \sum_{m=-M/2}^{M/2-1} \sum_{n=-N/2}^{N/2-1} S[m, n] e^{j2\pi(mp/M+nq/N)},$$

for $-M/2 \leqslant u \leqslant M/2$ and $-N/2 \leqslant v \leqslant N/2$. Note that knowledge of Δk_x and Δk_y is not required for reconstruction. If both Δk_x and Δk_y are set to 1, then Δx and Δy are $1/M$ and $1/N$ respectively. The direct DFT reconstruction formula for MR images is then:

$$I[p, q] = \sum_{m=-M/2}^{M/2-1} \sum_{n=-N/2}^{N/2-1} S[m, n] e^{j2\pi(mp/M+nq/N)}. \tag{2.14}$$

Chapter 3

CRISP

3.1 Calculated Readout by Spectral Parallelism

CRISP is a parallel acquisition principle that can be implemented in MRI in several different ways. First is filterbank CRISP, where the MR signal from the receiver is passed through a comb of analog bandpass filters, converting one broadband channel into multiple narrowband channels, hence spectral parallelism. Each narrowband channel is individually captured with an analog-to-digital converter. In software, a weighted-addition of the narrowband channels is performed to recover the broadband signal, where the weights are the magnitude response profiles of the narrowband bandpass filters (calculated readout). The filter response profiles can be estimated by imaging a known, flat and uniform sample.

A second method of implementation is multi-coil CRISP, where multiple coils are placed physically adjacent to each other and each one is sensitive to a small region of the object. In this arrangement, the RF coils act as the bandpass filters, and the signal from each coil is considered narrowband. Each narrowband channel requires a separate RF receiver chain, in addition to the analog-to-digital converters. The broadband signal is recovered in similar fashion by weighted-addition of the narrowband channels, where the weights are now the response profiles of the RF coils, which again can be estimated by imaging a known, flat and uniform sample.

This thesis is mostly concerned with filterbank CRISP, the first proposed implementation. From this point onward, filterbank CRISP will be referred to simply as CRISP unless specified otherwise. The first section of this chapter will review the state of the art of parallel imaging techniques most relevant to CRISP. The second section will explore the benefits of CRISP in terms of signal-to-noise and sensitivity improvements, as well as the imaging scenarios where CRISP is expected to make a difference. Finally, some experimental and simulation results are presented.

3.2 State of the Art

Parallel MRI techniques, such as phased array coils, have been around since the 1980s [12], but became a popular research area only in the past decade [13]. Early parallel imaging techniques were more focused on improving image quality and signal-to-noise (SNR) using full field-of-view (FOV) acquisitions. Since then, improvements in hardware have led to higher magnetic field strengths (up to 7 Tesla for clinical use) and faster switching gradients, which means performance is now limited to a larger extent by physical and physiological concerns such as specific absorption rate (SAR) or peripheral nerve stimulation (PNS) [14]. Research and development have shifted toward accelerated imaging and image reconstruction algorithms such as PILS [15], SENSE [16], SMASH [17], and GRAPPA [18], all of which exploit known sensitivity information about a parallel array of receive coils in order to reconstruct images from undersampled k-space. It is of note here that fundamentally, all these methods achieve accelerated imaging at the cost of reduced SNR [13]. The above algorithms can be roughly divided into two categories: image-domain methods (PILS, SENSE) and k-space methods (SMASH, GRAPPA). Since CRISP is an image-domain method, only PILS and SENSE will be described here for comparison.

Partially Parallel Imaging with Localized Sensitivity (PILS) assumes that each component coil in an array of surface coils is sensitive only to a localized region of space along the phase encoding (y) direction. If the full field-of-view (FOV) to avoid aliasing in the phase encoding direction is Y_i, then a coil with localized sensitivity is restricted to receiving signal from a region of size Y_c, where $Y_c < Y_i$, centered at y_0 where the coil is physically located. In this case, the FOV can be reduced to Y_c without aliasing problems. The reduction in FOV translates to a reduction in scan time since less phase encoding steps are required.

SENSivity Encoding (SENSE) can be described as a method to "unfold" aliased pixels in image space. FOV is reduced as a result of undersampling k-space to accelerate imaging. Aliasing occurs when a full FOV image is reconstructed from the reduced FOV data from a component coil. Each pixel in the intermediate images resulting from the component coils is a linear combination of equidistant pixels in the full FOV image, weighted by the coil sensitivity at the corresponding pixel locations. The signal at location (x,y) of the kth component coil can be written as [14]:

$$I_k(x,y) = C_k(x,y_1)\rho(x,y_1) + C_k(x,y_2)\rho(x,y_2) + \cdots + C_k(x,y_R)\rho(x,y_R)$$

where k counts from 1 to N_c, the number of coils used, and R is the number of aliased pixels in the full FOV image. $C_k(x,y_1)$ is the coil sensitivity for coil k at pixel location (x,y_1). $\rho(x,y_1)$ is the desired pixel value at (x,y_1). $I_k(x,y)$ is the pixel value at (x,y) of the aliased image from coil k. Combining all N_c coils results in a set of N_c linear equations, with R unknowns:

$$\vec{I} = \mathbf{C} \cdot \tilde{\rho} \tag{3.1}$$

$\vec{I}$ is a length N_c vector containing the value of one chosen pixel for each of the N_c coils. $\mathbf{C}$ is a $N_c \times R$ matrix with coil sensitivities at each of the R locations. R must not be greater than N_c in order to solve the system. Solving Eq. 3.1 is generally possible if the matrix inverse of $\mathbf{C}$ can be found or approximated.

3.3 Comparison to CRISP

PILS and SENSE are similar to CRISP in the sense that the final image is a combination of multiple intermediate images obtained from reduced FOV signals. In PILS and SENSE, each component receiver coil could be seen as a analog bandpass filter in the phase encoding direction [15]. The intermediate images are obtained from the signal of each coil. In filterbank CRISP, the signal from one coil is filtered into multiple narrower bandwidth channels using analog bandpass filters, and the intermediate images are derived from the signal of each of those narrowband channels. In the current implementation of CRISP, only one receiver coil is used, but in principle it is easily extendible to multiple coils by duplicating the entire receiver chain for each coil. CRISP on its own is not an accelerated imaging technique; it does not reduce the number of echoes required. It can, however, reduce the sampling requirement for echoes, such that a smaller number of data points is necessary to capture the signals from each narrowband channel when compared to the original broadband signal.

Fig. 3.1(a) and 3.1(b) illustrate some of the similarities and differences between PILS, SENSE and CRISP. PILS and SENSE require coil sensitivity profiles along the phase encoding direction, while filterbank CRISP requires bandpass filter response profiles along the readout or frequency encoding direction. The intermediate images for PILS and SENSE have reduced FOV in the phase encoding direction, while the intermediate images for CRISP have reduced FOV in the frequency encoding direction. In PILS and SENSE, the bandwidth of the signals from each coil just before the analog-to-digital converter (ADC) does not change. In CRISP, the ADC sees a smaller bandwidth due to the preceding bandpass filter.

3.4 CRISP Reconstruction

In this implementation of filterbank CRISP, the broadband MR signal is processed with a comb of analog bandpass filters, converting it into multiple narrowband signals. Each individual narrowband signal is acquired with an ADC and the final image is reconstructed in software using a weighted addition of intermediate images derived from the narrowband signals. As shown in Fig. 3.1(b), CRISP requires the bandpass filter frequency response

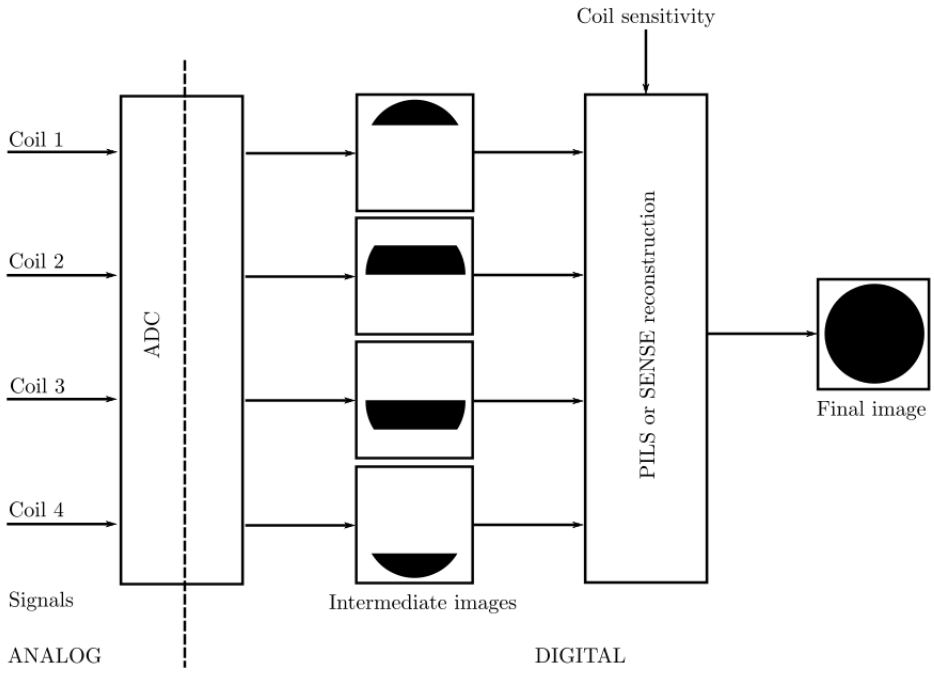

(a) PILS/SENSE

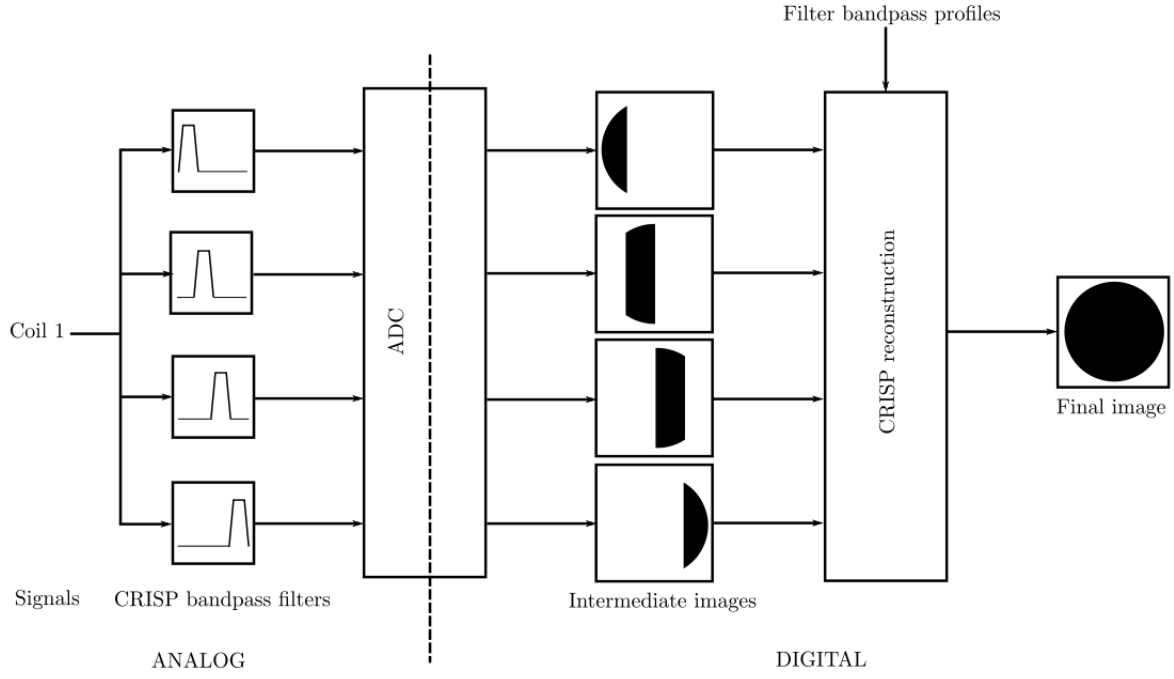

(b) CRISP

Figure 3.1: Simplified signal flow for (a) SENSE and PILS reconstruction and (b) CRISP reconstruction.

profiles in order to perform the reconstruction of the final image. These profiles are estimated using an object with flat and consistent response across the frequency direction.

The bandpass estimation and the image reconstruction process is illustrated with a concrete example; a water phantom acquired using the CRISP receiver chain, with four bandpass filters, is shown in Fig. 3.2, where the four partial field-of-view images are reconstructed from data from the four narrowband bandpass channels respectively. The region that will be used for bandpass response estimation is highlighted. An image of the same phantom acquired without CRISP narrowband filters is shown in Fig. 3.3 for reference. For each narrowband channel, the rows in the highlighted region are averaged to obtain the response profile corresponding to that filter. Four response curves are obtained, one for each filter, as illustrated in Fig. 3.4.

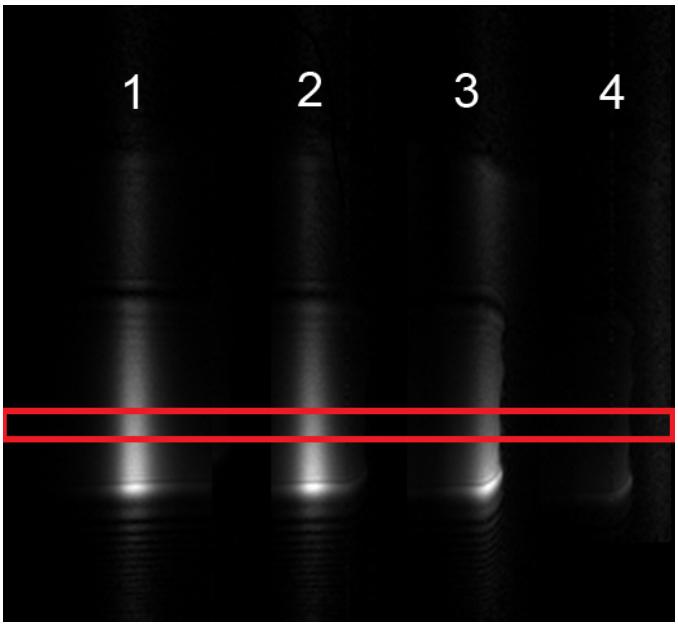

Figure 3.2: CRISP intermediate images from four bandpass filtered signals. The image region used to estimate bandpass filter response is highlighted.

Mathematically, the bandpass estimation can be described, in 1D, as follows. Let $F(\omega)$ represent the known, flat and uniform calibration image. That is, $F(\omega) = 1$ inside the field-of-view and $F(\omega) = 0$ elsewhere. Bandpass filter i has unknown response $B_i(\omega)$, and $i = \{0, 1, \ldots, N\}$, where N is the total number of bandpass filters. Filtering the signal gives the bandpass frequency response:

$$F(\omega)B_i(\omega) = B_i(\omega),$$

for $i = \{0, 1, \ldots, N\}$. The process is the same for all rows of all images. Let $B_{ij}(\omega)$ be the

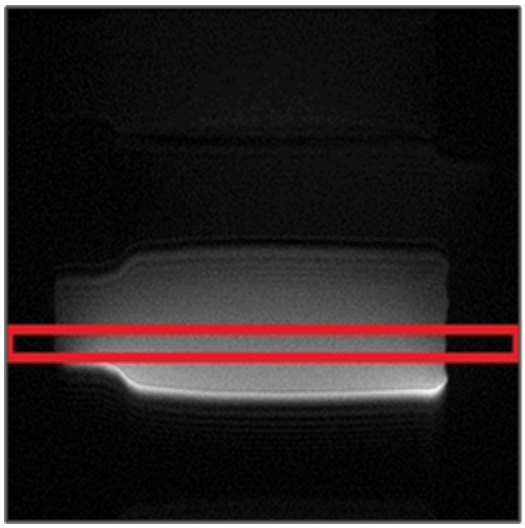

Figure 3.3: Image of the calibration water phantom acquired without CRISP bandpass filters. Region used to estimate bandpass filter response is highlighted.

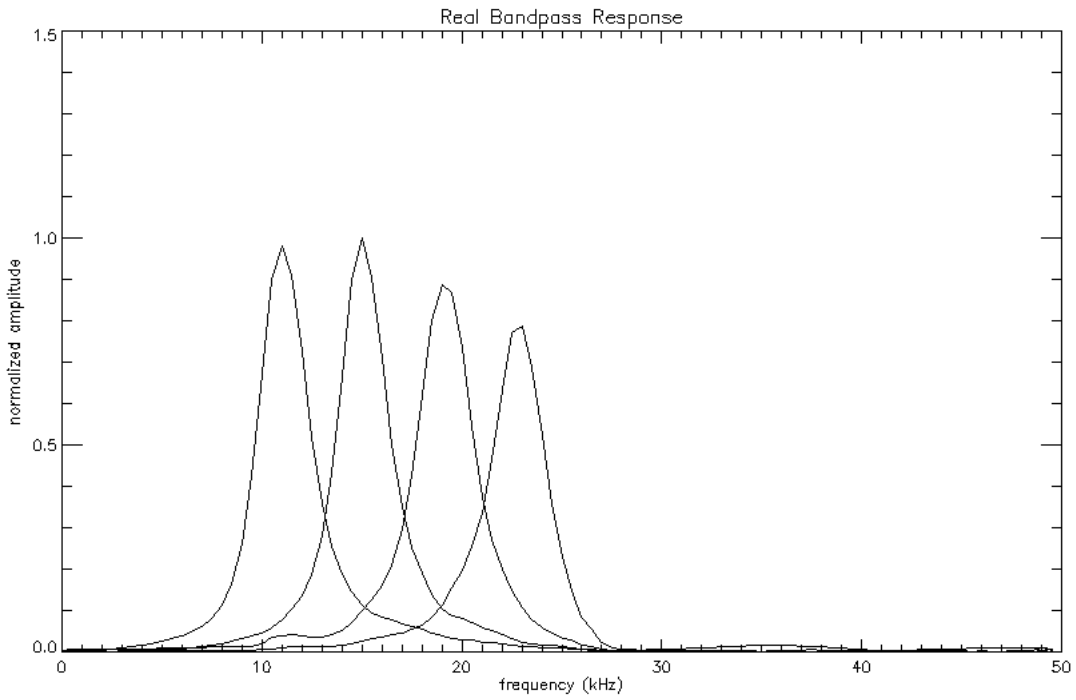

Figure 3.4: CRISP bandpass filter response profiles.

profile obtained for filter i using row j of channel i. The estimated bandpass response is:

$$\hat{B}_i(\omega) = \frac{\sum_{j=row_s}^{row_e} B_{ij}(\omega)}{row_e - row_s + 1}.$$

where row_s and row_e are the start and end row indices respectively. The start and end rows define the region used to estimate bandpass response profiles and are chosen by visual inspection of the unfiltered image to determine the flattest, most uniform region possible.

With the filter profiles, weighted addition is performed on the intermediate images in Fig. 3.2. Let $S(\omega)$ represent the spectrum of the noiseless signal and $N(\omega)$ the noise spectrum. The total signal spectrum, $F(\omega)$, over the entire bandwidth, BW, is then:

$$F(\omega) = S(\omega) + N(\omega),$$

where additive noise is assumed. Let $B_i(\omega)$ be the shape of bandpass filter i, centered at frequency ω_i, with bandwidth BW_i, and $i = \{1, \ldots, N\}$, where N is the total number of bandpass filters. Also, assume the estimated bandpass response is a good approximation to the true bandpass response, that is, $\hat{B}_i(\omega) \simeq B_i(\omega)$. Let $G_i(\omega)$ be the resulting signal filtered with bandpass i, that is

$$\begin{aligned} G_i(\omega) &= F(\omega) \cdot B_i(\omega) \\ &= [S(\omega) + N(\omega)] \cdot B_i(\omega) \\ &= S(\omega)B_i(\omega) + N(\omega)B_i(\omega). \end{aligned}$$

Weighted addition is then used to reconstruct the image. Let $H(\omega)$ be the reconstructed image. The acquired signals $G_i(\omega)$ are multiplied by the bandpass responses and divided

by the sum of the square of the bandpass responses for normalization:

$$
\begin{aligned}
H(\omega) &= \frac{\sum_{i=1}^{N} G_i(\omega) B_i(\omega)}{\sum_{i=1}^{N} B_i^2(\omega)} \\
&= \frac{\sum_{i=1}^{N} S(\omega) B_i^2(\omega)}{\sum_{i=1}^{N} B_i^2(\omega)} + \frac{\sum_{i=1}^{N} N(\omega) B_i^2(\omega)}{\sum_{i=1}^{N} B_i^2(\omega)} \qquad (3.2) \\
&= S(\omega) \frac{\sum_{i=1}^{N} B_i^2(\omega)}{\sum_{i=1}^{N} B_i^2(\omega)} + N(\omega) \frac{\sum_{i=1}^{N} B_i^2(\omega)}{\sum_{i=1}^{N} B_i^2(\omega)} \qquad (3.3) \\
&= S(\omega) + N(\omega).
\end{aligned}
$$

Therefore, the original signal and noise is recovered exactly. Equality between Eq. 3.2 and Eq. 3.3 is justified by the assumptions that both signal and noise are filtered in the same manner [19], and that noise is independent from signal and the effects of filtering. This is the case if the signal is filtered in the digital domain, where no effect on SNR would be observed. Therefore, in order to observe an SNR improvement with CRISP reconstruction using bandpass filters, the signal should be filtered in the analog domain. This separates CRISP from other digital filterbank reconstruction techniques in the past [20]. The reconstructed image is shown in Fig. 3.5(c), along with an image reconstructed without weighted addition, Fig. 3.5(b), and an unfiltered reference image, Fig. 3.5(a).

3.5 Signal-to-Noise Improvement

An argument for SNR improvement is presented here. The following assumptions are made:

1. Noise, $N(\omega)$, is dependent on signal bandwidth. As a simplifying assumption, noise is assumed to be equal to the square root of the bandwidth, BW, of the initial bandlimited signal, $S(\omega)$. The total signal is $S(\omega) + N(\omega)$.

2. A comb of N ideal bandpass filters are used, where the filter response of filter i is $B_i(\omega) = 1$ within the filter passband, BW_i, and 0 elsewhere. BW_i is identical for all i filters.

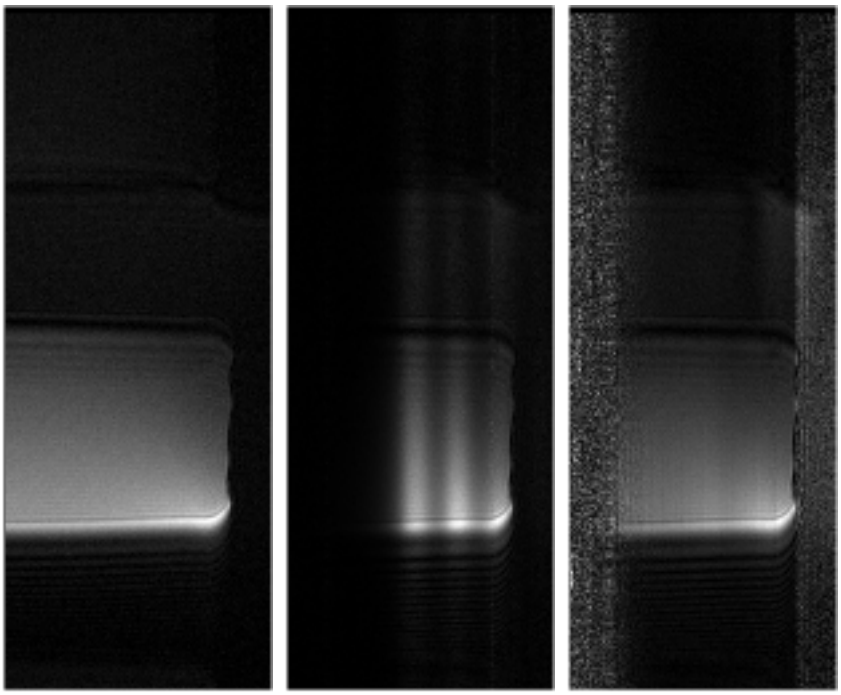

(a) Unfiltered (b) Simple add (c) Weighted add

Figure 3.5: CRISP reconstruction. In (c), noise outside of the FOV is amplified due to the weighted-add reconstruction.

3. The combined passband of all bandpass filters span the entire bandwidth, BW, of the initial signal.

4. Bandpass filter i only allows frequencies within its passband, BW_i to pass through, and attenuates all other frequencies.

5. Signal, $S(\omega)$, passing through the filter is unchanged, and can be recovered exactly.

6. As a corollary to Assumption 1, noise, $N_i(\omega)$, at the output of filter i is equal to the square root of the output signal bandwidth, $\sqrt{BW_i}$.

Given the above assumptions, passing through bandpass filter i, $S(\omega)$ is unchanged in the passband of the filter BW_i, but the noise has changed from $\sqrt{BW}$ to $\sqrt{BW_i}$:

$$\frac{noise\ at\ filter\ output}{noise\ at\ filter\ input} = \frac{\sqrt{BW_i}}{\sqrt{BW}}.$$

With N identical ideal filters available, the bandwidth of each filter is $1/N$ of the bandwidth of the initial signal.

$$\frac{\sqrt{BW_i}}{\sqrt{BW}} = \frac{1}{\sqrt{N}}.$$

Therefore, the noise in each narrowband channel is reduced by $\sqrt{N}$. Since signal is unaffected by the reconstruction and can be recovered exactly, the SNR of the total reconstructed signal compared to the total original signal is increased by a factor of $\sqrt{N}$.

In other words, CRISP targets noise that exhibit dependence on signal bandwidth. If there exists an RMS noise voltage per unit frequency present in the signal, the noise value is determined by multiplying the RMS noise voltage per unit frequency by $\sqrt{BW}$ where BW is the total bandwidth of the initial signal. If BW is divided into N by N equal filters with bandwidth BW_i, then the noise voltage at the output of each filter is $1/\sqrt{N}$ of the initial noise value. The part of the signal that lies in the bandwidth of the filters passes through and is used to fully reconstruct the original signal. In other words, the signal is unchanged, but the noise has been reduced by $\sqrt{N}$. Therefore, SNR is increased by $\sqrt{N}$.

A subtle point to note is that in order for the filters to have an effect on SNR, the noise must occur after the signal has been reduced in power, that is, after bandpass filtering. Filterbank CRISP has minimal impact on noise occurring before filtering, which is another argument for analog filtering over digital filtering since no further noise is added after signal digitization.

3.6 Sensitivity Improvement

Recall the relationship between the bandwidth of a signal and its echo. For narrowband filtered signals, the duration of the echo is extended in comparison to the original unfiltered

signal. This idea is illustrated in Fig. 2.7 in chapter 2, where the top signal is the unfiltered broadband signal, and the bottom two are signals from two different narrowband CRISP channels. In short T_2 relaxation scenarios with noise, the signal decays rapidly into the noise floor, and information may be lost. The reduction in decay rate allows for more signal to be acquired over time. This is demonstrated with the following experiment where MR data is acquired with a broadband filter and with a bank of narrowband filters. Digitization with varying bit levels is simulated using this data.

3.6.1 Experiment and Simulation Results

A small onion sample is imaged on a Bruker 11.7 T NMR magnet. The MR signal is downconverted using the Bruker receiver chain and then processed using either the CRISP narrowband bandpass filters or a broadband filter. A 16-bit analog-to-digital converter is used to acquired the 16-bit signals shown in Fig. 3.6(a) and 3.6(b). The corresponding reconstructed images are shown in Fig. 3.7(a) and 3.7(b). The 8-bit and 5-bit signals are simulated from the original 16-bit signals. Figures on the left in Fig. 3.6 show signals from the output of one of the CRISP narrowband filters, while figures on the right show the signals after a broadband filter. The broadband signal, with many frequency components, exhibits a fast decay rate, while a narrowband signal, with fewer frequency components, decays much more slowly. The difference is most apparent at the 5-bit level, where the CRISP narrowband signal avoids being digitized to zero for a longer period of time than the broadband signal. Fig. 3.7 shows the corresponding reconstructed images for each of the signals in Fig. 3.6.

Furthermore, when digitizing analog signals, such as an MR echo, it is beneficial to set the maximum input range of the ADC to the maximum peak of the signal. That is, if the peak signal is +5V, and the ADC is 16-bits, $2^{15} = 32768$ represents +5V and -32768 represents -5V. Each bit-level is then $1/32768 \times 5\text{V} = 0.153$ mV. Using the same 16-bit ADC for a signal with maximum peak to peak of ± 2.5V, each bit now represents 0.076 mV, making it more sensitive to smaller signals. In CRISP, by splitting a broadband signal into multiple narrowband signals, the signal peak in each channel is lower and the power is spread over a longer period of time. Therefore, the signal can be amplified and the full range of the ADC can be used more effectively. In short T_2 cases, where the signal is sharply peaked and decays rapidly, CRISP is expected to lead to an improvement in image quality.

3.7 Conclusion

In this chapter, recent MR image reconstruction methods were discussed; focus was given to PILS and SENSE since they are image-domain methods like CRISP. Their similarities

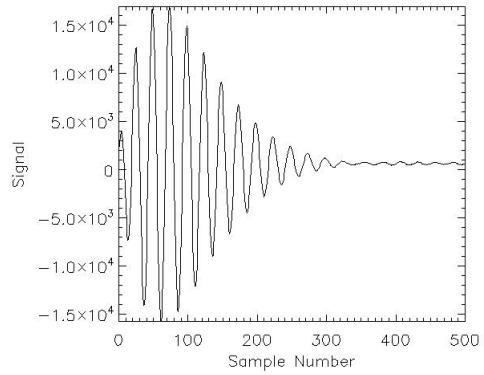

(a) One channel of CRISP 16-bit

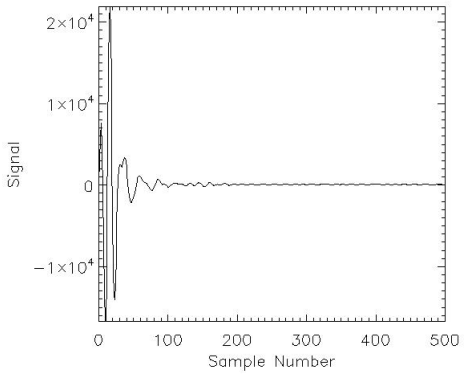

(b) Broadband 16-bit

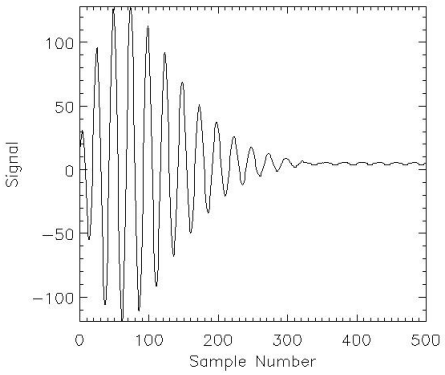

(c) One channel of CRISP 8-bit

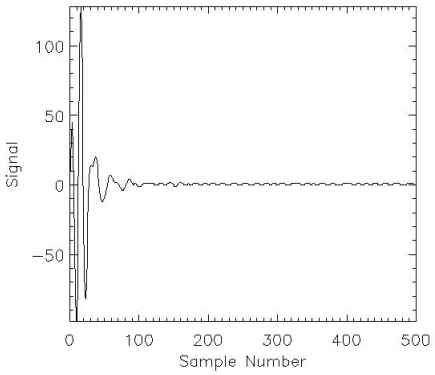

(d) Broadband 8-bit

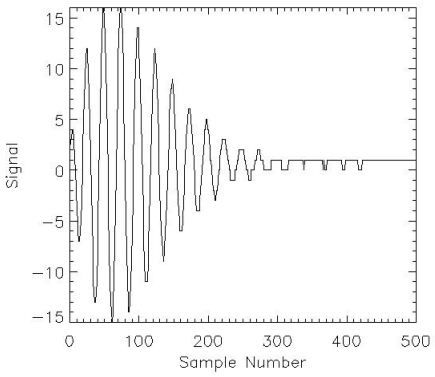

(e) One channel of CRISP 5-bit

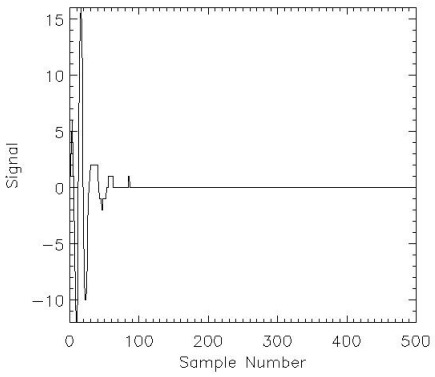

(f) Broadband 5-bit

Figure 3.6: Low-bit level digitization simulation FIDs from an onion sample. Sampling rate was 500 kHz, therefore, each tick on the x-axis represent 2 μs.

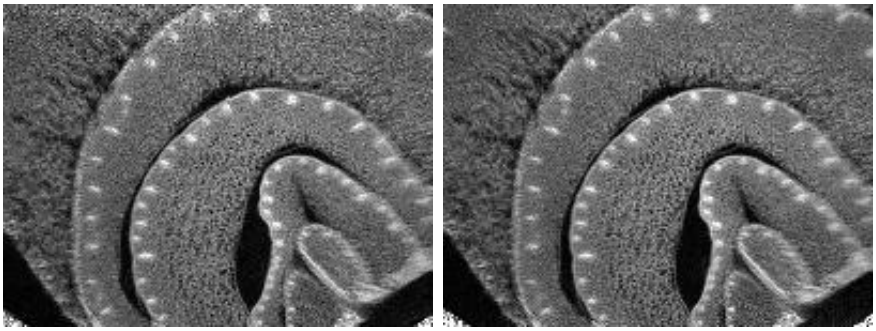

(a) CRISP 16-bit (b) Broadband 16-bit

(c) CRISP 8-bit (d) Broadband 8-bit

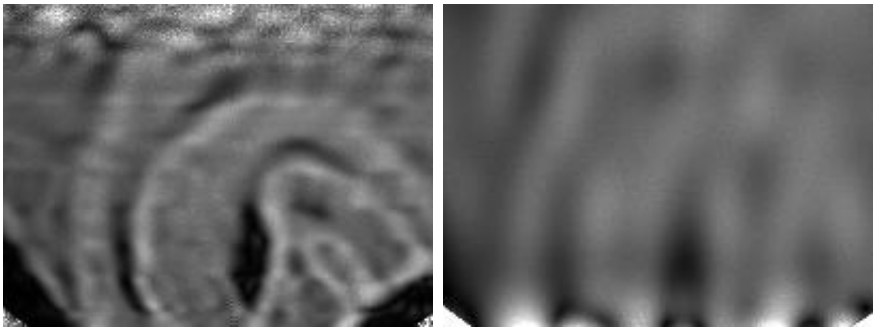

(e) CRISP 5-bit (f) Broadband 5-bit

Figure 3.7: Low-bit level digitization simulation images from an onion sample.

and differences were highlighted. Filterbank CRISP was explained and an argument for SNR improvement formalized. Assuming bandwidth dependent noise, such as thermal noise, occurring after the CRISP bandpass filters, CRISP offers an upper bound of $\sqrt{N}$ SNR improvement over traditional acquisition and reconstruction methods. An argument for analog hardware filtering was given, based on the fact that digital filtering affect both signal and noise in the same way and does not reduce the bandwidth dependent noise that occurs after filtering. Simulation results that demonstrate sensitivity improvement due to the extended duration of echoes/FIDs acquired with filterbank CRISP versus traditional broadband acquisition were shown.

Chapter 4

RF Receiver Chain

While working with Sergei Obruchkov on a 3T MRI system[1], it was determined that the system digitizes the MR signal at 2.25 MHz. Therefore, an analog MR signal lower than 2.25 MHz is not available. Thus, the goal for the custom receiver chain is to receive the raw MR signal, and down-convert it to a lower frequency of choice for filtering with CRISP bandpass filters. The custom receiver chain will from now on be referred to as the CRISP receiver chain, to eliminate confusion with the receiver chain in the clinical system.

This chapter will introduce the electronic components required to implement a custom RF receiver chain in order to capture a magnetic resonance signal from a clinical MRI system. Experimental results comparing the images acquired with the custom receiver chain and the clinical system will be presented.

In general, a simple RF receiver chain for MR consists of five main components: 1) (pre-)amplifiers, 2) RF receiver (demodulator/mixer), 3) local oscillator (LO), 4) filters and attenuators, 5) analog-to-digital converters (ADC). In the CRISP receiver chain, the input MR signal is obtained by splitting the signal from the clinical system after amplification by low-noise pre-amplifiers. An NMR RF receiver demodulates the signal using a local oscillator as the reference. The result is acquired with an analog-to-digital converter and finally, the image is reconstructed in software.

4.1 Input Signal

The input MR signal is a bandlimited signal, modulated with a carrier frequency ω_c equal to the Larmor frequency ω_0.

$$\omega_0 = \begin{cases} 63.864\ MHz & \text{for } B_0 = 1.5\ T \\ 127.728\ MHz & \text{for } B_0 = 3.0\ T \end{cases}$$

[1]Imaging Research Center at St. Joseph's Hospital in Hamilton, Ontario.

The bandwidth of the signal is typically 31.25 kHz and is at -65 dBm (or 128 μV_{rms} or 356 μV_{pk-pk} at 50Ω impedance) just after the receive coils. Fig. 4.1 plots the complex MR signal spectrum, and Fig. 4.2 plots the signal received by an RF detect coil. Note that the spectrum is symmetric about zero since the signal is real.

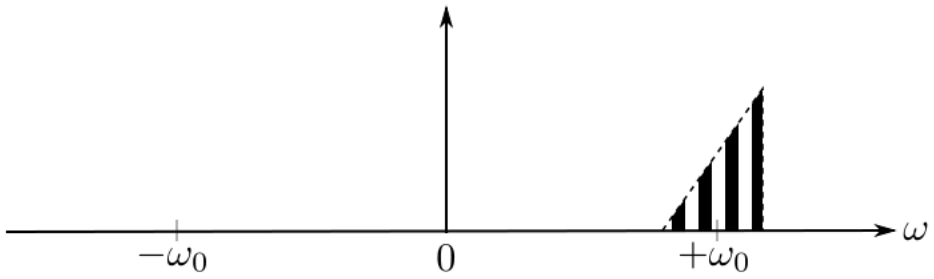

Figure 4.1: Complex MR signal.

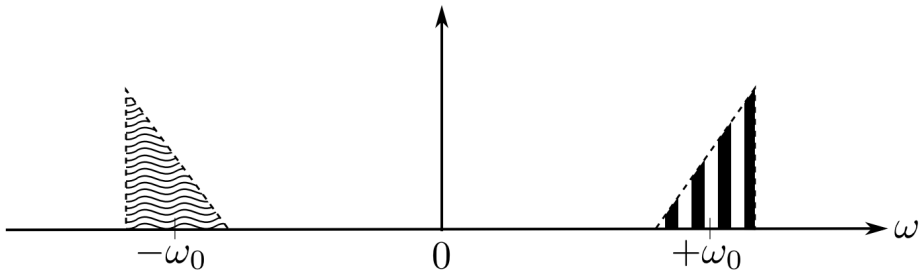

Figure 4.2: The signal received by an RF coil.

Accessing the raw signal in a clinical system requires either 1) directly soldering a connection on the circuit board of the RF coil and running a cable from the magnet room to the adjacent equipment room, or 2) identifying and intercepting the correct signal in the equipment room using a power splitter. With the assistance of Ken Bradshaw[2], the first method is implemented. An important detail of note is the insertion of an RF choke on the coaxial cable carrying the MR signal from the magnet room to the equipment room. The choke significantly improved signal quality and allowed for images to be captured. The second method does not require a cable from the magnet room to the equipment room, but it does require some trial and error to locate the correct signal and access to special RF connectors and adaptors.

[2]Sentinelle Medical Inc.

4.2 RF Receiver

At the heart of the receiver chain is the RF receiver, which performs the downconversion and demodulation of the signal. RF receivers in general can be split into two main architectures: heterodyne and homodyne. Heterodyne receivers (Fig. 4.3) downconvert the incoming RF signal down to an intermediate frequency (IF) first, then downconvert a second time from IF to baseband [21]. Some heterodyne receivers digitize the IF signal directly with an analog-to-digital converter, and perform the final demodulation stage in software [22]. Homodyne receivers (Fig. 4.4) downconvert RF signals directly to baseband [21]. Many RF communication systems, such as AM/FM radios, use the heterodyne architecture [23], and MRI systems are no exception. The exact IF depend on the specific system design and implementation, but is 2.25 MHz for the clinical system that is used for experiments here.

Fig. 4.5 illustrates one possible implementation of CRISP receiver chain using the homodyne architecture. The lowpass filters in Fig. 4.4 are replaced with two identical banks of four narrowband bandpass filters, one for the real and one for the imaginary channel. The outputs are fed into an analog-to-digital converter with eight simultaneous inputs.

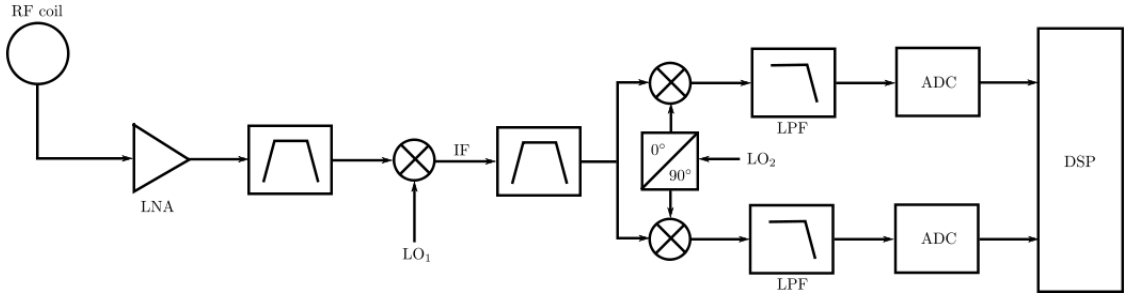

Figure 4.3: Simple heterodyne receiver chain. [21]

An NMR receiver is used for the CRISP receiver chain. The receiver has two independent I/Q channels, each with a double balanced mixer (SBL1-1) from Mini-circuits with broadband amplifiers with adjustable gain and a lowpass filter with cutoff frequency ≈ 1 MHz.

4.3 Quadrature Detection

The MR signal as received by a single RF coil is shown in Fig. 4.2. However, the complex signal with only positive frequencies, as shown in Fig. 4.1, is desired. Mixing with a simple $cos(\omega_0 t)$ results in the scenario in Fig. 4.6 where the positive and negative images are aliased together. Now consider the complex signal, $e^{-j\omega_0 t}$. According to Euler's formula,

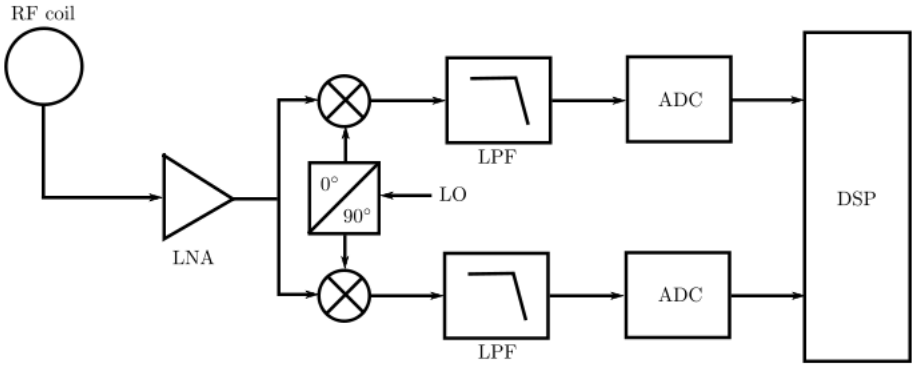

Figure 4.4: Simple homodyne receiver chain. [21]

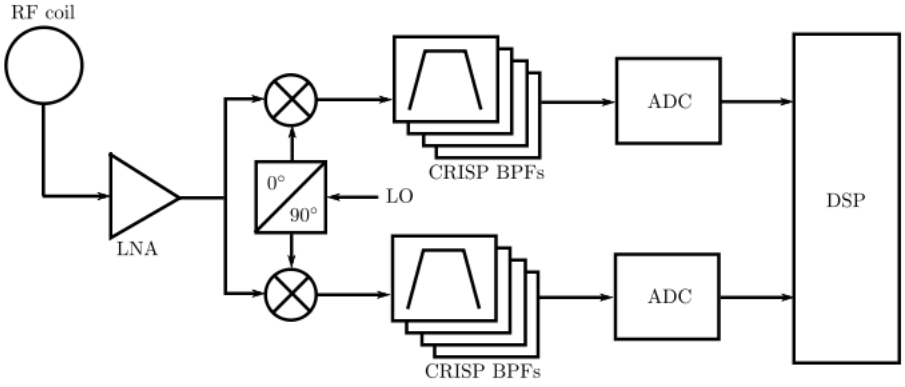

Figure 4.5: Simple receiver chain with CRISP filterbank.

$e^{-j\omega_0 t}$ decomposes into $cos(\omega_0 t) - jsin(\omega_0 t)$, which is a pair of sinusoids, one in-phase (the real or I channel) and the other in quadrature, or out of phase by 90° (the imaginary or Q channel). Using this I/Q pair as reference, the positive frequency signal can be recovered, as illustrated in Fig. 4.7. This is known as quadrature detection [6, 7].

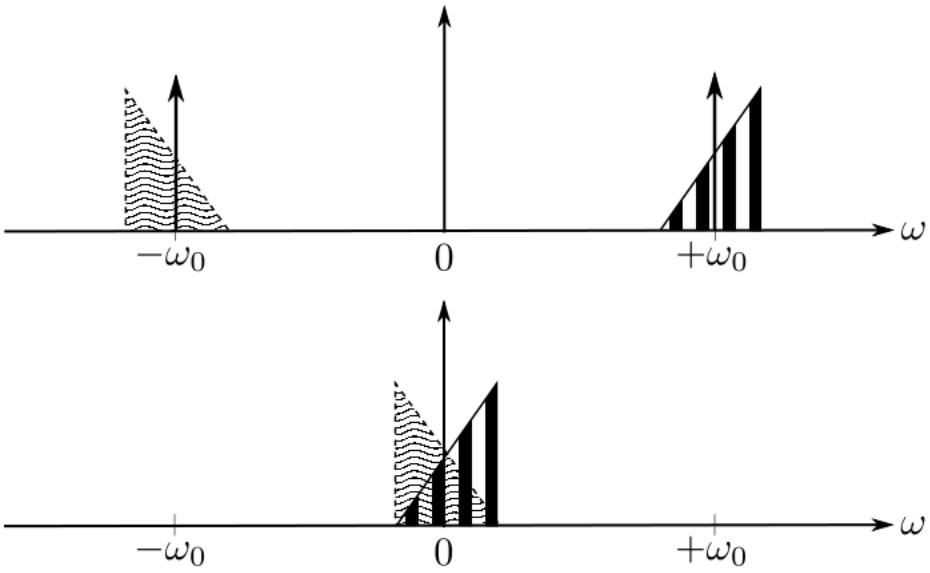

Figure 4.6: Demodulation with real signal $cos(\omega_0 t)$. Note the aliased demodulated baseband image.

4.3.1 Analog Quadrature Correction

The real (I) and imaginary (Q) component pairs of complex data should be located on perpendicular axes in the complex plane. However, when the phase difference between the I/Q pair is not 90°, the negative frequency component of the acquired data will not cancel properly. Rather than ideal case where $cos(\omega_0 t) - jsin(\omega_0 t) = e^{-j\omega_0 t}$, mismatch between pair of quadrature signals results in an additional $e^{j\omega_0 t}$ term [21]. Consider the case where θ represents the error in phase away from quadrature:

$$\begin{aligned} cos(\omega_0 t) - jsin(\omega_0 t + \theta) &= \frac{1}{2}\left[e^{j\omega_0 t} + e^{-j\omega_0 t}\right] - \frac{1}{2}\left[e^{j(\omega_0 t+\theta)} - e^{-j(\omega_0 t+\theta)}\right] \\ &= \frac{1}{2}\left[1 - e^{j\theta}\right] e^{j\omega_0 t} + \frac{1}{2}\left[1 + e^{-j\theta}\right] e^{-j\omega_0 t}. \end{aligned}$$

Quadrature pair mismatch results in a flipped and upside down version of the image superimposed on the desired image. The effect of quadrature mismatch is illustrated in Fig. 4.9(a) with an image of a water phantom acquired with the CRISP receiver chain.

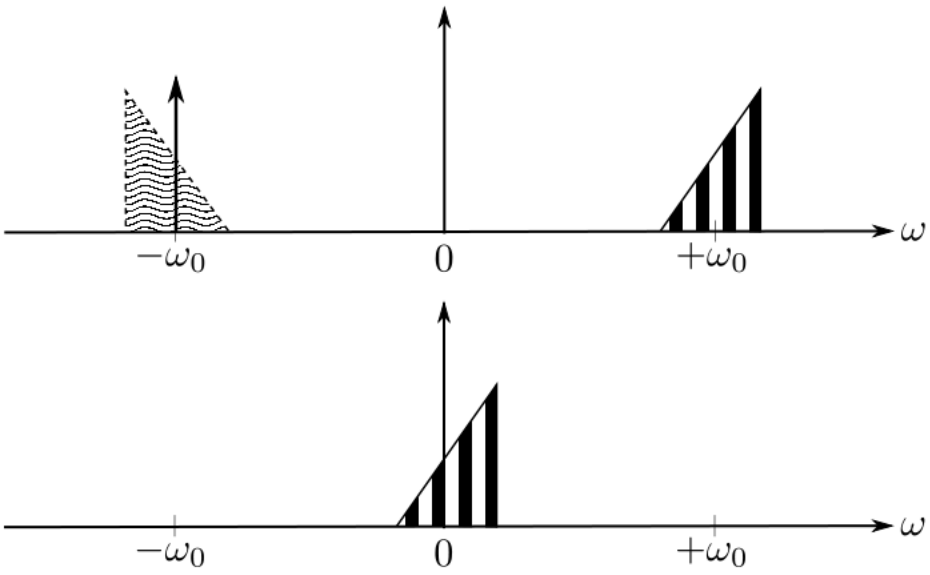

Figure 4.7: Demodulation with complex signal $e^{-j\omega_0 t}$. Note the unaliased baseband image.

The I and Q channels only need to be phase-shifted 90° *relative* to each other and therefore, misalignment could be corrected to some extent in software after data acquisition. Fig. 4.8 plots phasor x on the complex plane. The real component of x, R, is assumed to be correct. The correct real and imaginary components for x is R and I_{cor} respectively. In other words, R and I_{cor} are the data points that should have been acquired if the I and Q channels are exactly in quadrature. But due to quadrature mismatch, the actual data collected is R and I_{inc}. θ is the difference in angle between the correct and incorrect imaginary axis and ϕ is the angle of the phasor x with respect to the correct imaginary axis.

The following equations can be derived from trigonometry:

$$\frac{I_{inc}}{x} = cos(\phi - \theta) \tag{4.1a}$$

$$\frac{R}{x} = sin(\phi) \tag{4.1b}$$

$$\frac{I_{cor}}{x} = cos(\phi). \tag{4.1c}$$

Using the identity $cos(\phi - \theta) = cos(\phi)cos(\theta) + sin(\phi)sin(\theta)$ and Eg. 4.1a, 4.1b, and 4.1c, the equation for correcting quadrature mismatch can be written as:

$$I_{cor} = \frac{I_{inc} - Rsin(\theta)}{cos(\theta)}. \tag{4.2}$$

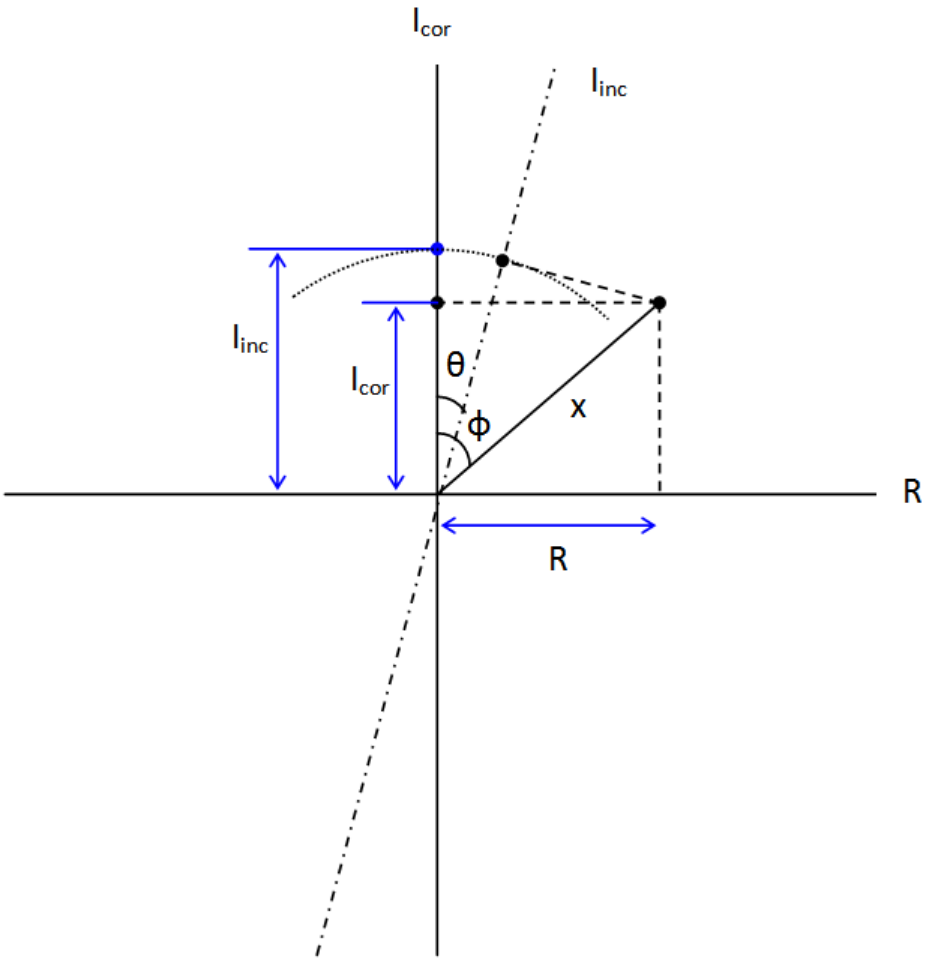

Figure 4.8: Correcting for quadrature mismatch - here, the real channel is assumed to be "correct", R and I_{cor} are the correct real (I) and imaginary (Q) axes, I_{inc} is the incorrect imaginary axis that data was acquired on, x is the magnitude of the phasor that is being acquired, and θ is the error in degrees away from exact quadrature.

In matrix form:

$$\begin{bmatrix} R \\ I_{cor} \end{bmatrix} = \begin{bmatrix} 1 & 0 \\ -tan(\theta) & sec(\theta) \end{bmatrix} \begin{bmatrix} R \\ I_{inc} \end{bmatrix}. \tag{4.3}$$

Fig. 4.9(b) shows the image after the correction is applied. The quadrature ghost image is much less visible in the corrected result, but not completely eliminated. This could be due to the fact that the angle θ was not known exactly, and trial-and-error was used to find an approximate solution. This process also highlights the point that it is difficult to generate the I and Q channels in exact quadrature without additional stabilization circuits, and that once the data has been acquired imperfectly, it may not be possible to recover the signal perfectly again.

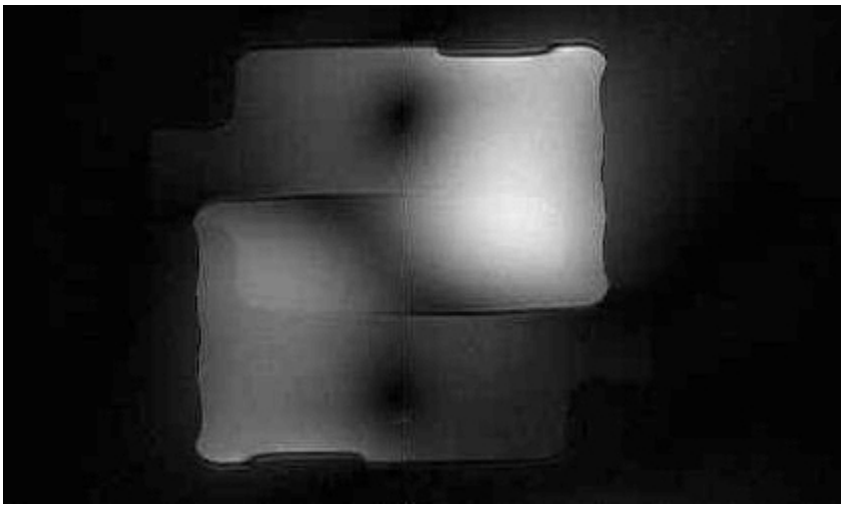

(a) Without correction

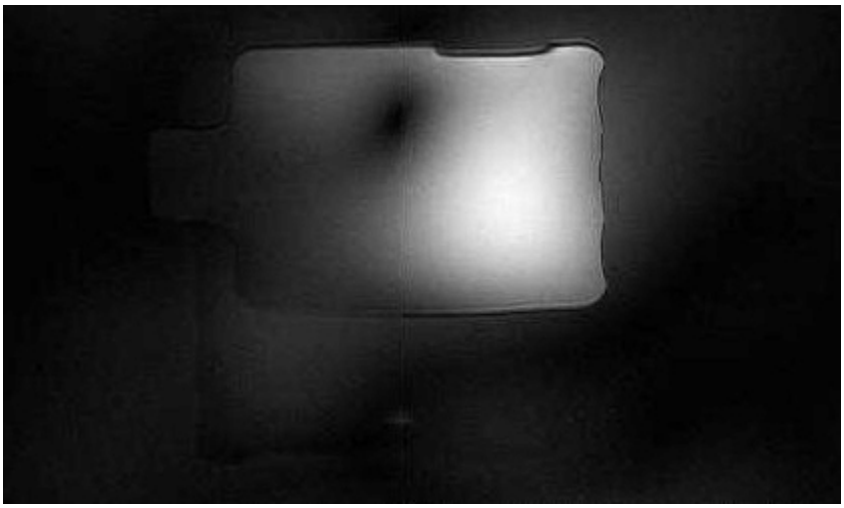

(b) With correction

Figure 4.9: Reconstructed images with mismatched quadrature reference pair.

4.3.2 Digital Quadrature Detection

Digital quadrature detection is one possible alternative to avoid the inefficiencies and difficulties of quadrature detection in the analog domain. The premise is to sample the signal at four times the center frequency of the image [24, 25], and at the same time ensuring that the sampling rate satisfies the Nyquist criterion.[3] To give a concrete example, assume the signal of interest is a real-valued bandpass signal centered at 32 kHz with 32 kHz bandwidth, as shown in Fig. 4.10.

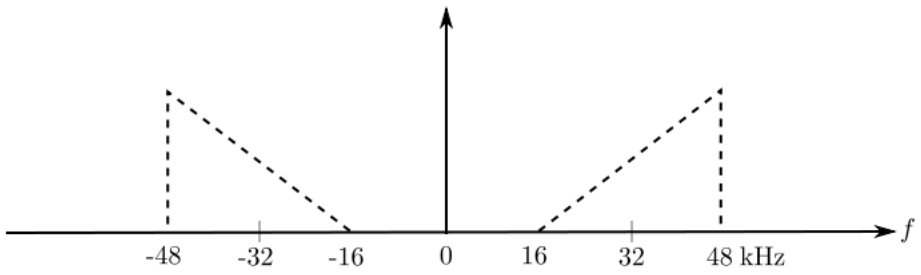

Figure 4.10: Digital quadrature detection example signal spectrum.

Demodulation of this signal requires the quadrature reference pair $sin(2\pi f_c t)$ and $cos(2\pi f_c t)$, where $f_c = 32$ kHz. If sampling rate is set at four times f_c, or 128 kHz, the nth sample correspond to time $t = n/128$ kHz. The quadrature reference signals now becomes $sin(2\pi n/4)$ and $cos(2\pi n/4)$. Table 4.1 shows the first few values of both of these reference signals. As a result of this choice of sampling rate, all the even numbered samples belong to the I channel and all the odd numbered samples belong to the Q channel. Since the original analog signal was sampled at 128 kHz, the sampling rate in the I and Q channels is 64 kHz, which is twice the bandwidth (32 kHz) and therefore satisfies the Nyquist condition.

Table 4.1: Digital quadrature reference signal values from $n = 0$ to 7.

n	0	1	2	3	4	5	6	7
$cos(2\pi n/4)$	1	0	-1	0	1	0	-1	0
$sin(2\pi n/4)$	0	1	0	-1	0	1	0	-1

[3]Nyquist rate is the lower limit on sampling rate to prevent aliasing. Nyquist frequency is the maximum frequency representable by sampling at the Nyquist rate

4.4 Local Oscillator

In an MR system, the local oscillator, often generated using a frequency synthesizer, is needed for transmission of the RF excitation pulses, and also for demodulation of the RF signal during receive. In order to receive an MR signal from the clinical system, the CRISP receiver chain needs a local oscillator from either 1) the clinical system itself, or 2) a separate frequency synthesizer.

The frequency of the local oscillator from the clinical system unfortunately is not on resonance due to its heterodyne receiver chain design. Instead, it oscillates at 2.25 MHz above the center frequency during the readout period, when data acquisition occurs. Mixing the MR signal with this local oscillator results in an IF signal centered at 2.25 MHz, which is incompatible with the NMR RF receiver due to a built-in low-pass filter with $f_{cutoff} \approx 1$ MHz at its output.

For the sake of compatibility with existing equipment and flexibility of selecting any desired IF frequency, a separate frequency synthesizer is used. The CRISP receiver chain uses the PTS 500, from Programmed Test Sources, which is an accurate and precise synthesizer that has been used previously for NMR experiments. Fig. 4.11 shows the output of the unit set at 63.9 MHz.

During data acquisition, the local oscillator is synchronized using a standard 10 MHz reference signal from the clinical system.

4.5 Phase Drift

When using two separate frequency sources, in this case, one for RF transmit in the clinical system and the PTS 500 for the CRISP receiver chain, their frequencies and phases must be locked in order to properly receive the MR signal. Phase locking is critical for 2-D imaging. In the absence of phase lock, the phase between each row in k-space will be different. S. Obruchkov plots the difference between properly acquired signal and signal acquired using the CRISP receiver chain in Fig. 4.12. Looking at the phase data (the left plot in both figures), data obtained with the clinical system has a relatively consistent pattern across k-space and is in phase, while data acquired with the CRISP receiver chain seem to have random and incoherent phase. As a result, in the reconstructed image in Fig. 4.13(a), the object is smeared across the phase direction. A properly acquired image of the same object using the clinical system is shown in Fig. 4.13(b) for reference.

One method of correcting the phase drift is to implement a phase-locked loop in the demodulation circuit, as Fig. 4.14 illustrates.

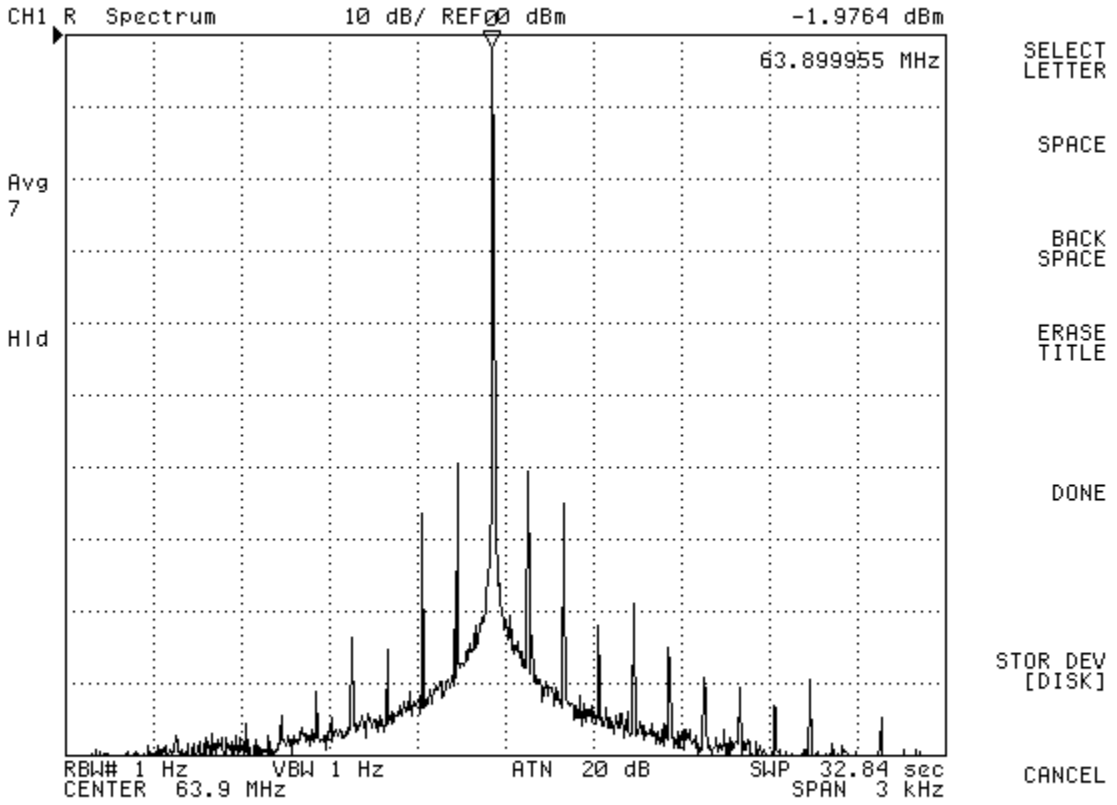

Figure 4.11: Output spectrum of PTS 500 frequency synthesizer.

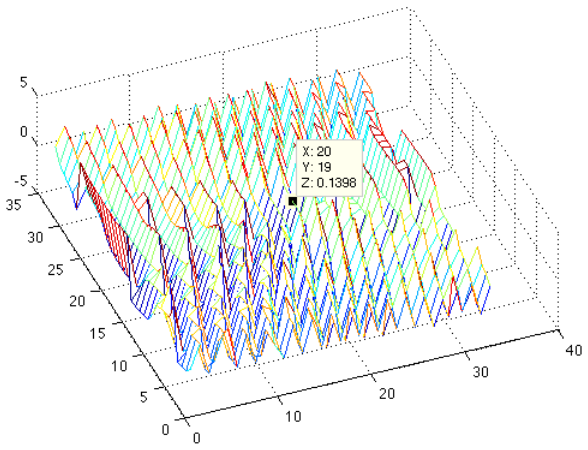

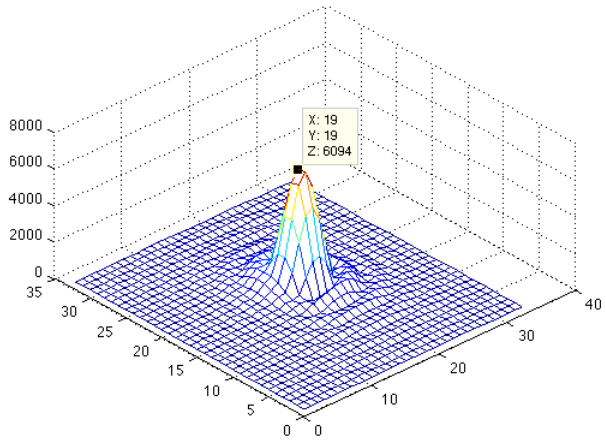

(a) K-space data from clinical system. Left: phase. Right: magnitude

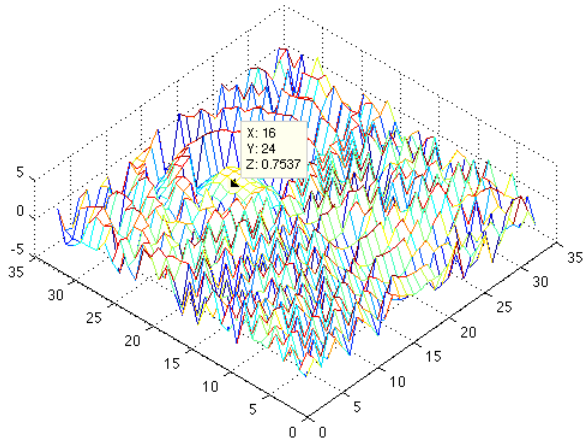

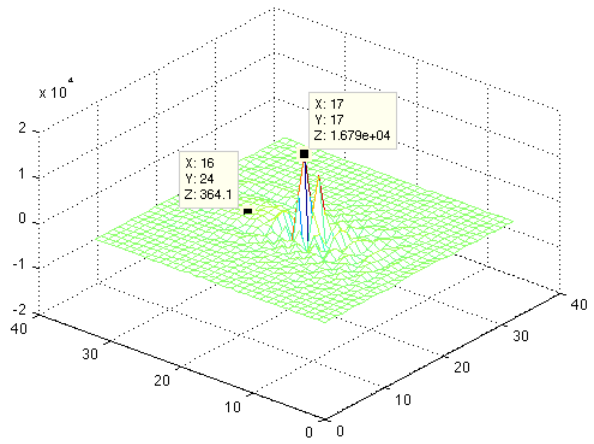

(b) K-space data from CRISP system. Left: phase. Right: magnitude

Figure 4.12: K-space data from clinical and CRISP systems. Produced by S. Obruchkov.

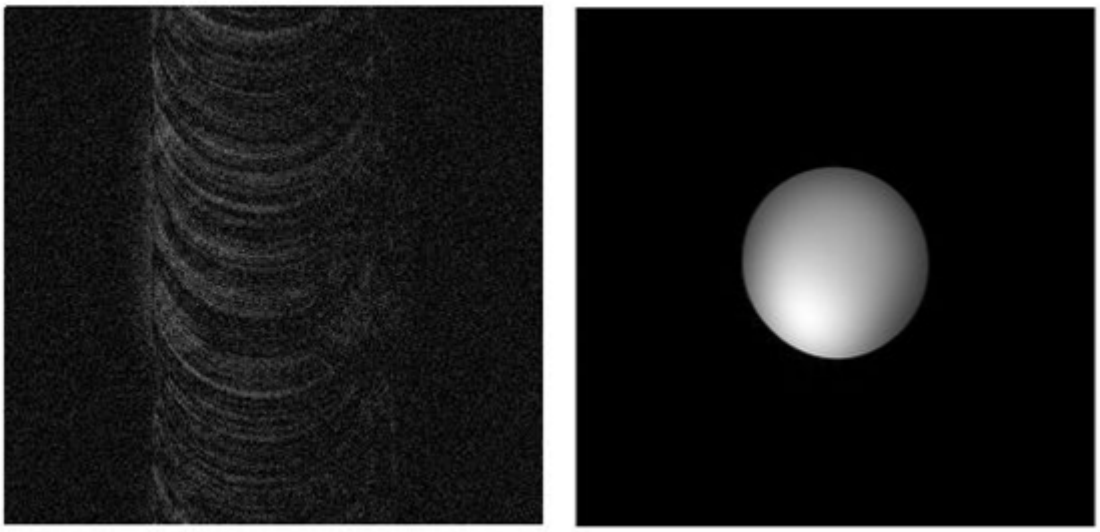

(a) Improper phase lock (b) Proper phase lock

Figure 4.13: Effects of improper phase lock between local oscillator and signal resonant frequency.

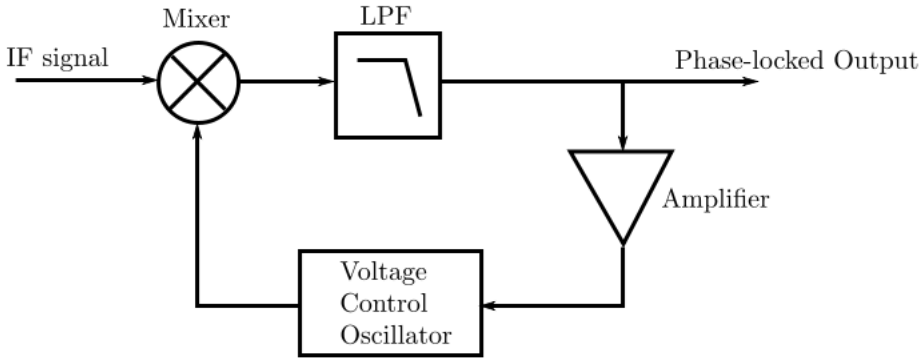

Figure 4.14: Phased-locked loop for demodulation.

4.6 Experimental Results

The custom CRISP receiver chain is interfaced with a clinical MR system, from which three signals are needed: 1) MR signal from RF coil, 2) trigger pulse to signal the beginning of data acquisition, and 3) 10 MHz reference to stabilize the local oscillator. Fig. 4.15 compares the images obtained with the clinical system versus baseband images obtained with the CRISP system (without narrowband filters). By inspection, the images from the CRISP system appear to be blurred. This is due to the issue of phase drift of the CRISP local oscillator. The effect, shown previously in Fig. 4.13(a), is much more noticeable if the signal is down-converted to a higher intermediate frequency, rather than baseband.

The signal-to-noise ratio of the images in Fig. 4.15 are shown in Table 4.2. All four images are normalized to maximum value of 1 before calculations, and SNR is defined as the RMS of signal over the RMS of noise.

Table 4.2: SNR of images acquired with clinical system and custom CRISP system

Sample	SNR with clinical system	SNR with CRISP system (without narrowband filters)
Bone	5.678 (Fig. 4.15(a))	7.896 (Fig. 4.15(b))
Onion	3.278 (Fig. 4.15(c))	5.479 (Fig. 4.15(d))

4.7 Conclusion

The major components of a RF receiver chain were discussed, including the RF receiver and the local oscillator. Specific implementation issues were highlighted such as quadrature detection, correction and phase drift. The CRISP receiver chain uses an NMR receiver and PTS500 as the local oscillator. The CRISP system and the clinical system can be operated concurrently. Images were acquired using both systems and the results were presented. Images from the CRISP system have higher SNR but are more blurry than images obtained with the clinical system.

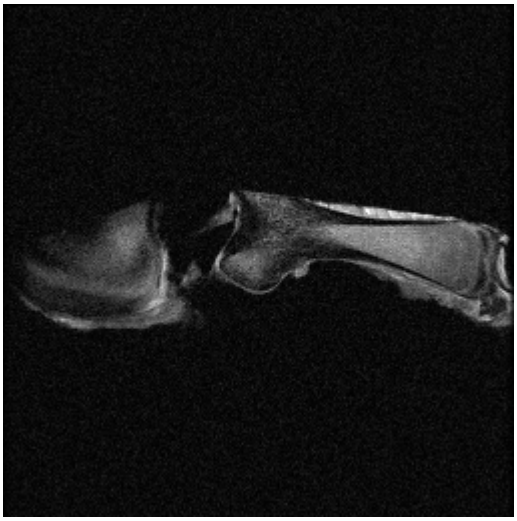

(a) Beef bone sample with clinical system

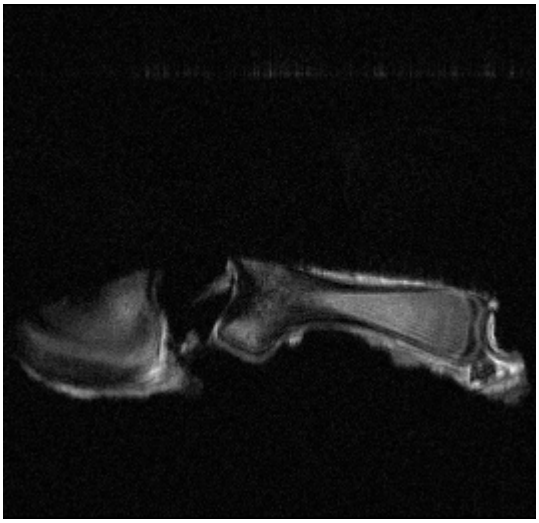

(b) Beef bone sample with CRISP system (without bandpass filters)

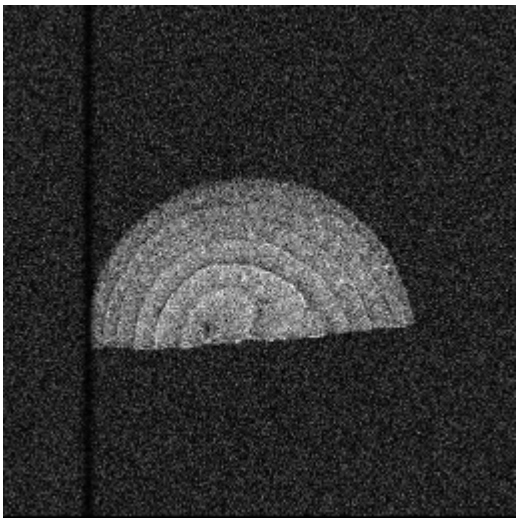

(c) Onion sample with clinical system

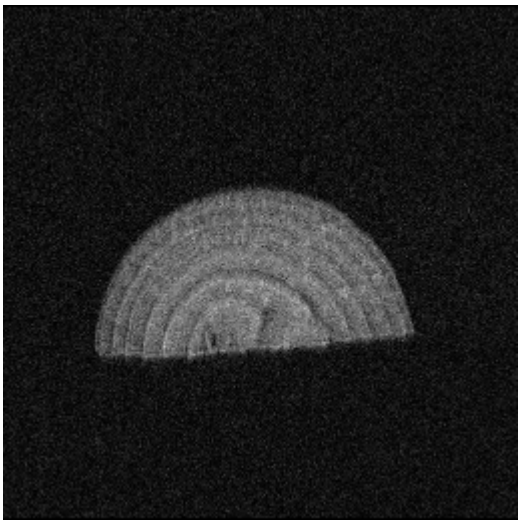

(d) Onion sample with CRISP system (without bandpass filters)

Figure 4.15: Comparison of images acquired with clinical system and custom CRISP receiver chain unfiltered (without narrowband filters). The vertical strip in (c) is an artifact from centering the sample in the image.

Chapter 5

Filter Hardware and Data Acquisition

CRISP requires a comb of analog bandpass filters, each with a narrow bandwidth, and together spanning the entire bandwidth of a broadband signal. The filters separate the broadband signal into multiple narrowband channels. This chapter will illustrate the selection, design, and implementation processes of the CRISP narrowband bandpass filters.

Before discussing filter requirements, a few parameters regarding filter specifications are defined. Fig. 5.1 shows a bandpass filter at center frequency f_0. The -3 dB frequencies are f_l and f_h. The bandwidth is defined as $f_h - f_l$. The passband includes all frequencies between f_l and f_h. R_p is the ripple magnitude in the passband, and R_s is the ripple magnitude in the stopband. The stopband includes all frequencies below f_{sl} and above f_{sh}. The minimum attenuation in the stopband is A_{min}.

5.1 Filter Requirements

Normally, the MR signal from the coil, centered at $63.864 \approx 64$ MHz for 1.5 T systems, is amplified, down-converted, demodulated, filtered and then captured with an ADC. Depending on the frequency of the local oscillator (LO) in the CRISP receiver chain, which is freely adjustable, the resulting signal from down-conversion can be centered at baseband or some intermediate frequency. The bandwidth of the signal is an adjustable imaging parameter, and is dependent on the magnetic gradient and field-of-view (FOV). Larger gradients result in larger bandwidths. The maximum gradient is limited due to dB/dt (rate of change of magnetic field) limitations imposed by health and safety regulations. Typical signal bandwidth is $31.25 \approx 32$ kHz. Depending on the amount of amplification and attenuation prior and during the demodulation stage, the power level of the signal is variable as well.

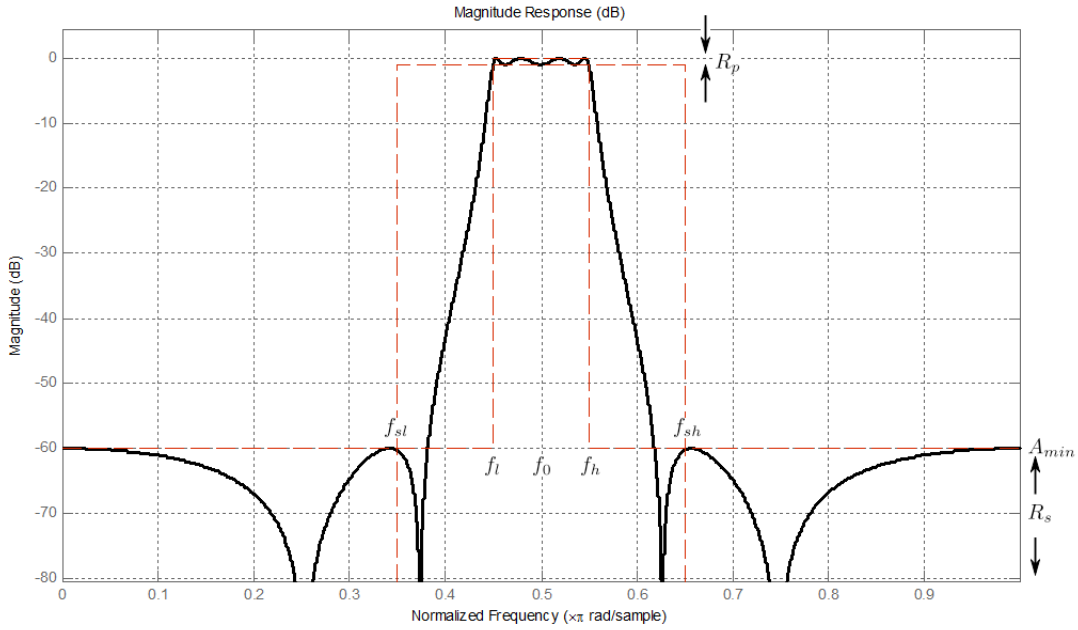

Figure 5.1: Bandpass filter response parameters.

In order to acquire full-FOV images, CRISP requires that the passband of the sum of all channels spans the 32 kHz bandwidth of the incoming MR signal. For example, if there are four channels, each would need to have 8 kHz bandwidth. Fig. 5.2 shows the frequency responses of four ideal bandpass filters each with 8 kHz bandwdith. This requirement applies regardless of the carrier frequency of the MR signal. If the bandwidths, BW, and shapes of the filters are required to be identical and only varying in center frequencies, then the bandwidth of each filter is only a function of the number of CRISP channels:

$$BW = \frac{32\ kHz}{N}, \tag{5.1}$$

where N is the number of channels. Channel bandwidth decreases as the number of channel increases. The more channels there are, the more stringent the requirements are on the filters.

Filter bandwidth is intimately related to the concept of a 'quality' factor (Q), which is a dimensionless number describing how tuned or selective a resonant circuit is. There are a few different definitions of Q depending on context. For bandpass and band reject filters, Q can be the ratio between the center frequency and the bandwidth:

$$Q = \frac{f_c}{\Delta f}. \tag{5.2}$$

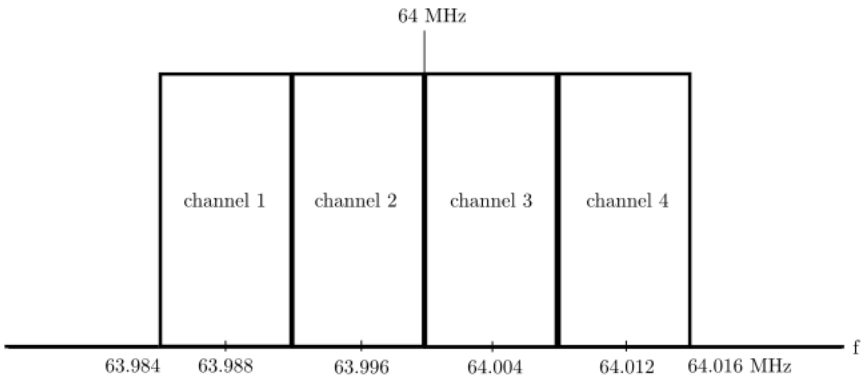

Figure 5.2: Bandpass filter responses for ideal four channel CRISP system.

At a given center frequency, the smaller the bandwidth, the higher the Q. Narrowband filters, therefore, have higher Q than relatively broadband filters. Naturally, high Q circuits demand higher quality components with tighter tolerances. In the ideal example described in Fig. 5.2, each of the four channels would have Q of $\approx$ 8,000, which is quite high. Typical Q for audio bandpass filters range from 1 to 10, and some band reject filters may approach Q of 100.

5.2 RF Filters

In an ideal scenario, the entire demodulation stage could be eliminated if filters can be designed to split the 32 kHz bandwidth signal with a 64 MHz carrier into multiple narrowband channels. In this case, RF filters are needed and there are three main types of RF filters suitable for operation at 64 MHz: 1) resistor, inductor, capacitor (RLC), 2) surface acoustic wave (SAW), and 3) crystal.

RLC filters are based on passive components, i.e. resistors, inductors and capacitors, and no active components such as operational amplifiers or transistors. Although relatively easy to design and analyze at sub-MHz frequencies, they are more complex in the RF range due to problems such as stray inductances and capacitances. Signal path length becomes an issue due to shorter wavelengths (λ is 4.68 m at 64 MHz). In general, it is difficult to achieve high Q filters with steep passband-stopband transitions with passive RLC filters.

SAW filters convert electrical signals into mechanical waves and then back into electrical signals using a piezoelectric substrate with input and output interdigital transducers (IDT), as Fig. 5.3 demonstrates. The IDTs are metal electrodes, created using lithographic techniques, similar to those used for semiconductors and integrated circuits. When a voltage is applied across the input IDT, it generates a surface wave on the piezoelectric substrate.

The pitch – spacing between the 'fingers' – of the electrodes determines the wavelength, and therefore frequency, of the wave generated. The response is strongest at the frequency that corresponds to the length of the pitch and weaker at other frequencies, hence it acts as a bandpass filter. The surface wave propagates through to the output IDT, which converts it into an output voltage.

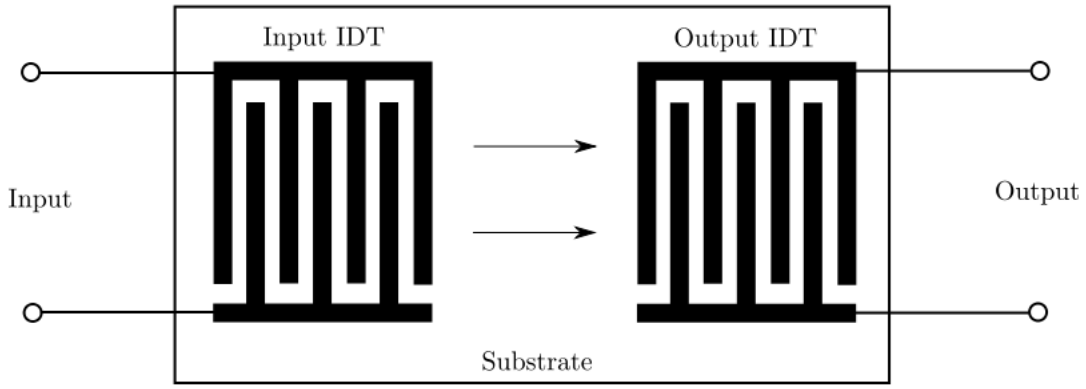

Figure 5.3: A simple SAW filter.

Commercially available SAW filters can operate anywhere from 20 MHz to 3 GHz. A transversely-coupled resonator (TCR) filter is a specific design of a SAW filter whose operation frequencies range from 50 MHz to 200 MHz. TCR filters offer bandwidths as narrow as 0.05% of center frequency, which is 32 kHz if the center frequency is 64 MHz[26].

Crystal filters use crystal resonators to achieve high-Q bandpass filters. Quartz crystals have excellent mechanical and electric properties, good temperature stability, and can have unloaded Q (i.e. not connected to any other circuit components) of up to 100,000, and are therefore a good choice for extremely narrowband bandpass filters. Crystal filters can range from 1 kHz to 150 MHz with bandwidths as low as 0.01% of center frequency, which is 6.4 kHz if center frequency is 64 MHz[27].

High-Q bandpass filters can be designed with both SAW and crystal resonators. Crystal filters edge out SAW filters when considering suitability for CRISP due to its narrower bandwidths. However, commercially available SAW and crystal resonators are usually designed for standard frequencies such as 455 kHz and 10.7 MHz for AM/FM radio, or 70 MHz for satellite communications, and so on. As a result, the cost of designing and manufacturing SAW or crystal filters with custom, non-standard, bandwidth and center frequencies is quite high in terms of both time and money. For example, specialized equipment and trained technicians/engineers are needed to grow and cut the quartz crystal to resonate at the desired custom frequencies. It was decided that implementing RF filters at 64 MHz while satisfying the bandwidth and roll-off requirements of CRISP cannot be

done with readily available components and a down-conversion of the MR signal is required such that the CRISP filters could be designed for lower frequencies.

5.3 Passive and Active Filters

Instead of designing filters to operate at 64 MHz, the filters could be placed after a demodulation stage, which could be adjusted to suit the frequency range of the filters by tuning the local oscillator. At lower frequencies, from baseband to a few MHz, filter designs can be split into two main categories: passive and active. Active filters using operation amplifiers offer several advantages over passive filters [28]:

1. No inductors needed, which tend to be lossy and pick up EM noise.
2. Sharper rolloff, frequency response and higher Q possible (compared to passive).
3. Higher and adjustable gain possible.
4. Op-amps can act as buffer to reduce loading effects.
5. Physically smaller footprint in general.
6. Ease of manufacturing and parts readily available.

Active filters have disadvantages as well:

1. Performance suffers at higher frequencies due to finite gain-bandwidth product and finite Q of op-amps.
2. Requires external power source.
3. Higher noise floor when compared to passive filters.

Regarding the first disadvantage, there are a few commercially available op-amps with GBWP in the GHz range. However, designing circuits at RF frequencies still require paying careful attention to stray capacitance and inductance both of which are safely negligable at lower frequencies. In addition, if maximum Q is limited, low center frequencies allow for narrower bandwidth filters. With that said, it is not desirable to go to the extreme and design the filters too close to baseband due to extra noise sources such as flicker ($1/f$) noise [29]. For these reasons, the filters are designed for frequencies in the 10-50 kHz range. This way, noise close to DC is avoided, and the frequencies are still low enough to allow for filters with relatively narrow bandwidths to be constructed.

Switched-capacitor filters are another type of active filter that are usually considered along with passive and active filters at these frequencies. They are available in monolithic packages and generally do not require external resistors or capacitors [28]. The cutoff frequency (3 dB point) is adjusted via an external input clock, which is used to control the rate of sampling. Because switched-capacitor filters sample the input signal, they operate in the discrete domain, in contrast to standard active and passive filters, which are both considered analog or continuous filters. Since CRISP requires filtering to be in the analog domain, switched-capacitor filters are not suitable for this application.

5.4 Filter Response Types

The next step in the filter design process is to select the desired filter response that matches most closely with the ideal. Filter response, essentially a mathematical model of the behaviour of the filter as the input signal frequency varies, is often expressed as a transfer function between input and output, $H(s) = Y(s)/X(s)$. There are five basic types of frequency responses: 1) Butterworth, 2) Chebyshev I, 3) Chebyshev II, 4) Bessel, and 5) Elliptic. The low-pass responses of each filter type are presented here.

5.4.1 Butterworth

Butterworth filters offer a maximally flat passband by placing equally spacing poles around the unit circle in the s-plane. The squared magnitude of the frequency response of an nth-order Butterworth low-pass filter [30] is:

$$|H(j\omega)|^2 = \frac{1}{1 + (\frac{\omega}{\omega_p})^{2n}},$$

where ω_p is the cutoff (-3 dB) frequency at the edge of the passband.

5.4.2 Chebyshev I

Chebyshev type I filters are known for their characteristic ripple in the passband and flat stopband. Instead of equally spacing poles in a unit circle, the poles for a Chebyshev filter are arranged on an elongated ellipse at the center of s-plane with its major axis on the imaginary axis. The squared magnitude frequency response of an nth-order Chebyshev low-pass filter [30] is:

$$|H(j\omega)|^2 = \frac{1}{1 + \epsilon^2 T_n^2(\frac{\omega}{\omega_p})},$$

where T_n is the nth-degree Chebyshev polynomnial and ϵ is determined by the allowable passband ripple in dB (R_p) [30]:

$$\begin{aligned} T_n(x) &= cosh(n \cdot arccosh(x)),\ for\ |x| \geqslant 1 \\ \epsilon &= \sqrt{10^{R_{dB}/10} - 1}. \end{aligned}$$

5.4.3 Chebyshev II

Chebyshev type II filters, sometimes referred to as the inverse Chebyshev, has flat passbands but ripples in the stopband. The squared magnitude frequency response of an nth-order inverse Chebyshev filter is [30]:

$$|H(j\omega)|^2 = \frac{1}{1 + \frac{1}{\epsilon^2 T_n^2(\frac{\omega_s}{\omega})}}.$$

Note that ω_s, the edge of the stopband, is specified rather than the edge of the passband, ω_p as in Chebyshev type I filters.

5.4.4 Bessel

Bessel filters offer maximally linear phase response, which is beneficial in applications where preservation of phase between frequencies is critical. The nth-order transfer function is based on the nth-order reverse Bessel function, $\theta_n(s)$ [30]:

$$H(s) = \frac{\theta_n(0)}{\theta_n(\frac{s}{\omega_c})},$$

and

$$\begin{aligned} \theta_n(s) &= \sum_{k=0}^{N} a_k s^k \quad where \\ a_0 &= 1 \\ a_{k+1} &= \frac{2(N-k)}{(2N-k)(k+1)} a_k, \quad for\ k = 0, 1, \ldots, N-1. \end{aligned}$$

There is no convenient closed-form expression for the squared magnitude of the frequency response of a Bessel filter [30].

5.4.5 Elliptic

The elliptic filter, also known as the Cauer filter after Wilhelm Cauer, allows for ripples in both the passband and the stopband. It has the steepest transition possible out of all previously mentioned filter responses for a given order. The squared magnitude frequency response [30] is :

$$|H(j\omega)|^2 = \frac{1}{1+\epsilon^2 R_n^2(s)},$$

where R_n is the nth-order Chebyshev rational function, which can be written as a ratio of polynomials:

$$R_n(s) = (s)^r \prod_{i=1}^{L} \left[\left(\frac{s^2 - \xi_i^2}{1 - s^2 k^2 \xi_i^2} \right) \left(\frac{1 - k^2 \xi_i^2}{1 - \xi_i^2} \right) \right],$$

where $n = 2L + r$, $r = 1$ if n odd and 0 if n even, and $k = \omega_p/\omega_s$. Finding ξ_i requires the evaluation of elliptic integrals. ξ_i is defined by the Jacobi elliptic function, $cd(z, k)$:

$$\begin{aligned} \xi_i &= cd(u_i K, k) \\ u_i &= \frac{2i-1}{N}, \quad i = 1, 2, \ldots, L, \end{aligned}$$

and K is the complete elliptic integral of the first kind :

$$K = \int_0^{\pi/2} \frac{d\theta}{\sqrt{1 - k^2 sin^2\theta}}.$$

Understanding the mathematics behind elliptic filters can be quite involved. However, the actual process of designing and implementing an elliptic filter is well-documented [30, 31, 32]. There are built-in MATLAB functions such as `ellip`, `ellipap`, and `ellipk` that significantly ease the design process for elliptic filter, and functions are available for all the aforementioned filter types as well.

Ripples in the passband are acceptable for CRISP as long as they can be characterized, and ripples in the stopband are acceptable if the minimum attenuation is high enough. Since the response of elliptic filters is the closest to the ideal, the preliminary CRISP filter design follow the elliptic filter design procedure outlined in [32] and is detailed in Appendix A.

5.5 MAX274

MAX274 is an analog active filter IC from Maxim Integrated Products. It features four independently adjustable and cascadable second-order sections capable of center frequencies up to 150 kHz. Filter parameters are adjusted using four external resistors (R_1, R_2,

R_3, R_4) per filter section. Appendix B derives the transfer function for one second-order section and the relationships between center frequency ($f_0 = \omega_0/2\pi$), Q, and gain (G_0). These equations are used to calculate the external resistor values based on the desired filter characteristics. Maxim offers a filter design software package[1] with the equations built in, which eliminates the need to calculate resistor values manually.

The MAX274 IC has limits on realizable center frequency f_0 and Q, which is due to factors such as the finite gain-bandwidth product of internal op-amps. As a result, actual performance of high-Q or high frequency designs will deviate from simulations. For the sake of getting predictable performance, designs are kept within the range of usable f_0 and Q recommended by the vendor. The maximum recommend Q for f_0 at 40 kHz is 30.

MAX274 requires additional external components in order to implement elliptic designs due to the extra zeroes in the frequency response, and the relatively low maximum Q value restricts designs to Butterworth filters only. The following table show the f_0 and Q for both cascaded second-order sections for each of eight bandpass filters:

Table 5.1: Designed f_0 and Q values for CRISP bandpass filters.

		1st Section		2nd Section	
Channel	Overall f_0	f_0	Q	f_0	Q
1	12 kHz	11.205 kHz	8.431	12.618 kHz	8.423
2	16 kHz	15.268 kHz	11.222	16.598 kHz	11.369
3	20 kHz	19.269 kHz	14.163	20.673 kHz	14.161
4	24 kHz	23.229 kHz	17.073	24.631 kHz	16.872
5	28 kHz	27.341 kHz	19.617	28.633 kHz	19.613
6	32 kHz	31.398 kHz	22.528	32.895 kHz	22.533
7	36 kHz	35.619 kHz	25.557	36.430 kHz	25.501
8	40 kHz	39.025 kHz	28.000	40.859 kHz	28.601

Each filter is a fourth-order Butterworth bandpass filter with two cascaded second-order sections. The bandwidth of each is designed to be 2 kHz.

5.6 Simulations

Using the general 2nd-order bandpass transfer function:

$$H(s) = G_0 \frac{s(\frac{\omega_0}{Q})}{s^2 + s(\frac{\omega_0}{Q}) + \omega_0^2},$$

[1] `www.maxim-ic.com/tools/other/software/274SOFT.ZIP`

and values in Table 5.1, frequency responses are simulated and plotted using IDL[2], as shown in Fig. 5.4.

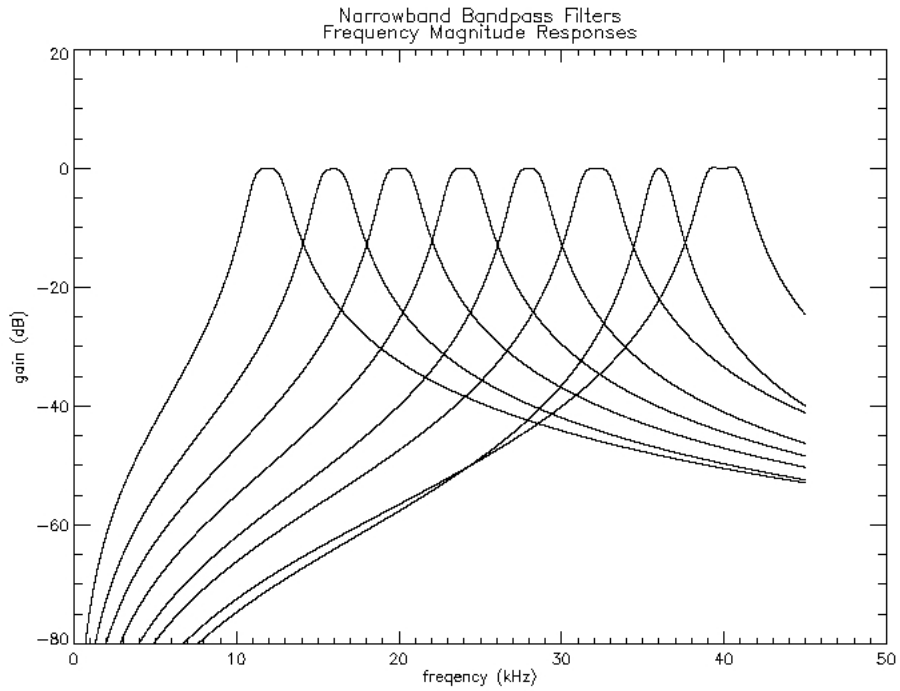

Figure 5.4: IDL simulation of CRISP bandpass filter magnitude frequency responses. Starting from left, magnitude frequency response of bandpass filter centered at 12 kHz, 16 kHz, 20 kHz, 24 kHz, 28 kHz, 32 kHz, 36 kHz, and 40 kHz.

Note that the response curve for the first six filters agree with expectations, that is, flat passbands, $\approx$ 2 kHz bandwidth, and $\approx$ 24 dB/octave roll-off rate, but the second-to-last filter (channel #7 centered at 36 kHz) has a smaller bandwidth and a sharper response than others, and the last filter (channel #8 centered at 40 kHz) has a small dip in the passband. This could be a result of the filter software design procedure, which rounds off resistor values to accommodate for practical resistor tolerances, and then recalculates the f_0 and Q values, resulting in the numbers in Table 5.1. Another possibility is that the poles of the filters have reached the maximum recommended Q limit, leading to deviation from the desired filter response.

In order to fix the imperfections, a SPICE[3] model circuit simulation is created to quickly view circuit response changes as a result of fine adjustments to component values.

[2]IDL by ITT Visual Information Solutions is a software package very similar to MATLAB by MathWorks, for data analysis, visualization, and simulations.

[3]SPICE (Simulation Program with Integrated Circuit Emphasis) is an electronic circuit simulation framework. LTspice IV from Linear Technology is the specific program used here.

The circuit diagram for one second-order filter section on the MAX274 IC is illustrated in Fig. B.1. All eight bandpass filters circuits are modelled, the first of which ($f_0 = 12$ kHz) is shown in Fig. 5.5.

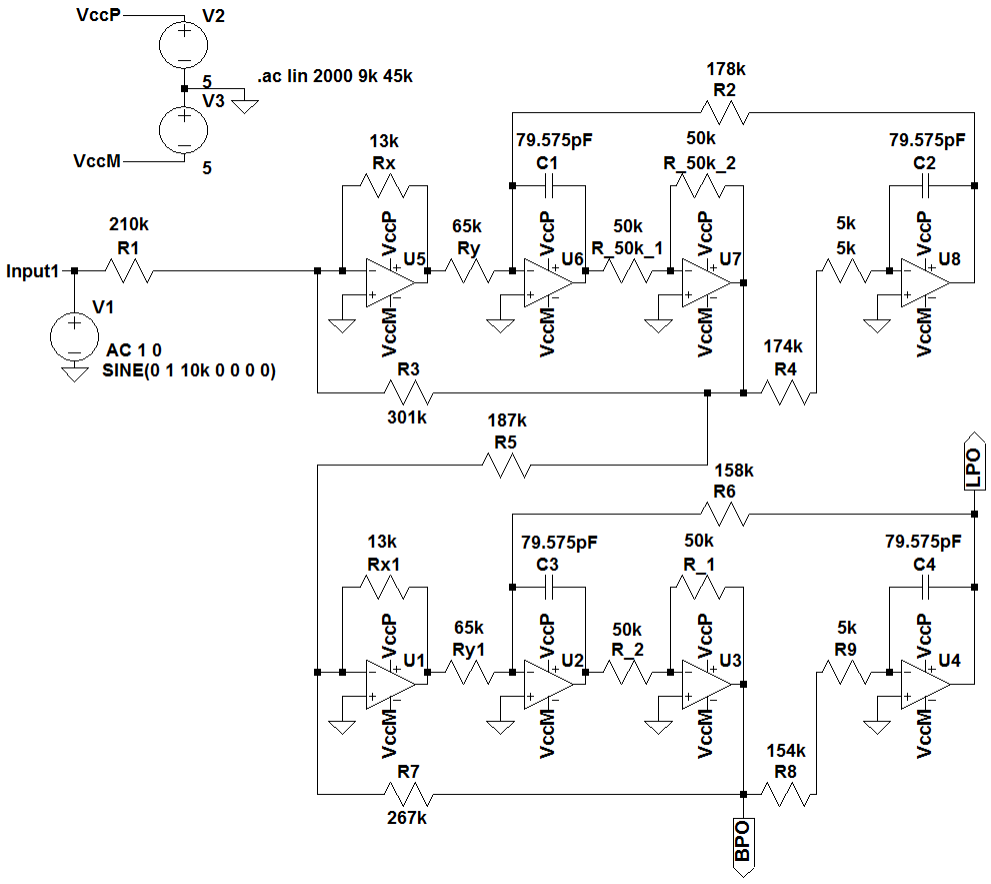

Figure 5.5: SPICE circuit simulation of 12 kHz CRISP bandpass filter.

With the aid of the SPICE simulation, resistor values are tuned to obtain much more uniform responses from all eight bandpass filters. The magnitude frequency response curves in Fig. 5.6 demonstrate the results of this adjustment. Appendix C tabulates the initial and final resistor values for the CRISP bandpass filters.

5.7 Breadboard

For the first prototype, the circuit is laid out on a breadboard. Fig. 5.7 shows the circuit schematic for one MAX274 IC, which includes two different narrowband bandpass filters. Simple buffers using TL071 op-amps in a non-inverting configuration provide isolation for

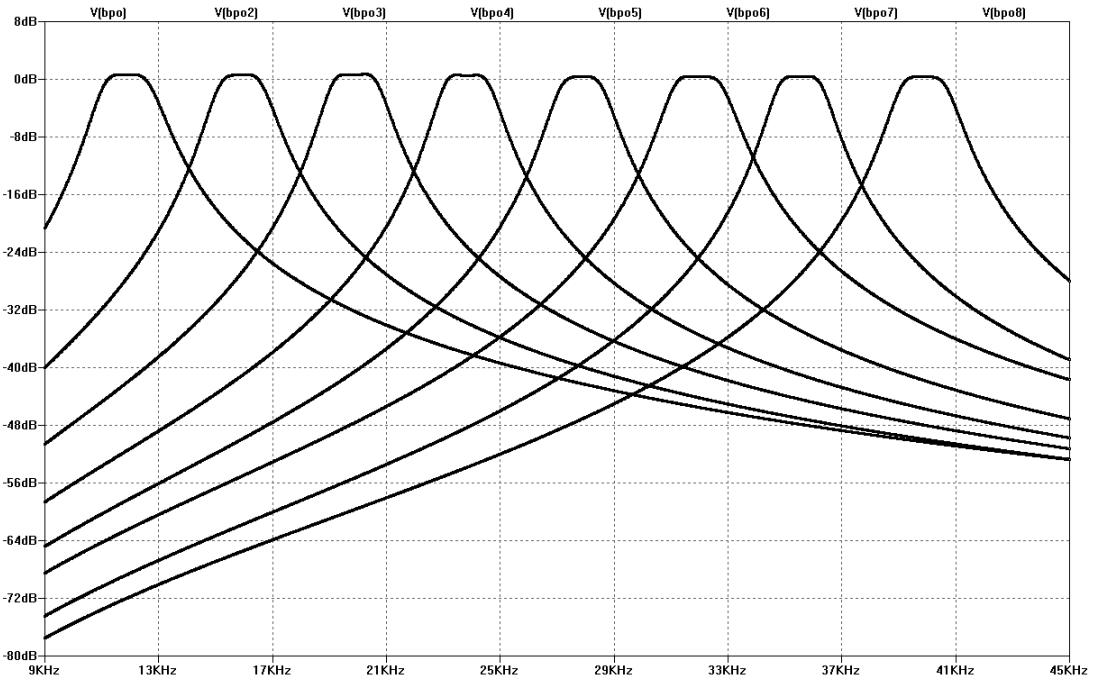

Figure 5.6: SPICE simulated frequency response for the CRISP bandpass filters after resistor tuning.

the inputs and outputs for each filter. Variable resistors are used throughout due to the non-standard resistor values in the design. The populated breadboard is shown in Fig. 5.8.

The breadboard prototype is functional, but handling and debugging the circuit with all the loose wires is a tedious task. The filters are fairly noisy, especially when placed in the RF equipment room, likely due to EM noise entering the system through the exposed wires. The next step is to move the circuit to a more permanent and less fragile platform: printed circuit board.

5.8 Printed Circuit Board

The PCB is designed to contain all eight bandpass filters, and the input and output buffers for each filter. The gain at the input and output of each filter is adjustable via variable resistors. As a compromise between cost and ease of soldering, through-hole, instead of surface-mount, components are used. Each variable resistor in the breadboard prototype translates to two standard-value resistors on the PCB. The combination of two standard resistors approximate the desired resistances and the deviation from the designed value for any pair of resistors is less than ± 0.9 %.

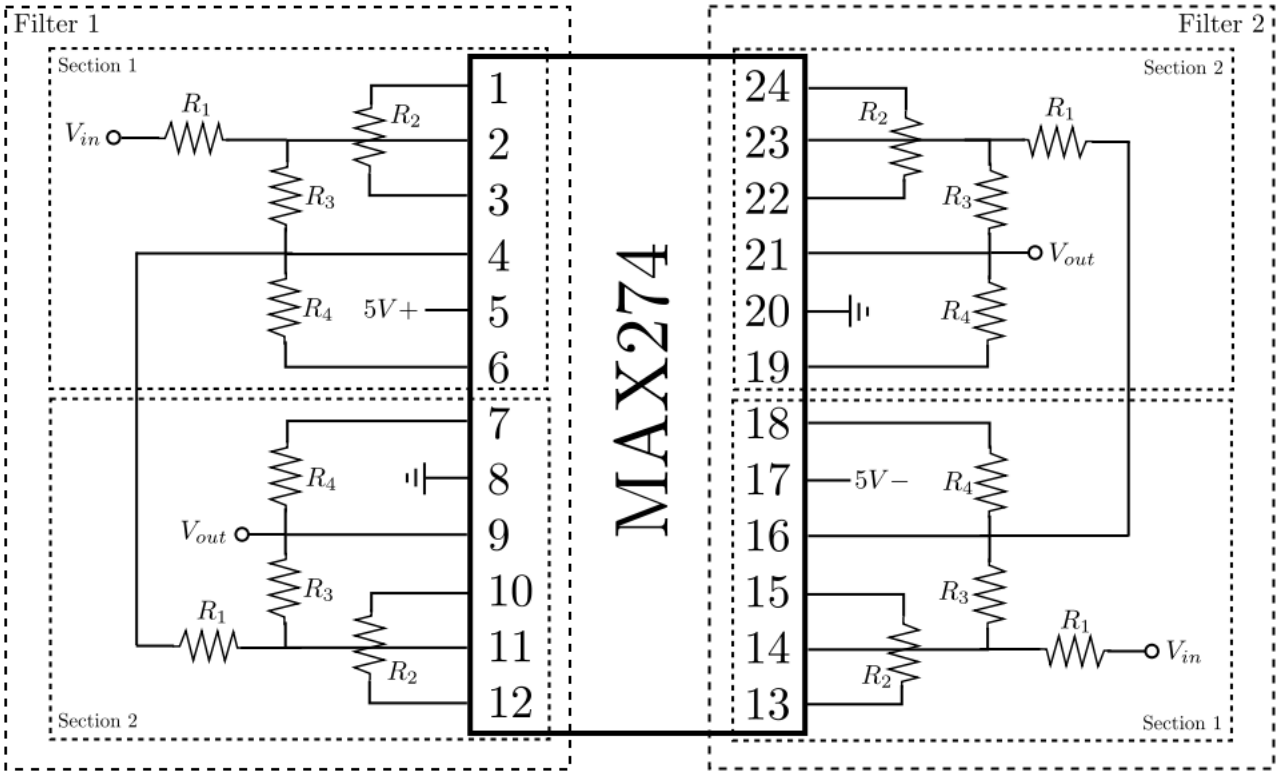

Figure 5.7: CRISP bandpass filters MAX274 breadboard layout schematic.

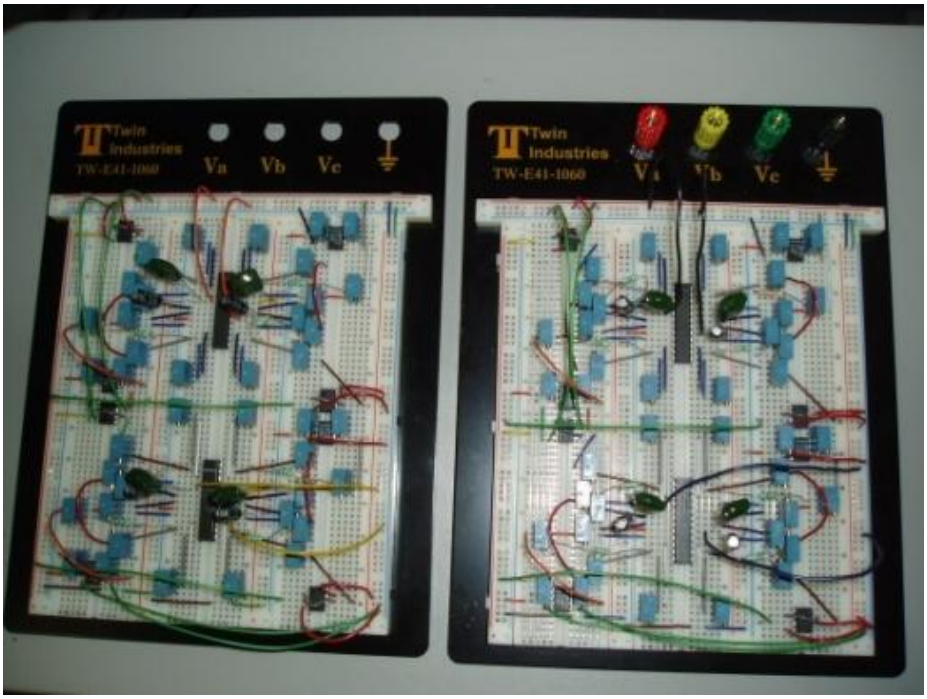

Figure 5.8: CRISP bandpass filters breadboard prototype.

In addition to the narrowband filters, an eighth-order Butterworth broadband filter with passband from 8 kHz to 30 kHz is also implemented using the same PCB design with minor adjustments. Since an eighth-order filter requires four second-order sections, the entire MAX274 IC is utilized. Recall the schematic in Fig. 5.7. The output of filter 1 can be routed to the input of filter 2, and by cascading four second-order sections, an eighth-order filter is realized without significant modifications to the PCB design.

Fig. 5.9 and 5.10 show the top and bottom layer traces respectively. The top layer is reserved for power and ground, and the bottom layer for signals. Fig. 5.11 shows the PCBs populated with all resistors and buffers in place, but is missing three MAX274 ICs[4] and the ribbon cable and power connectors.

5.9 Testing

Frequency sweeps are performed on all filters and the responses of narrowband filters 1 to 4, narrowband filters 5 to 8, and the broadband filter are shown in Fig. 5.12, 5.13 and 5.14 respectively. For the narrowband filters, the actual center frequencies correspond well with the designed values, as seen in Table 5.2, with maximum center frequency error of 1.28%. The passband bandwidths turned out to be 2.0 ± 0.1 kHz for all but the last filter, which has a 2.4 kHz bandwidth. The ripple in the passband of this filter is visible in Fig. 5.13, which is a result of inaccurate resistor values, leading to 1) uneven gain between the two poles, 2) error in the location of the poles, and 3) error in the Q of the poles.

Table 5.2: Error between actual and designed center frequencies for CRISP narrowband bandpass filters.

Designed f_0	Actual f_0	Percent Error
12 kHz	11.89 kHz	0.92%
16 kHz	15.89 kHz	0.69%
20 kHz	19.9 kHz	0.50%
24 kHz	23.84 kHz	0.67%
28 kHz	27.85 kHz	0.54%
32 kHz	31.96 kHz	0.13%
36 kHz	35.54 kHz	1.28%
40 kHz	39.68 kHz	0.80%

Noise measurements were taken to see if the filters introduce additional noise. The filters are connected to the ADC, without any input signals. The first set of measurements

[4]The two circuits on the top PCB are identical, only one of them is used

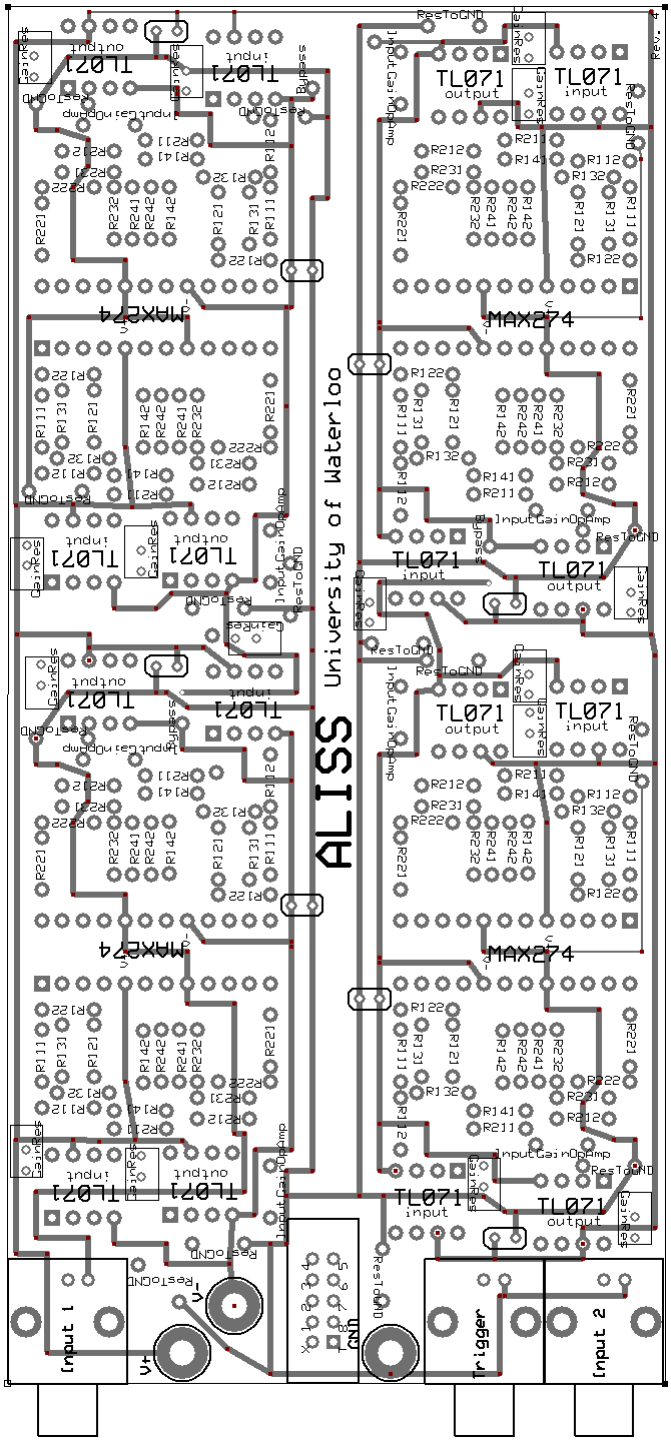

Figure 5.9: CRISP filters PCB top layer

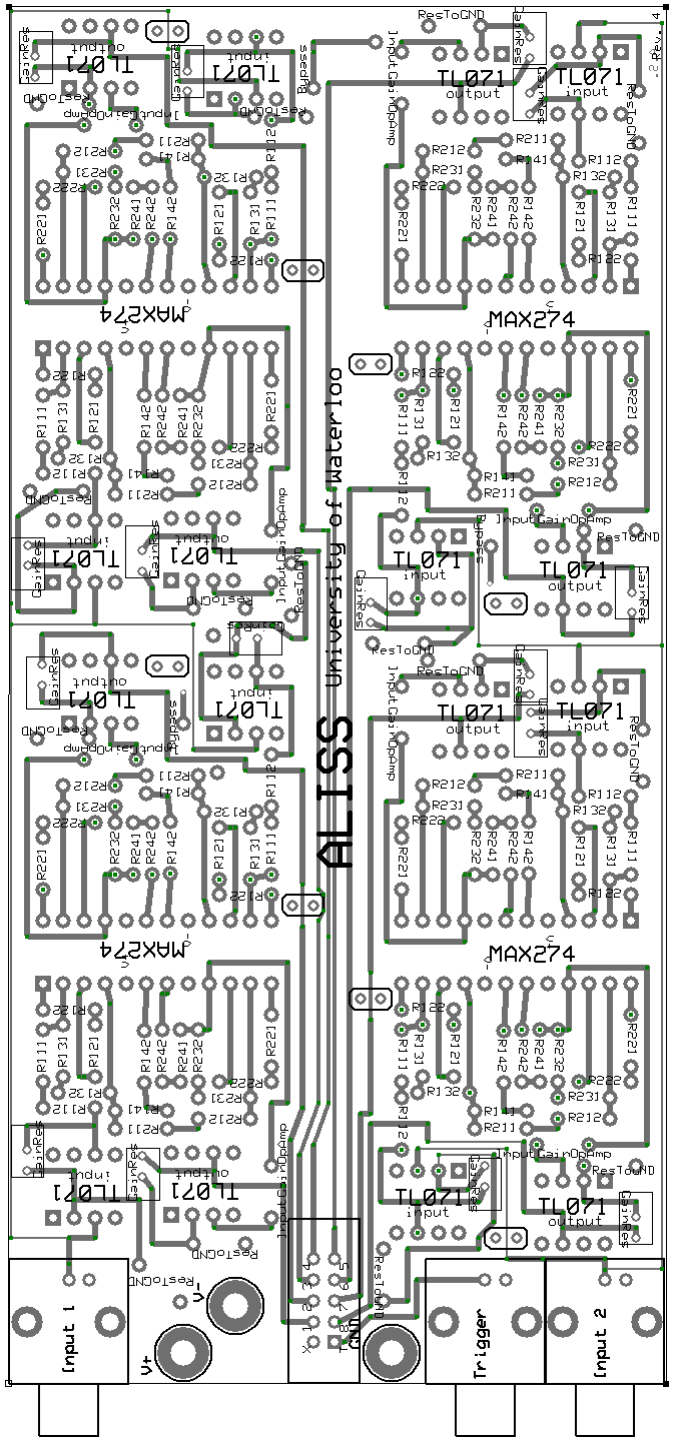

Figure 5.10: CRISP filters PCB bottom layer

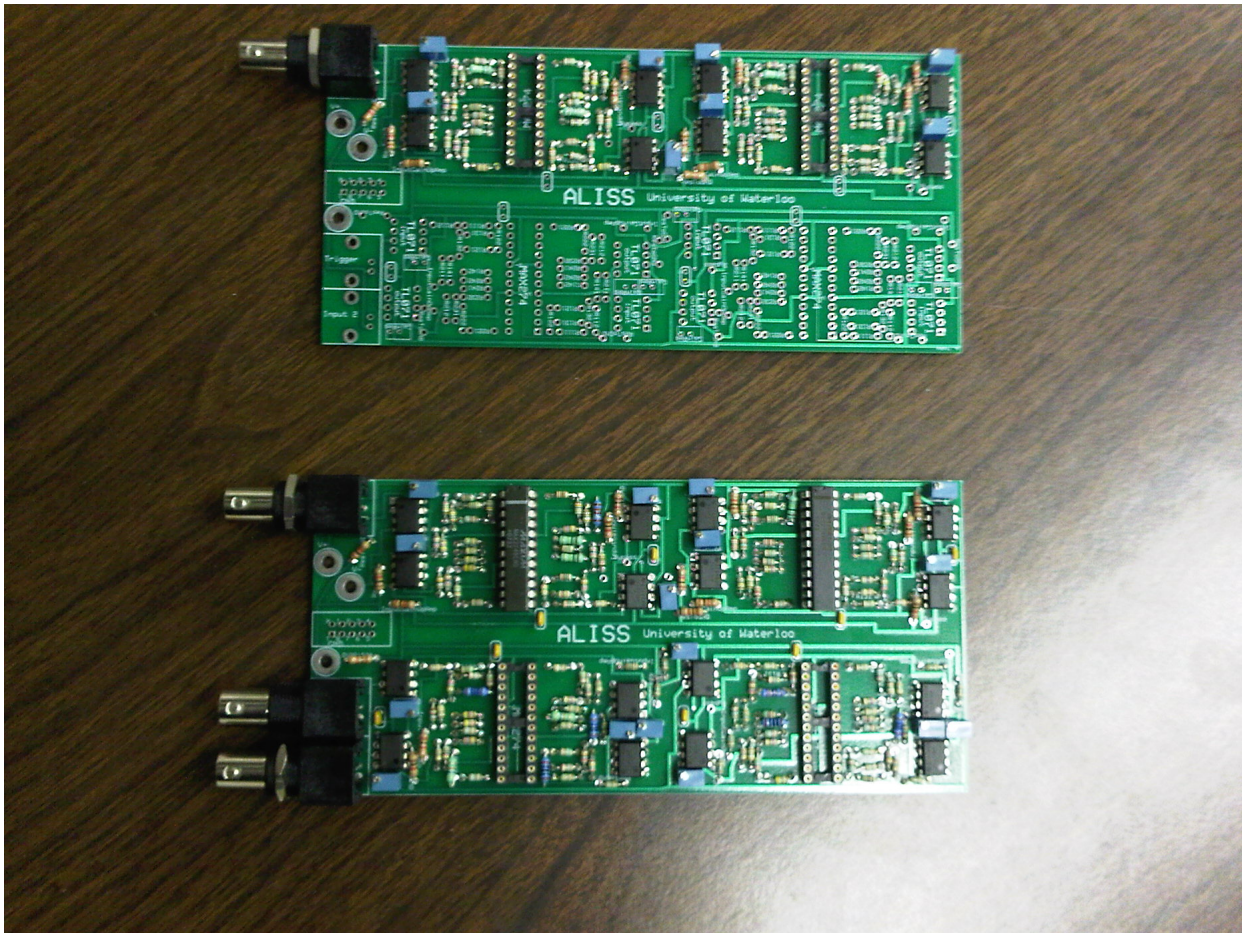

Figure 5.11: Narrowband bandpass filters (bottom) and broadband filter (top) partially populated. Missing three MAX274 ICs, ribbon and power connectors.

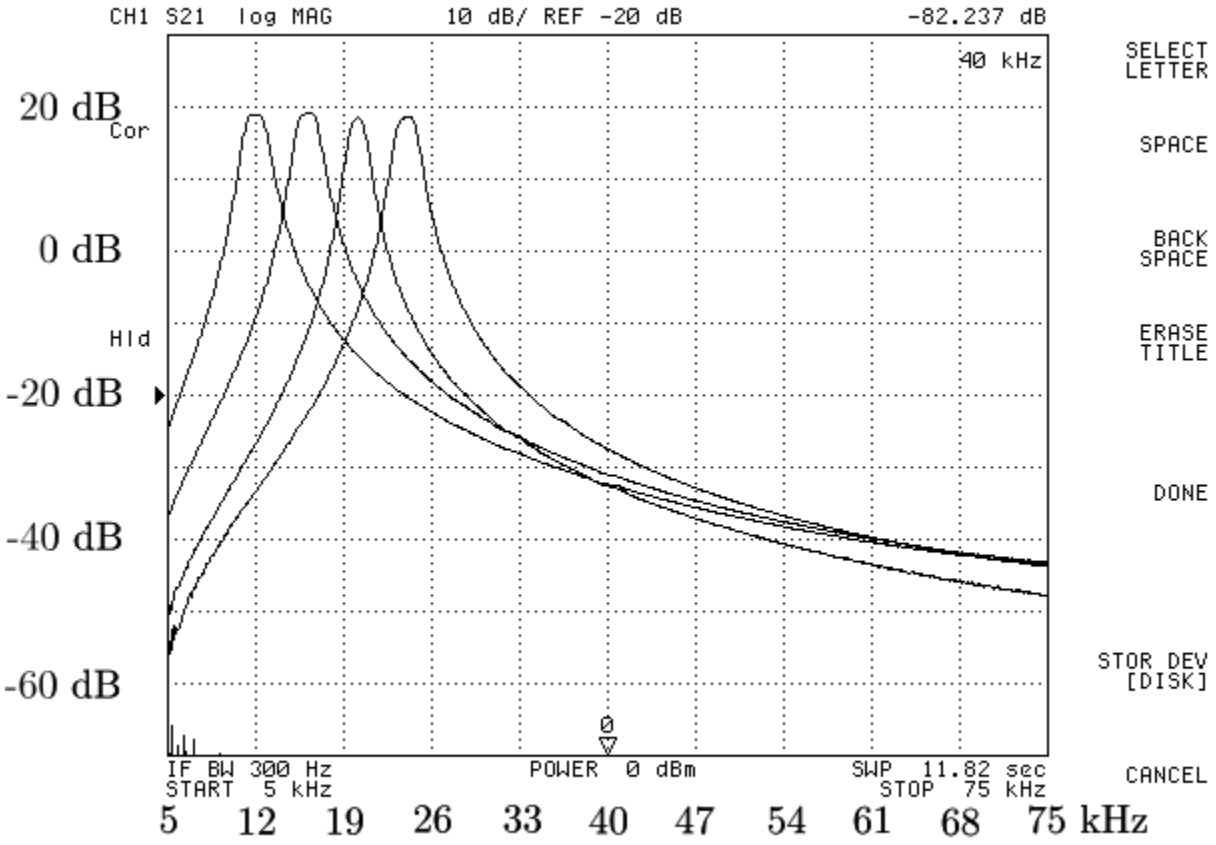

Figure 5.12: Frequency sweep of CRISP PCB narrowband filters 1-4 with spectrum analyzer.

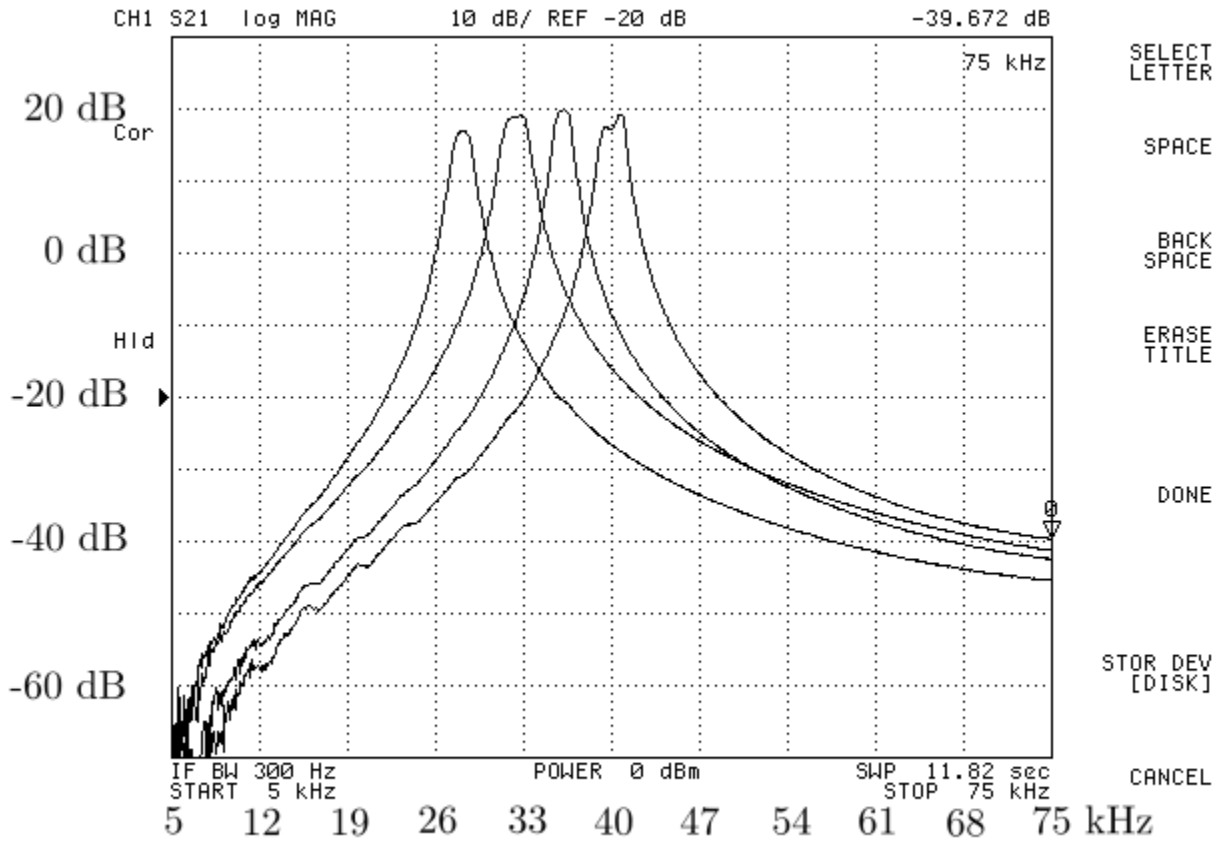

Figure 5.13: Frequency sweep of CRISP PCB narrowband filters 5-8 with spectrum analyzer.

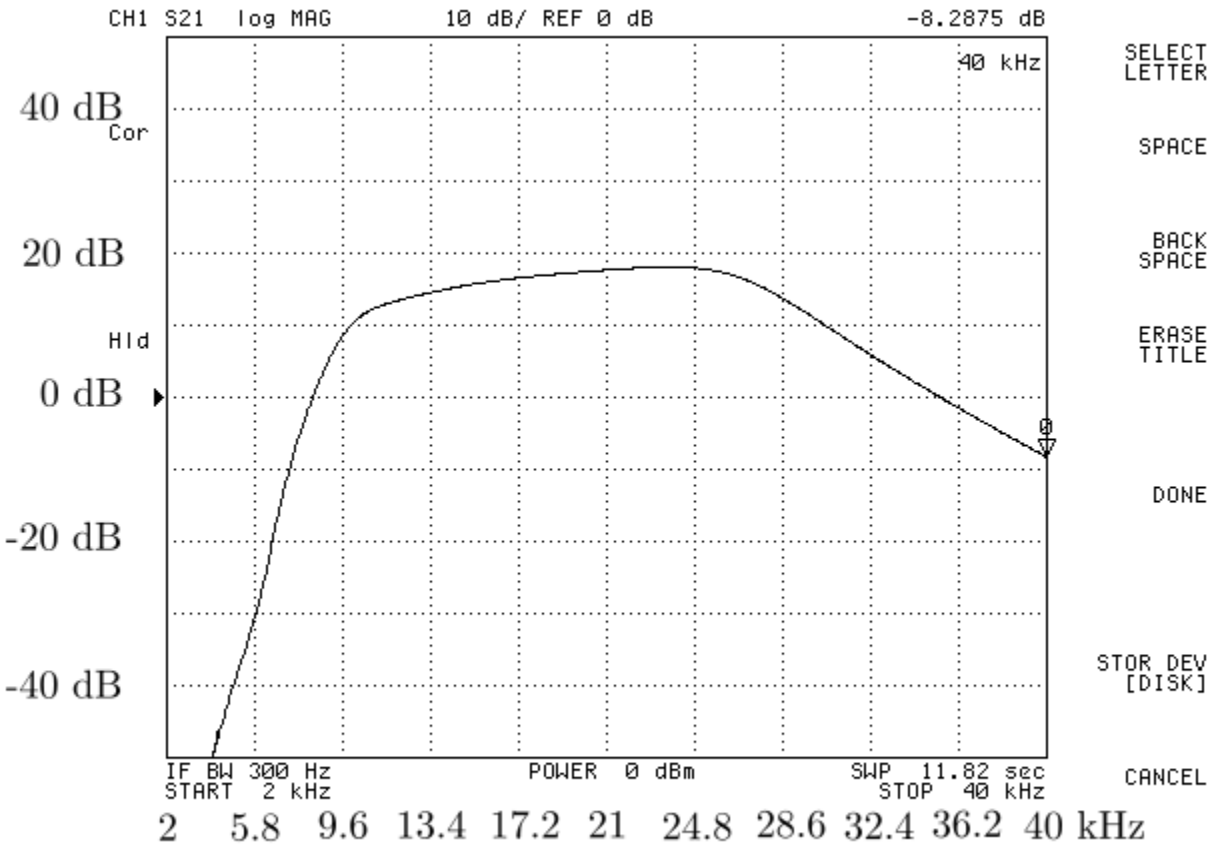

Figure 5.14: Frequency sweep of CRISP PCB broadband filter with spectrum analyzer.

are taken (500 kHz sampling rate, ±2.5V input range) without powering on the filters, and then a second set taken after turning on the filters (but still without any input signals). The average RMS noise for all channels is 3.3 mV with the filters off, and 3.0 mV with the filters on. Converting the noise into its power spectrum, it is found that the average noise floor for all channels is -43 dBm with the filters off and -45 dBm with the filters on. Therefore, the filters are not introducing any additional noise that would significantly affect the ADC's ability to distinguish between signal and noise.

5.10 Analog-to-Digital Conversion

National Instruments (NI) PCI-6123 is used as the analog-to-digital converter. It offers eight simultaneous analog input channels, each with maximum sampling rate of 500 kHz at 16-bit resolution. Input voltage can be set to one of four ranges ±10, ±5, ±2.5, or ±1.25 V. A simple C++ program using NI APIs is written to record data. A program waits for a trigger pulse from the MR system to signal the beginning of data acquisition.

The most convenient trigger pulses to access are the "Scope Trigger" and the "Receiver Unblank", both of which are available using BNC connectors. Using either of these signals for triggering leads to the acquisition of more data than necessary. That is, the pulses occur well before the beginning of the MR echoes, meaning some post-processing is required to determine the proper beginning and end of every echo. Another available signal, the signal of choice, is the "In View" pulse, which goes high when the clinical system begins data acquisition and is more accurate, but requires a non-standard connector/adaptor.

5.11 Conclusion

Design and performance requirements for the CRISP narrowband bandpass filters were presented. Various RF, low frequency, active and passive bandpass filter technologies were discussed and arguments based on the feasibility of implementation were given. The MAX274 active filter IC was chosen for the bandpass filters and a breadboard prototype was implemented. Noise and durability were two key issues with the breadboard prototype. A PCB version of the bandpass filter was realized and tested. The results indicate that the filters function as expected. NI PCI-6123 was used as the analog-to-digital converter and the "In View" signal was used to trigger the start of data acquisition.

Chapter 6

Results and Discussion

6.1 Summary of Results

In chapter 3, sensitivity improvement with CRISP is demonstrated using an 8-channel narrowband filterbank and a Bruker 11.7 T NMR magnet. The results of the experiments and simulations show that CRISP offers a sensitivity improvement for rapidly decaying signals such as those obtained from samples with short T_2-relaxation times. CRISP separates the broadband MR signal into multiple narrowband signals, and in doing so, decreases the rate of decay of the signals in each narrowband channel, enabling the signals to remain above the noise floor for a longer period of time. In the low bit-rate digitization simulations, an improvement in image resolution is achieved due to CRISP.

In chapter 4, implementation of the custom CRISP RF receiver chain is detailed and images acquired with the system are presented. The receiver chain is able to acquire images with higher SNR compared to the clinical system. However, upon visual inspection, the quality of the images is inferior due to blurring in the phase direction. This blurring is caused by the phase drift between the local oscillator in the CRISP receiver chain and the local oscillator used to generate the MR signal in the clinical system.

Chapter 5 describes the design, implementation, and testing of the CRISP narrowband bandpass filters. The CRISP filterbank requires the input MR signal to be centered in the middle of the combined passband of the narrowband filters in order to recover the full FOV of the image. The passbands of the filters span from 11 kHz to 41 kHz, which indicates that the signal should be centered at 26 kHz. However, due to the phase drift of the local oscillator in the CRISP receiver chain, acquiring a 2D non-baseband image results in the blurring effect, seen previously in chatper 4, in the reconstructed image. Centering the 32 kHz bandwidth MR image at baseband, the signal will only be seen in the first two of eight channels of the CRISP filterbank. Therefore, only a fraction of the total FOV appears in the reconstructed CRISP image.

Note that this phase drift issue affects only 2D imaging since only the phase between rows of k-space is affected. 1D acquisition is still feasible. With that in mind, the data from the bone sample presented in chapter 4 is analyzed in one dimension. Fig. 6.1 is obtained by plotting the rows of k-space on top of each other for the unfiltered image and for one channel (ch. 3) of the CRISP filterbank. Noise statistics for the unfiltered broadband echoes and the narrowband filtered echoes are calculated. Relative to the unfiltered broadband signal, it is expected that some narrowband channels would have less noise, but that the average noise from all narrowband channels should not deviate significantly from the broadband noise. Table 6.1 shows the RMS noise calculated from the first 100 samples of the broadband unfiltered signal, one channel of the narrowband filtered signal, and the average over all eight narrowband filtered signals.

Table 6.1: RMS noise of echoes from bone sample.

Signal	RMS noise
Broadband unfiltered	20.5 mV
Narrowband filtered (channel 3)	7.2 mV
Narrowband filtered (averaged over all 8 channels)	22.4 mV

In another experiment, water samples are doped with varying concentrations of magnesium chloride ($MnCl_2$) solution to simulate signal from short T_2 material. A broadband filter constructed using the same MAX274 IC as the narrowband filters, with passband spanning frequencies from 8 kHz to 30 kHz, is used as a comparison. The average RMS noise over all trials of the experiment is listed in Table 6.2.

Table 6.2: Average RMS noise over all trials in $MnCl_2$ experiment for unfiltered, broadband filtered, and narrowband filtered signals.

Signal	RMS noise
Broadband unfiltered	6.8 mV
Broadband filtered	1.3 mV
Narrowband filtered (averaged over all 8 channels)	0.8 mV

For the bone sample, the average RMS noise for narrowband filtered signals is 10% higher than the broadband unfiltered signal. In the $MnCl_2$ experiment, the average RMS noise for narrowband filtered signals is 38% lower than the broadband filtered signal. This inconsistency can simply be due to the fact that different type of samples are used for the two experiments. Different SNR can result from different samples because the RF receiver coil is loaded differently. However, even if the overall noise is slightly higher, as Table 6.1

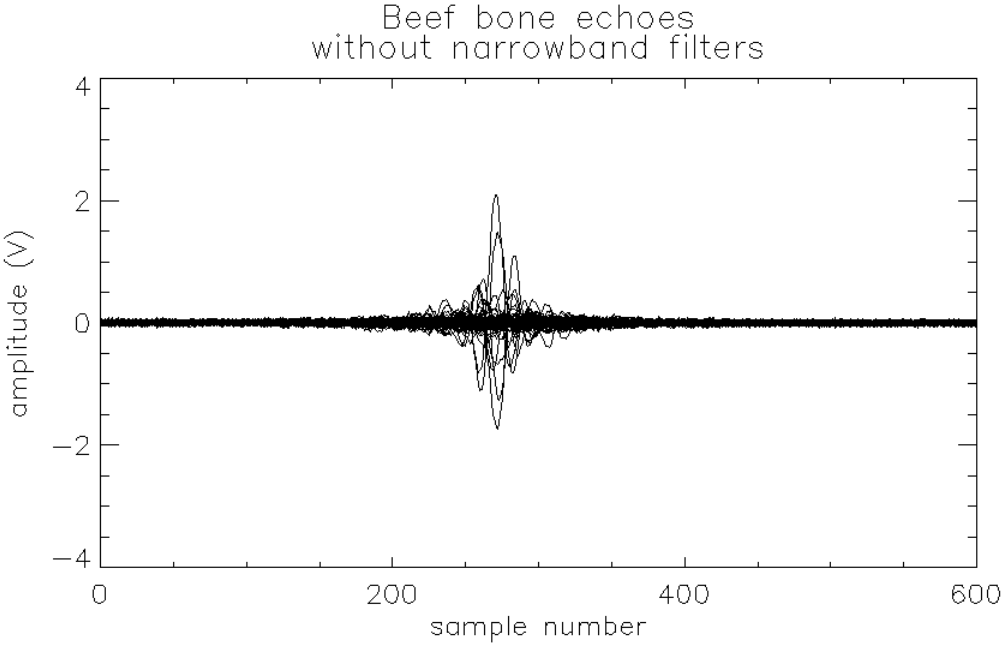

(a) Without narrowband filters

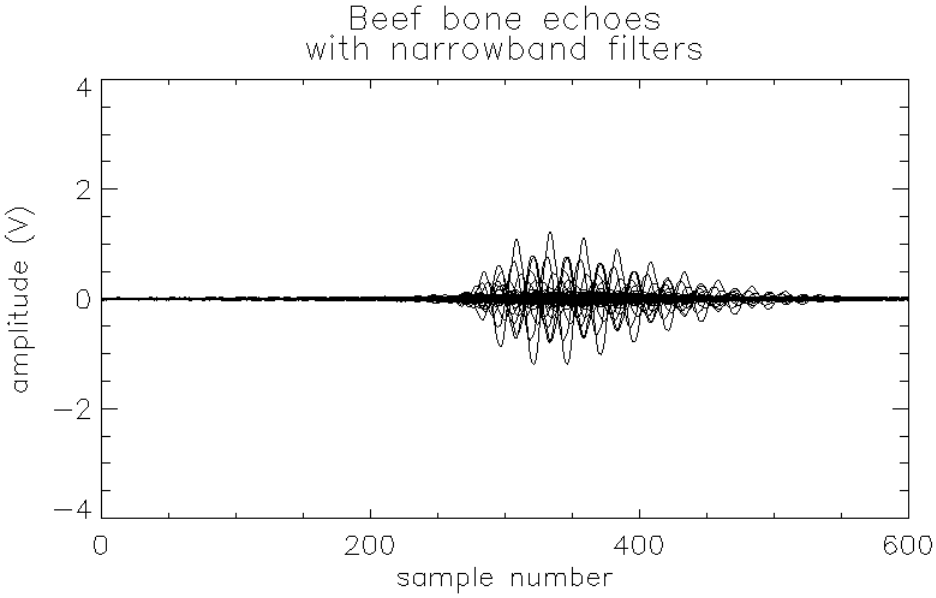

(b) With narrowband filters (channel 3)

Figure 6.1: Acquired echoes from beef bone with CRISP receiver chain.

demonstrates, lower noise floors are observed in some narrowband channels, which lead to an increase in SNR for the image regions that correspond to those channels.

6.2 Limitations

This current implementation of filterbank CRISP makes use of analog bandpass filters in and around the audio frequency range (20 Hz to 20 kHz). The additional equipment and circuitry required to downconvert the MR signal from 64 MHz to 26 kHz limits the potential improvement that could be achieved with CRISP. Compared to the receiver chain in the clinical system, the custom CRISP receiver chain is relatively simple and not optimized for operation at the MR frequencies. In addition, the phase drift caused by the usage of a different and separate local oscillator for the CRISP receiver chain limits 2D imaging capabilities. At this current state, the CRISP system can only capture 1D scans reliably.

In order for CRISP to demonstrate an SNR improvement, the signal ideally should be dominated by bandwidth dependent noise occurring after filtering. Noise in MRI, to a large extent, comes from thermal noise in the patient. Therefore, the current implmentation of filterbank CRISP has limited effect on SNR.

Chapter 7

Conclusion

A filterbank CRISP prototype was implemented, which included a custom receiver chain and analog bandpass filters. Results were obtained using a clinical system. Images acquired showed that it is feasible to achieve image with SNR comparable to those produced by the clinical system. However, due to issues with drifting phase from row to row in k-space, acquiring full-FOV, non-baseband 2D CRISP images were not possible. RMS noise in 1D echoes from two different experiments were compared and inconsistency in the average RMS noise was observed. Despite the higher average noise in the narrowband signals when compared to the broadband unfiltered signal, a few narrowband channels exhibited lower noise floors than that of the unfiltered signal, in addition to the slower decay rate observed across all narrowband channels.

The current implementation of filterbank CRISP has only eight narrowband channels. Since SNR improvement increases with the square root of the number channels, in theory, increasing the number of channels by four will bring about a factor of two improvement over the current system. Therefore, a factor of eight improvement could be gained with a 512-channel CRISP system, at which point the level of resolution and image quality improvement at 8-bit digitization shown in Fig. 3.7, could be seen at 16-bit. The maximum number of possible narrowband channels is limited by the number of pixels in the image in the frequency direction and by the narrowest possible bandpass filter.

Interfacing a custom analog RF receiver chain with a separate local oscillator with an existing clinical MRI system was lengthy process, much of it due to the novelty of processing the MR signal in the analog domain, while a majority of signal processing in current commercial systems is done in the digital domain. Many of the lessons learned during the design, construction, and testing of the CRISP system are not written in literature. Small details can make a difference with analog RF equipment, for example, the quality of coax cables make an observable improvement in signal and image quality (RG223 cables are superior to RG58).

7.1 Future Work

There are a few obvious extensions to the work presented. The first is to implement a phased-locked loop in the demodulator in order to correct the phase drift that is currently limiting 2D imaging capabilities. Second, RF narrowband filters such as crystal or SAW filters should be further investigated. By designing and constructing crystal filters, the MR signal can be filtered directly without the demodulation stage. By placing the filterbank further up the chain and closer to the RF receive coils, it opens up the possibility of directly digitizing the signal at 64 MHz.

The filterbank can be moved all the way up the chain and implemented as multiple receiver coils each tuned to a narrow range of frequencies. However, this may not be feasible since the coil Q required would be $\approx$ 16,000 for an eight-channel CRISP system at 1.5 T.

CRISP can also be operated concurrently with accelerated parallel MRI reconstruction algorithms such as PILS, SENSE, SMASH or GRAPPA. Each coil in the MRI array can be paired with a bank of narrowband filters at the output and the corresponding number of ADCs. A reconstruction algorithm that takes into account both coil and bandpass filter sensitivities would then be used to generate the images.

The sensitivity improvement offered by CRISP may have application in ultra-low-field (ULF) MRI where SNRs are inherently lower, allowing CRISP to make more of an impact in image quality. Very sensitive detectors such as superconducting quantum interference devices (SQUID) can generate MR images with very small magnetic fields [33]. CRISP can potentially improve image quality in SQUID-based MR imaging, which can be traded-in for imaging with even smaller magnetic field, perhaps as small as Earth's own field. If ULF MR can provide images of high quality, such as those necessary for diagnosis, the larger, more expensive superconducting magnets that cost thousands of dollars per year to maintain may no longer be necessary.

APPENDICES

Appendix A

Designing Elliptic Filters

The bandpass design procedure from [32] is used. The overall steps are:

1. Convert filter requirements to normalized lowpass specifications.
2. Select appropriate lowpass filter from normalized frequency response curves.
3. Use normalized lowpass parameters and transform into bandpass filter.

The normalized lowpass specifications are:

Passband bandwidth	$f_u - f_l = 36000 - 34000 = 2000$
Center frequency	$f_0 = \sqrt{f_l f_u} = 34985.71137$
Stopband bandwidth	$f_2 - \frac{f_0^2}{f_2} = 37000 - \frac{34985.71137^2}{37000} = 3918.919$
Bandpass steepness factor	$A_s = \frac{stopband\ \ bandwdith}{passband\ \ bandwidth} = \frac{3918.919}{2000} = 1.96$

To estimate the filter order required, several parameters need to be determined. The following is the design of a filter centered at 35 kHz. The rest of the filters can be design in exactly the same manner. Saal and Zverev have tabulated elliptic functions using

Passband ripple	$R_{dB} = 0.5\ dB$
Minimum stopband attenuation	$A_{min} = 50\ dB$
Lowest stopband frequency at which A_{min} occurs	$\Omega_s = 1.96$
Ripple factor	$\epsilon = \sqrt{10^{R_{dB}/10} - 1} = 0.3493$

filter order n, parameter θ in degrees, and reflection coefficient ρ in percent. The angle θ

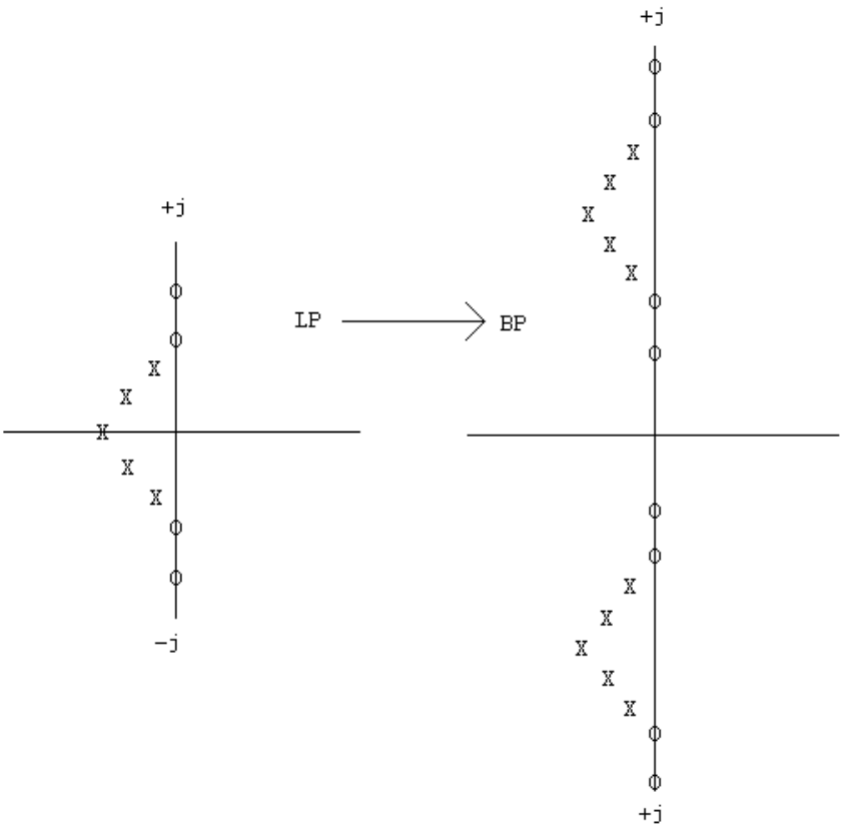

Figure A.1: Visualization of transformation of elliptic lowpass poles and zeroes to bandpass poles and zeroes

determines the steepness of the filter:

$$\theta = arcsin(\frac{1}{\Omega_s}) = 30.92^{\circ}.$$

The reflection coefficient:

$$\rho = \frac{VSWR - 1}{VSWR + 1} = \sqrt{\frac{\epsilon^2}{1 + \epsilon^2}} = 0.3298,$$

where $VSWR$ is the voltage standing wave ratio and ϵ is the ripple factor. In order to use Fig. 2-86 in [32] to estimate filter order, ρ is converted to A_p using table provided. Doing a simple linear interpolation, A_p is determined to be ≈10 dB.

$$\begin{aligned} A_{min} + A_p &= 50 + 10 = 60\ dB \\ \Omega_s &= 1.96. \end{aligned}$$

The curve indicates that a filter of $n = 5$ provides the required attenuation.

The poles and zeroes of a 5th-order elliptic lowpass filter are found from the normalized filter design table (Table 11-56 in [32]). Therefore,

θ	31.0
Ω_s	1.9416
A_{min}	59.93
σ_0	0.52122
σ_1	-0.12238
σ_3	-0.37845
Ω_1	1.0488
Ω_2	3.1460
Ω_3	0.7013
Ω_4	2.0274

Complex pole pair 1	-0.12238±1.0488j
Complex pole pair 2	-0.37845±0.7013j
Real pole	-0.52122
Imaginary zero pair 1	±3.1460j
Imaginary zero pair 2	±2.0274j

A series of design equations, obtained from Chapter 5 of [32], are used to determine the center frequency f_r, gain A, Q factor Q, and zero frequency f_∞ for each of the five

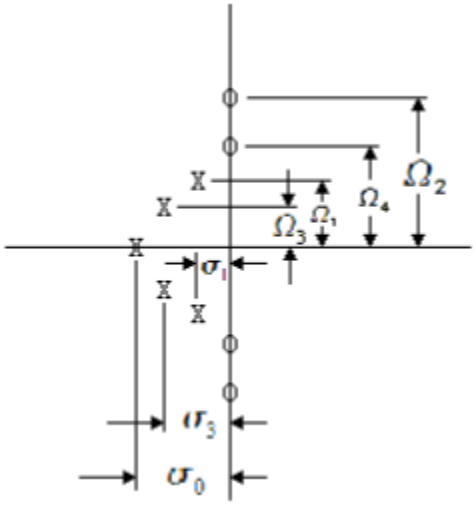

Figure A.2: Poles and zeroes of normalized 5th-order elliptic lowpass

Section	f_r	A	Q	f_∞
1	33952.622	8.632	143.003	31980.875
2	36050.235	8.632	143.003	38272.875
3	34291.399	2.106	46.232	33017.005
4	35694.081	2.106	46.232	37071.805
5	34985.711	1	33.561	n/a

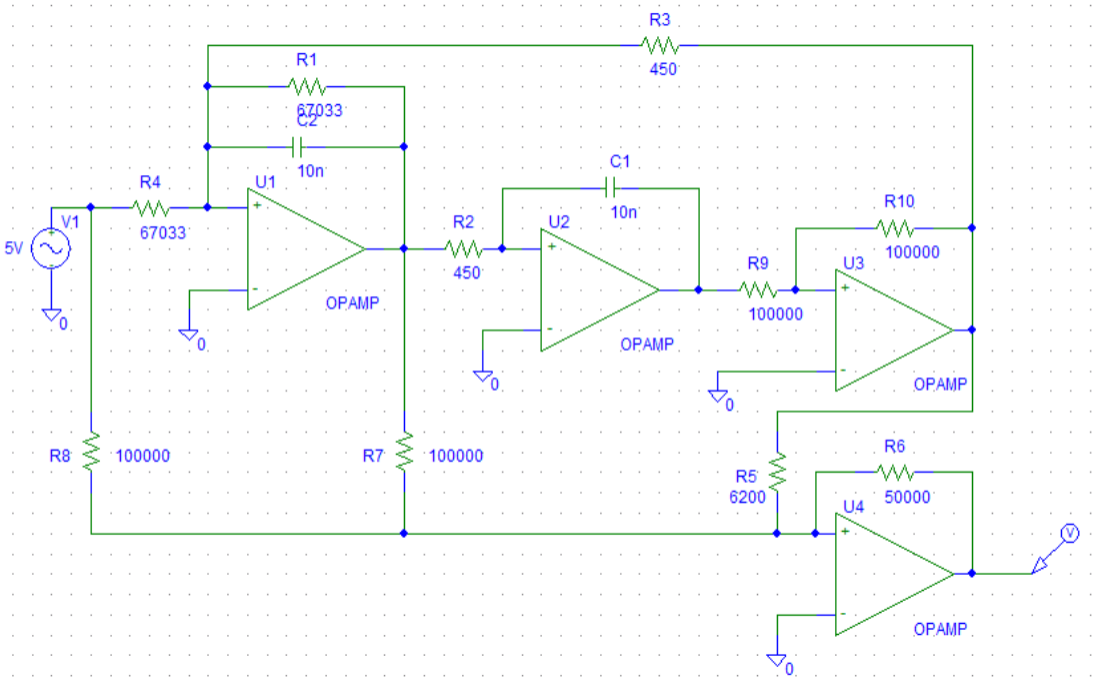

Figure A.3: State-variable biquad topology with additional zero.

filter sections: The state-variable biquad in Fig. A.3 is chosen as the filter topology to implement. The additional op-amp in the lower right corner makes it possible to realize a zero above or below the resonant frequency. When $f_\infty < f_r$, such as in sections 1 and 3, the transfer function is:

$$T(s) = \frac{-R_6}{R} \frac{s^2 + \frac{1}{R_2 R_3 C^2}(1 - \frac{R_3 R}{R_4 R_5})}{s^2 + \frac{1}{R_1 C} s + \frac{1}{R_2 R_3 C^2}}.$$

When $f_\infty > f_r$, such as in sections 2 and 4, the transfer function is:

$$T(s) = \frac{-R_6}{R} \frac{s^2 + \frac{1}{R_2 R_3 C^2}(1 + \frac{R_3 R}{R_4 R_5})}{s^2 + \frac{1}{R_1 C} s + \frac{1}{R_2 R_3 C^2}}.$$

The general bandpass transfer function is:

$$T(s) = \frac{H(s^2 - \omega_\infty^2)}{s^2 + \frac{\omega_r}{Q} s + \omega_r^2}.$$

Equating the coefficients, we can use the following equations to calculate resistor values:

$$\begin{aligned} R_1 = R_4 &= \frac{Q}{2\pi f_r C} \\ R_2 = R_3 &= \frac{R_1}{Q} \\ R_5 &= \frac{f_r^2 R}{Q|f_r^2 - f_\infty^2|} \\ R_6 &= \frac{f_r^2 R}{f_\infty^2} \quad for\ f_\infty > f_r \\ R_6 &= R \quad for\ f_\infty < f_r. \end{aligned}$$

Appendix B

Derivation of MAX274 second-order section transfer function

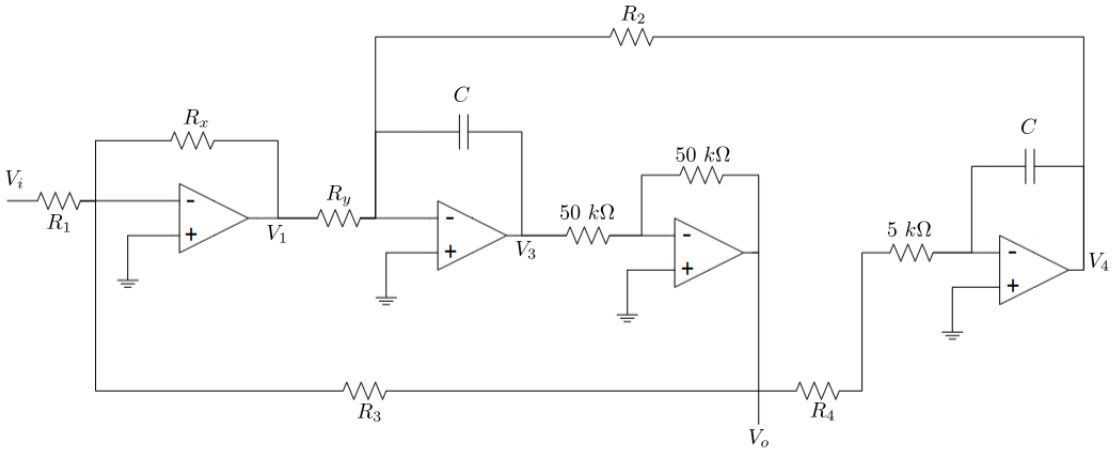

Figure B.1: Circuit diagram of one second order section in MAX274

In this section, the transfer function for the second-order filter section in MAX274 is derived. The result will reveal exactly how the filter parameters center frequency ω_0, gain G_0, and Q vary with the four external resistors, R_1, R_2, R_3, and R_4. Recall that the impedance of a capacitor is

$$Z_c = \frac{1}{j\omega C},$$

where in this case $C = 79.575$ pF. As well, for convenience and to simplify expressions, we define

$$R' = R_4 + 5k\Omega.$$

Treat the first op-amp from the left as a summing amplifier, summing V_o and V_i weighted by R_3 and R_1 respectively. At the output of the first op-amp:

$$\begin{aligned} \frac{V_1}{R_x} &= \frac{V_i}{R_1} + \frac{V_o}{R_3} \\ V_1 &= \frac{R_x}{R_1} V_i + \frac{R_x}{R_3} V_o. \end{aligned} \tag{B.1}$$

The second op-amp sums V_1 and V_4, weighted by R_y and R_2 respectively. At the output of the second op-amp:

$$-j\omega C V_3 = \frac{V_1}{R_y} + \frac{V_4}{R_2}. \tag{B.2}$$

At the output of the third op-amp, which is in a simple inverting configuration:

$$V_o = -V_3. \tag{B.3}$$

Finally, at the output of the last op-amp:

$$\begin{aligned} -j\omega C V_4 &= \frac{V_o}{R'} \\ V_4 &= \frac{V_o}{-(R+5k)j\omega C}. \end{aligned} \tag{B.4}$$

Substituting Eq. B.3 and B.4 into Eq. B.2:

$$\begin{aligned} -j\omega C V_o &= \frac{V_1}{R_y} + \frac{V_o}{-j\omega R_2 R' C} \\ \frac{V_1}{R_y} &= \left[j\omega C + \frac{1}{j\omega R_2 R' C} \right] V_o. \end{aligned} \tag{B.5}$$

Substituting Eq. B.1 into Eq. B.5:

$$\begin{aligned} -\frac{R_x}{R_y R_1} V_i - \frac{R_x}{R_y R_3} V_o &= \left[\frac{\omega^2 R' R_2 C^2 + 1}{j\omega R' R_2 C} \right] V_o \\ -\frac{R_x}{R_y R_1} V_i &= \left[\frac{\omega^2 R' R_2 C^2 + 1}{j\omega R' R_2 C} + \frac{R_x}{R_y R_3} \right] V_o \\ \frac{V_o}{V_i} &= \frac{-\frac{R_x}{R_y R_1}}{\left[\frac{\omega^2 R_y R' R_2 R_3 C^2 + R_y R_3 + j\omega R_x R' R_2 C}{j\omega R_y R' R_2 R_3 C} \right]} \\ \frac{V_o}{V_i} &= \frac{-\frac{R_x}{R_y R_1} (j\omega R_y R' R_2 R_3 C)}{\omega^2 R_y R' R_2 R_3 C^2 + R_y R_3 + j\omega R_x R' R_2 C}. \end{aligned}$$

Dividing top and bottom by $R_y R' R_2 R_3 C^2$, substituting $s = j\omega$, and simplifying:

$$H(s) = \frac{s(\frac{R_x}{R_y R_1 C})}{s^2 - s(\frac{R_x}{R_y R_3 C}) + (\frac{1}{R' R_2 C^2})}. \tag{B.6}$$

Compare Eq. B.6 with the general 2nd-order bandpass transfer function:

$$H(s) = G_0 \frac{s(\frac{\omega_0}{Q})}{s^2 + s(\frac{\omega_0}{Q}) + \omega_0^2},$$

where G_0 is the gain at the center frequency f_0. To match up the coefficients, multiply the top of Eq. B.6 by $\frac{R_3}{R_3}$:

$$H(s) = \frac{s(\frac{R_x}{R_y R_3 C})(\frac{R_3}{R_1})}{s^2 - s(\frac{R_x}{R_y R_3 C}) + (\frac{1}{R' R_2 C^2})}.$$

Equating the coefficients, we have:

$$\begin{aligned} \frac{\omega_0}{Q} &= \frac{R_x}{R_y R_3 C} \\ \omega_0^2 &= \frac{1}{R' R_2 C^2} \\ G_0 &= \frac{R_3}{R_1}. \end{aligned} \tag{B.7}$$

Solving for ω_0:

$$\begin{aligned} \omega_0 &= \frac{1}{C}\sqrt{\frac{1}{R' R_2}} \\ \omega_0 &= \frac{1}{C}\sqrt{\frac{1}{(R_4 + 5k\Omega) R_2}}. \end{aligned} \tag{B.8}$$

Solving for Q:

$$\begin{aligned} \frac{R_x}{R_y R_3 C} &= \frac{\frac{1}{C}\sqrt{\frac{1}{(R_4+5k\Omega)R_2}}}{Q} \\ Q &= \sqrt{\frac{1}{(R_4 + 5k\Omega) R_2}}(\frac{R_y}{R_x})(R_3). \end{aligned} \tag{B.9}$$

Appendix C

Initial and Final Resistor Values for CRISP Filters

The following tables detail the initial resistor values obtained with Maxim's filter design software and the final resistor values after fine tuning with the aid of a SPICE simulation.

Table C.1: CRISP bandpass filter resistor values before and after fine adjustments, for filters 1-4

Filter f_0	Section	Resistor	Initial ($k\Omega$)	Final ($k\Omega$)
12 kHz	1	R_1	196	210
		R_2	178	178
		R_3	301	301
		R_4	174	174
	2	R_1	205	187
		R_2	158	158
		R_3	267	267
		R_4	174	154
16 kHz	1	R_1	205	220
		R_2	130	130
		R_3	294	294
		R_4	127	127
	2	R_1	210	200
		R_2	121	121
		R_3	274	274
		R_4	115	115
20 kHz	1	R_1	200	220
		R_2	105	105
		R_3	294	294
		R_4	97.6	97.6
	2	R_1	200	200
		R_2	97.6	97.6
		R_3	274	274
		R_4	90.9	90.9
24 kHz	1	R_1	196	220
		R_2	86.6	86.6
		R_3	294	280
		R_4	80.6	80.6
	2	R_1	205	210
		R_2	80.6	80.6
		R_3	274	260
		R_4	76.8	76.8

Table C.2: CRISP bandpass filter resistor values before and after fine adjustments, for filters 5-8

Filter f_0	Section	Resistor	Initial ($k\Omega$)	Final ($k\Omega$)
28 kHz	1	R_1	210	220
		R_2	73.2	73.2
		R_3	287	240
		R_4	68.1	68.1
	2	R_1	205	210
		R_2	69.8	69.8
		R_3	274	230
		R_4	64.9	64.9
32 kHz	1	R_1	215	196
		R_2	63.4	63.4
		R_3	287	220
		R_4	59	59
	2	R_1	174	196
		R_2	60.4	60.4
		R_3	274	205
		R_4	56.2	56.2
36 kHz	1	R_1	255	230
		R_2	56.2	57
		R_3	287	220
		R_4	51.1	52
	2	R_1	237	210
		R_2	54.9	54.9
		R_3	280	210
		R_4	49.9	49.9
40 kHz	1	R_1	169	210
		R_2	51.1	50
		R_3	287	190
		R_4	46.4	46.4
	2	R_1	178	200
		R_2	48.7	48.7
		R_3	280	180
		R_4	44.2	44.2

Bibliography

[1] A. R. Hajian and J. K. Kim, "Noise reduction by means of spectral parallelism," May 2009. US Patent No. US 2009/0136104 A1. 1

[2] A. R. Hajian, B. B. Behr, A. T. Cenko, R. P. Olling, D. Mozurkewich, J. T. Armstrong, B. Pohl, S. Petrossian, K. H. Knuth, R. B. Hindsley, M. Murison, M. Efroimsky, R. Dantowitz, M. Kozubal, D. G. Currie, T. E. Nordgren, C. Tycner, and R. S. McMillan, "Initial results from the USNO dispersed fourier transform spectrograph," *The Astrophysical Journal*, Jan 2007. 1

[3] E. W. Weisstein, *Millimeter/Submillimeter Fourier Transform Spectroscopy of Jovian Planet Atmospheres*. PhD thesis, California Institute of Technology, 1996. 2

[4] F. Bloch, "nuclear induction," *Physical Review*, vol. 70, pp. 460–474, 1946. 5, 12, 13

[5] E. M. Purcell, H. C. Torrey, and R. V. Pound, "Resonance absorption by nuclear magnetic moments in a solid," *Physical Review*, vol. 69, pp. 37–38, 1946. 5

[6] M. H. Levitt, *Spin Dynamics: Basics of Nuclear Magnetic Resonance*. West Sussex, England: John Wiley & Sons Ltd, second ed., 2008. 5, 6, 7, 8, 37

[7] Z.-P. Liang and P. C. Lauterbur, *Principles of Magnetic Resonance Imaging: A Signal Processing Perspective*. Piscataway, USA: IEEE Press, 2000. 6, 7, 8, 10, 11, 12, 13, 37

[8] C. P. Slichter, *Principles of Magnetic Resonance*. Springer-Verlag, third ed., 1990. 6, 7

[9] R. H. Hashemi, W. G. B. Jr., and C. J. Lisanti, *MRI: The Basics*. Philadelphia, USA: Lippincott Williams & Wilkins, second ed., 2004. 8, 11, 12, 14

[10] J. P. Hornak, *The Basics of MRI*. 2010. `http://www.cis.rit.edu/htbooks/mri/index.html`. 12

[11] S. Sykora, "Suppression of receiver recovery time in NMR," in *Stan's Library*, vol. II. `http://dx.doi.org/10.3247/SL1Nmr07.001`. 14

[12] P. B. Roemer, W. A. Edelstein, C. E. Hayes, S. P. Souza, and O. M. Mueller, "The NMR phased array," *Magnetic Resonance in Medicine*, vol. 16, pp. 192–225, 1990. 20

[13] D. J. Larkman and R. G. Nunes, "Parallel magnetic resonance imaging," *Physics in Medicine and Biology*, vol. 52, pp. 15–55, 2007. 20

[14] M. Blaimer, F. Breuer, M. Mueller, R. M. Heidemann, M. A. Griswold, and P. M. Jakob, "SMASH, SENSE, PILS, GRAPPA: How to choose the optimal method," *Topics in Magnetic Resonance Imaging*, vol. 15, no. 4, 2004. 20

[15] M. Griswold, P. M. Jakob, M. Nittka, J. W. Goldfarb, and A. Haase, "Partially parallel imaging with localized sensitivities (PILS)," *Magnetic Resonance in Medicine*, vol. 44, pp. 602–609, 2000. 20, 21

[16] K. P. Pruessman, M. Weiger, M. B. Scheidegger, and P. Boesiger, "SENSE: Sensitivity encoding for fast MRI," *Magnetic Resonance in Medicine*, vol. 42, pp. 952–962, 1999. 20

[17] D. K. Sodickson and W. J. Manning, "Simultaneous acquisition of spatial harmonics (SMASH): Fast imaging with radiofrequency coil arrays," *Magnetic Resonance in Medicine*, vol. 38, pp. 591–603, 1997. 20

[18] M. A. Griswold, P. M. Jakob, R. M. Heidemann, M. Nittka, V. Jellus, J. Wang, B. Kiefer, and A. Haase, "Generalized autocalibrating partially parallel acquisitions (GRAPPA)," *Magnetic Resonance in Medicine*, vol. 47, pp. 1202–1210, 2002. 20

[19] J. Meade, "Frequency filtering on a noisy signal." Advanced Laboratories for Interferometry and Spectroscopic Sciences (ALISS), University of Waterloo, Canada, January 2009. 26

[20] L. Ying and E. Abdelsalam, "Parallel MRI reconstruction: A filter-bank approach," in *Proceedings of IEEE Engineering in Medicine and Biology*, September 2005. 26

[21] S. Mirabbasi and K. Martin, "Classical and modern receiver architectures," *IEEE Communications Magazine*, pp. 132–139, Novemeber 2000. 35, 36, 37

[22] X. Jia, X. Wang, Q. Li, and J. Li, "Improved radio frequency receiver front-end for magnetic resonance imaging," in *Proceedings of IEEE Engineering in Medicine and Biology 27th Annual Conference*, pp. 1328–1331, September 2005. 35

[23] A. A. Abidi, "Direct-conversion radio transceivers for digital communications," in *Proceedings of IEEE Solid-State Circuits Conference*, 1995. Technical Paper 11.1. 35

[24] J. A. Nossek, "Method for digital quadrature amplitude modulation," Oct 1986. US Patent No. 4617537. 42

[25] L. Yu, "A novel adaptive mismatch cancellation system for quadrature if radio receivers," Master's thesis, Carleton University, 1997. 42

[26] D. Morgan, *Surface Acoustic Wave Filters*. Elsevier Ltd., second ed., 2007. 52

[27] R. G. Kinsman, *Crystal Filters*. John Wiley & Sons Inc., 1987. 52

[28] K. Lacanette, "A basic introduction to filter – active, passive, and switched-capacitor," tech. rep., National Semiconductor, April 1991. Application Note 779. 53, 54

[29] B. Razavi, "Design considerations for direct-conversion receivers," *IEEE Transactions on Circuits and Systems – II: Analog and Digital Signal Processing*, vol. 44, pp. 428–435, June 1997. 53

[30] L. D. Paarman, *Design and Analysis of Analog Filters: A Signal Processing Perspective*. USA: Kluwer Academic Publishers, 2001. 54, 55, 56

[31] S. J. Orfanidis, "Lecture notes on elliptic filter design." www.ece.rutgers.edu/∼orfanidi/ece521/notes.pdf, Novemeber 2006. Department of Electrical and Computer Engineering, Rutgers University. 56

[32] A. B. Williams and F. J. Taylor, *Electronic Filter Design Handbook*. USA: McGraw-Hill, 1988. 56, 78, 80

[33] V. S. Zotev, A. N. Matlashov, P. L. Volegov, I. M. Savukov, M. A. Espy, J. C. Mosher, J. J. Gomez, and R. H. K. Jr., "Microtesla MRI of the human brain combined with MEG," *Journal of Magnetic Resonance*, vol. 194, pp. 115–120, 2008. 76